

Innovations in Imaging System Design: Gigapixel, Chip-Scale and Multi- Functional Microscopy

Thesis by

Guoan Zheng

In Partial Fulfillment of the Requirements for the
degree of

Doctor of Philosophy



CALIFORNIA INSTITUTE OF TECHNOLOGY

Pasadena, California

2013

(Defended Oct 19th, 2012)

© 2013

Guoan Zheng

All Rights Reserved

Thesis Committee

Professor Changhuei Yang (Chair)

Professor Hyuck Choo

Professor Yu-Chong Tai

Professor Michael B. Elowitz

Professor Scott E. Fraser

This thesis is dedicated to my parents and my dearest wife, for their constant support and always being my source of inspiration.

Acknowledgements

First of all, I would like to express my sincere gratitude to my advisor, Prof. Changhuei Yang, for giving me the opportunity to work in his lab. I really enjoy the discussion with him for all kinds of innovative ideas, and he always gives me the complete freedom to learn and access any resources that help my research projects. In addition, his passion and enthusiasm for scientific research set up a best role model for me in pursuing my career in the future. I am very thankful that Yang has taught me how to become a creative researcher in all aspects. Without his support, it would be impossible for me to successfully finish my exciting research projects and become an independent researcher.

I am also grateful to Professor Michael B. Elowitz and Dr. Yaron Antebi. They gave me much generous help on culturing stem cells using the ePetri dish platform. I would like to thank Professor Yu-Chong Tai, Professor Scott E. Fraser, Professor P. P. Vaidyanathan, Professor Hyuck Choo, Professor Ali Hajimiri, and Professor Michael B. Elowitz for being my thesis committee and/or my candidacy committee, and providing me their valuable suggestions. They are all my role models for my scientific research career. I would also like to thank Professor Rongguang Liang, Professor Charles DiMarzio, and Professor Zhi-Pei Liang. They are always there to provide me precious advice and generous help both for my research and my career choice.

The Biophotonics lab at Caltech is a great place to work in, and I enjoy every day working with a group of brilliant people there. My thanks go to former group members Dr. Zahid Yaqoob, Dr. Xin Heng, Dr. Jigang Wu, Dr. Emily McDowell, Dr. Xiquan Cui, and Dr. Lap Man Lee. I also want to thank Seung Ah Lee, Samuel Yang, and Xiaoze Ou for being my teammates on some of the research projects over the past years. I still remember that Seung Ah, Samuel, and I went to Texas for the 'Idea to Product' competition. We practiced day and night, and finally won first prize of the competition. I would also like to thank other group members: Dr. Vahan Senekerimyan, Dr. Meng Cui, Dr. Michael Salvador, Dr. Ivo Vellekoop, Dr. Prasanna Pavani, Dr. Benjamin Judkewitz, Jian Ren, Shuo Pang, Ying Min Wang, Chao Han, Roarke Horstmeyer, Mooseok Jang, Christopher Kolner, Zheng Li, and Haojiang Zhou for their friendship and numerous technical

discussions during these years. Anne Sullivan, Christine Garske, and Agnes Tong are our best secretaries. They have made my life a lot easier.

Lastly, I want to express my deepest love and gratitude to my family. I would like to thank my parents and my dearest wife for being with me, for their unconditional support, and for everything they have done for me.

Abstract

Microscopy imaging is of fundamental importance in diverse disciplines of science and technology. In a typical microscopy imaging platform, the light path can be generalized to the following steps: photons leave the light source, interact with the sample, and finally are detected by the image sensor. Based on such a light path, this thesis presents several new microscopy imaging techniques from three aspects: illumination design, sample manipulation, and imager modification.

The first design strategy involves the active control of the illumination sources. Based on this strategy, we demonstrate a simple and cost-effective imaging method, termed Non-interferometric Aperture-synthesizing Microscopy (NAM), for breaking the spatial-bandwidth product barrier of a conventional microscope. We show that the NAM method is capable of providing two orders of magnitude higher throughput for most existing bright-field microscopes without involving any mechanical scanning. Based on NAM, we report the implementation of a 1.6 gigapixel microscope with a maximum numerical aperture of 0.5, a field-of-view of 120 mm^2 , and a resolution-invariant imaging depth of 0.3 mm. This platform is fast (acquisition time of ~ 3 minutes), free from chromatic aberration, capable for phase imaging, and, most importantly, compatible with most existing microscopes. High quality color images of histology slides were acquired by using such a platform for demonstration. The proposed NAM method provides a robust way to transform the problem of high-throughput microscopy from one that is tied to physical limitations of the optics to one that is computationally solvable. The active control of illumination sources can also be adapted for chip-scale microscopy imaging. To this end, we present a lensless microscopy solution termed ePetri-dish. This ePetri-dish platform can automatically perform high resolution (~ 0.66 micron) microscopy imaging over a large field-of-view ($6 \text{ mm} \times 4 \text{ mm}$). This new approach is fully capable of working with cell cultures or any samples in which cells/bacteria may be contiguously connected, and thus, it can significantly improve Petri-dish-based cell/bacteria culture experiments. With this approach providing a low-cost and disposable microscopy solution, we can start to transit Petri-dish-based experiments from the traditionally labor-intensive process to an automated and streamlined process.

The second strategy in design considerations is to manipulate the sample. We present a fully on-chip, lensless, sub-pixel resolving optofluidic microscope (SROFM). This device utilizes microfluidic flow to deliver specimens directly across an image sensor to generate a sequence of low-resolution projection images, where resolution is limited by the sensor's pixel size. This image sequence is then processed to reconstruct a single high-resolution image, where features beyond the Nyquist rate of the LR images are resolved. We demonstrate the device's capabilities by imaging microspheres, *protist Euglena gracilis*, and *Entamoeba invadens* cysts with sub-cellular resolution.

The third accessing point in design considerations is the image sensor. Imager modification is an emerging technique that performs pre-detection light field manipulation. We present two novel optical structure designs: surface-wave-enabled darkfield aperture (SWEDA) and light field sensor. These structures can be directly incorporated onto optical sensors to accomplish pre-detection background suppression and wavefront sensing. We further demonstrate SWEDA's ability to boost the detection sensitivity, with a contrast enhancement of 27 dB.

Table of Contents

Chapter 1: Overview of optical microscopy	1
1.1 Limitations of the conventional microscope	1
1.2 Modern microscopy techniques	4
1.2.1 Super resolution microscopy	4
1.2.2 Digital in-line holography	5
1.3 Structure of this thesis	5
Bibliography	9
Chapter 2: Computational gigapixel microscopy without mechanical scanning	11
2.1 Background.....	11
2.2 Principle and simulations	13
2.2.1 Principle of NAM	13
2.2.2 Simulations of NAM	16
2.2.3 Sampling requirement of NAM	19
2.2.4 Computational cost of NAM	20
2.3 Experimental characterizations of NAM	20
2.3.1 Resolution improvement by NAM	21
2.3.2 Extending imaging depth by digital refocusing	23
2.3.3 Auto-focusing index	26
2.4 Demonstration of imaging capabilities of NAM	27
2.4.1 High-resolution intensity and phase imaging via NAM	27
2.4.2 Parallel computing and image blending for large data sets	29
2.4.3 Gigapixel color imaging via NAM	31
2.5 Discussion	34
Bibliography	36
Chapter 3: ePetri dish, an on-chip cell imaging platform	37
3.1 Background.....	37
3.2 Principle of sub-pixel perspective sweeping microscopy	39
3.3 Wide field-of-view cell imaging using ePetri	43

3.3.1 Color imaging of the stained confluent cell sample	43
3.2.2 Longitudinal cell imaging and tracking	46
3.4 Resolution of the ePetri platform	51
3.5 Discussion	53
Bibliography	56
Chapter 4: Digital 3D refocusing using a LED matrix	59
4.1 Background.....	59
4.2 Principle and experimental setup	60
4.3 Demonstration in biological imaging	62
4.4 Discussion.....	65
Bibliography	66
Chapter 5: Sub-pixel resolving optofluidic microscope	67
5.1 Background.....	67
5.2 The SROFM device	60
5.2.1 Principle of SROFM	69
5.2.2 Fabrication of SROFM device	71
5.3 On-chip imaging using the SROFM device	71
5.3.1 Imaging of non-rotating sample	71
5.3.2 Imaging of rotating sample.....	73
5.3.3 Reconstruction of high resolution video.....	75
5.3.4 Resolution of SROFM	76
5.4 Discussion.....	77
Bibliography	78
Chapter 6: Surface-wave-enabled darkfield aperture	81
6.1 Background.....	81
6.2 SWEDA concept	83
6.3 SWEDA device	85
6.3.1 SWEDA with circular groove pattern	85
6.3.2 SWEDA with linear groove pattern	91
6.4 Boosting detection sensitivity by SWEDA	96

	xi
6.5 Biotin-streptavidin biosensing with SWEDA	98
6.6 Discussion.....	100
Bibliography	102
Chapter 7: Angle-sensitive pixel design for wavefront sensing	105
7.1 Background.....	105
7.2 Angle-sensitive pixel design	106
7.2.1 Principle	106
7.2.2 Simulations of the angle-sensitive pixel design	107
7.3 Discussion.....	112
Bibliography	114
Chapter 8: 0.5 Gigapixel microscopy using a flatbed scanner	115
8.1 Background.....	115
8.2 The prototype setup	117
8.3 Automatic focusing scheme	119
8.4 Resolution and field curve of the platform	121
8.5 Imaging of blood smear and a pathology slide.....	124
8.6 Conclusion	125
Bibliography	127
Chapter 9: Summary	129

List of illustrations

Figure 1-1: Limitations of an infinite-corrected digital microscope system.....	2
Figure 1-2: The design conflict of the conventional microscope system	3
Figure 1-3: The typical setup of digital in-line holographic microscope.....	6
Figure 1-4: The structure of this thesis.....	8
Figure 2-1: Principle and simulation of the proposed NAM approach.....	14
Figure 2-2: The relationship between low-resolution measurements and the high- resolution reconstruction	17
Figure 2-3: Extending imaging depth by digital refocusing.....	18
Figure 2-4: Experimental setup of the gigapixel microscope.....	22
Figure 2-5: NAM reconstructions with different numbers of LED light sources and their corresponding spectrums in the Fourier space	23
Figure 2-6: Extending imaging depth by digital refocusing.....	24
Figure 2-7: Characterization of the imaging-depth of the NAM platform	25
Figure 2-8: Comparison between cases with and without digital refocusing	25
Figure 2-9: Auto-focusing index for locating the axial position of the sample automatically.....	26
Figure 2-10: High-resolution intensity and phase imaging via NAM (blood smear).....	28
Figure 2-11: High-resolution intensity and phase imaging via NAM (pathology slide).....	29
Figure 2-12: Demonstration of image blending.....	30
Figure 2-13: Gigapixel color imaging via NAM	31
Figure 2-14: Comparison between the raw data and the recovered color image with NAM.	32
Figure 2-15: Comparison of image quality between NAM and different objective lenses.	33
Figure 3-1: Principle of SPSM and the ePetri prototype	40
Figure 3-2: Scanning pattern	42

Figure 3-3: Color imaging with ePetri.	44
Figure 3-4: The comparison between the conventional microscopy image (in reflection mode) and the image acquired by the ePetri platform.	45
Figure 3-5: ePetri for cell culturing.....	47
Figure 3-6: Time-lapse imaging of first-stage embryonic stem cell culture on the ePetri platform	49
Figure 3-7: Time-lapse imaging of embryonic stem cell culture on the ePetri platform	50
Figure 3-8: Tracking of cell division (denoted by the arrows) for cell type 1 (a), type 2 (b), and type 3 (c).....	51
Figure 3-9: Resolution of the proposed platform.....	53
Figure 4-1: The proposed illumination scheme	61
Figure 4-2: Demonstration of bright-field and dark-field imaging	63
Figure 4-3: Demonstration of digital 3D refocusing	64
Figure 4-4: Comparison between the proposed method and Kohler illumination.....	65
Figure 5-1: Schematic of the SROFM device.....	70
Figure 5-2: Images obtained from the SROFM device	73
Figure 5-3: Sequential HR images of rotating cells (scale bar 10 μm).....	74
Figure 5-4: Reconstruction of HR video using the multiframe pixel super-resolution algorithm (scale bar 10 μm)	76
Figure 5-5: Resolution of the SROFM prototype obtained with 0.5 μm microspheres.	77
Figure 6-1: Simulations of the circular-groove-based SWEDA	86
Figure 6-2: Experimental characterization of the circular-groove-based SWEDA.....	89
Figure 6-3: Working principle and simulation of the linear-groove-based SWEDA	92
Figure 6-4: Experimental characterization of the linear-groove-based SWEDA.....	94
Figure 6-5: Transmission characterization of the linear-groove-based SWEDA.....	95
Figure 6-6: The sensitivity enhancement demonstration for the circular-groove-based SWEDA.....	97
Figure 6-7: Biotin-streptavidin biosensing with SWEDA.....	99

Figure 7-1: The proposed ASP design	107
Figure 7-2: The FDTD simulation of the front-side illuminated ASP design	109
Figure 7-3: Characterization of the propose ASP design	110
Figure 7-4: The FDTD simulation of the back-side illuminated ASP design	112
Figure 8-1: The setup of the proposed 0.54 gigapixel microscopy (not to scale).....	118
Figure 8-2: The automatic focusing scheme of the proposed setup.....	120
Figure 8-3: USAF resolution target acquired by the proposed 0.54 gigapixel microscopy system.....	122
Figure 8-4: Displacement of the best focal plane of different FOVs (from center to edge FOV).....	123
Figure 8-5: 0.54 monochromatic gigapixel image of a blood smear.	124
Figure 8-6: 0.54 gigapixel color image of a pathology slide (human metastatic carcinoma to liver).....	125
Figure 8-7: The SBP-resolution summary for microscope objectives and the proposed system.....	126

List of frequently used acronyms

Non-interferometric aperture-synthesizing microscopy (NAM)

Sub-pixel perspective sweeping microscopy (SPSM)

Sub-pixel resolving optofluidic microscopy (SROFM)

Surface-wave-enabled darkfield aperture (SWEDA)

Angle-sensitive pixel (ASP)

Numerical aperture (NA)

Complementary metal oxide semiconductor (CMOS)

Full width at half maximum (FWHM)

Point spread function (PSF)

Signal-to-noise ratio (SNR)

Chapter 1

Overview of optical microscopy

Optical microscopy imaging is of fundamental importance in diverse disciplines of science and technology; to name a few key areas, optical microscope is a vital instrument in microelectronics, medical diagnosis, pharmaceutical research and microbiology. Since its debut in the early 17th century, the architecture of the optical microscope has not deviated much from the use of bulky and expensive optical components. Most modern optical microscopes consist of a condenser for light illumination, an objective lens for light collection, and an eyepiece/tube lens for eye observation or digital recording.

In this chapter, we will first discuss the imaging model of the conventional microscopy. Based on that, we will point out the limitations set by the objective lens, the image sensor and the design conflict for different parameters. Next, we will review two groups of the modern microscopy techniques and discuss how they bypass these limitations. Finally, we will introduce our efforts and outline the structure of this thesis.

1.1 Limitations of the conventional microscope

Conventional microscopes are instruments designed to produce magnified visual image of small specimens. The core components of an infinite-corrected digital microscope system are shown in Fig. 1-1: the objective, the tube lens and the image sensor. The objective plays a central role in determining the quality of images that the microscope is capable of producing. It is characterized by two main parameters: resolution (numerical aperture, NA) and field-of-view (also known as field number). On the other hand, the tube lens is used to focus the virtual image to the image sensor. Combined with the objective, it determines the magnification of the microscope system.

From the signal transfer function point-of-view, there are two limitations associated with such a microscope system, as shown in Fig. 1-1. The first limitation comes from the

objective lens. The objective acts like a low-pass filter, with a cutoff frequency determined by the NA. Only the spatial frequency component within the passband can be collected by the objective. Such a low-pass filtering process imposes a resolution limit on the system. Based on Rayleigh criterion, this resolution limit is expressed as

$$R = \frac{0.61\lambda}{NA} \quad (1.1)$$

, where λ is the wavelength of the incidence. The second limitation comes from the image sensor. Adequate resolution of a specimen imaged with the microscope can only be achieved if at least two samples are made for the smallest feature (i.e., R in Eq. (1.1)). In other words, if the pixel size of image sensor is too big, it will induce the aliasing problem for the final image, as shown in Fig. 1-1 (bottom left). A smaller pixel size of the image sensor helps to address the aliasing issue; however, it may also impose limitations on the dynamic range and the signal-to-noise ratio of the device.

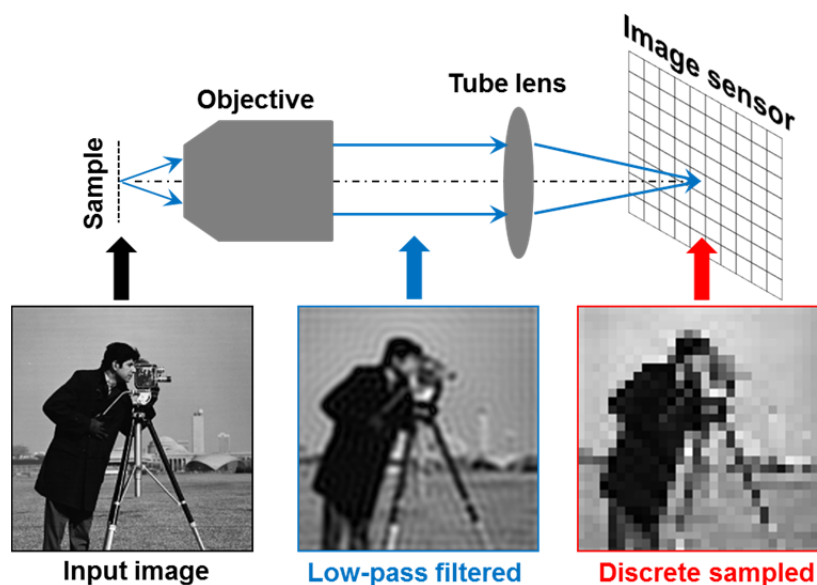


Figure 1-1 (color): Limitations of an infinite-corrected digital microscope system. Top: the sample is magnified by the objective / tube lens system, and sampled by image sensor. Bottom: Two limitations imposed by the objective lens and the image sensor. In this simulation, the following parameters are used: $NA = 0.15$, $\lambda = 0.53 \mu\text{m}$, pixel size = $5.8 \mu\text{m}$, magnification factor = 2.

From the optical design point of view, there are other limitations associated with the conventional microscope system: limited field-of-view, short depth-of-focus, geometric and chromatic aberrations. In conventional microscopy, a better resolution (larger NA) usually implies a smaller field-of-view, a shorter depth-of-focus, and makes it harder for aberration correction. As a reference point, the field-of-view of a typical 0.5 NA 20X objective lens is about 1.1 mm and the depth-of-focus is about 3 microns. The tradeoff between the resolution and other parameters imposes a big limitation for high throughput imaging. For example, in digital pathology industry, the typical imaging area is about 1.5 cm by 1.5 cm, with a desired resolution of 0.5 μm . Therefore, in order to capture the image of the entire field-of-view, we need to perform 3D (x-y-z) mechanical scanning of the sample and stitching the captured images at the end. The x-y scan is for expanding the field-of-view, and the z scan is for bringing the sample into focus for different region of the field-of-view. The design conflict of the conventional microscope system is summarized at Fig. 1-2.

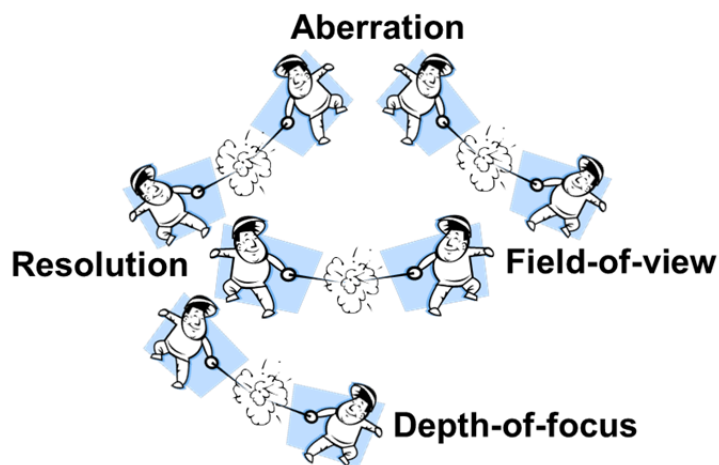


Figure 1-2 (color): The design conflict of the conventional microscope system. A better resolution (larger NA) implies a smaller field-of-view, a shorter depth-of-focus, and makes aberration correction harder.

Regarding the design conflict of the microscope system, can we design better objective lens to expand the field-of-view without compromising on resolution? The

answer is ‘Yes, but very challenging’. The common strategy to expand the field-of-view of an imaging system is to scale the size of the lens up [1]. However, simple size-scaling also introduces geometric aberrations to the system. To compensate for these aberrations, more optical surfaces need to be introduced to increase the degrees of freedom in lens optimization. With the constraint of the tube length and parfocal length of the conventional microscope, expanding field-of-view without compromising resolution is considered very challenging in objective lens design. On the other hand, even though we can design such a ‘super’ objective lens, we still face the limitation on the digital recording. Currently, the total pixel count of a state-of-art image sensor is only about 20 million. In other words, without mechanical scanning, the best image we can capture only contains 20 megapixels, regardless the space-bandwidth product (i.e., the total number of resolvable points) provided by the microscope system.

1.2 Modern microscopy techniques

In the previous section, we discussed the limitations as well as the intrinsic design conflict of the conventional microscope. Fortunately, different types of new microscopy techniques have been developed over the past years, aiming to address some of these issues. In this sub-section, we discuss two types of these developments: super resolution microscopy and digital in-line holography. Super resolution microscopy breaks the diffraction limit imposed by the objective lens. Digital in-line holography technique, on the other hand, addresses the design conflict between different parameters.

1.2.1 Super resolution microscopy

Super-resolution techniques address the low-pass filtering process of the objective lens and allow the capture of images with a higher resolution than the diffraction limit. There are two major groups of methods for the super-resolution microscopy: deterministic and stochastic methods.

Stimulated Emission Depletion Microscopy (STED) and Spatially Structured Illumination microscopy (SSIM) are two good examples of deterministic super resolution microscopy. STED is a process that provides super resolution by selectively deactivating

fluorophores to enhance the imaging resolution in that area [2]. It uses two laser pulses, one for raising the fluorophores to their fluorescent state and the other for the de-excitation of fluorophores by means of stimulated emission [3]. Due to the non-linear dependence of the stimulated emission rate on the intensity of the STED beam, all the fluorophores around the focal excitation spot will be in their off state (the ground state of the fluorophores). By scanning this focal spot across the sample, one retrieves the 2D image. The size of the excitation focal spot can theoretically be infinitely small by raising the intensity of the STED pulse. The other example of deterministic super resolution microscopy, SSIM, is based on the nonlinear dependence of the emission rate of fluorophores on the intensity of the excitation laser [4]. By applying a sinusoidal illumination pattern with a peak intensity close to that needed to saturate the fluorophores, one retrieves nonlinear moiré fringes. The fringes contain high order spatial information that can be extracted by computational techniques. Once the information is extracted, a super-resolution image beyond the diffraction limit is recovered.

Another type of super resolution microscopy is based on the stochastic method. Photoactivated localization microscopy (PALM) [5] or stochastic optical reconstruction microscopy (STORM) [6] is a good example of it. This technique utilizes sequential activation and localization of photoswitchable fluorophores to create a precise location map of fluorophores. During imaging, only a small subset of fluorophores is activated at any given time, as such, the position of each fluorophore can be determined with high precision by locating the centroid of the single-molecule. To date, the spatial resolution achieved by this technique is ~ 20 nm in the lateral dimensions and ~ 50 nm in the axial dimension and the temporal resolution is as fast as ~ 0.5 -1s [7].

1.2.2 Digital in-line holography

Dennis Gabor invented holography in 1948 as a lensless imaging technique to recover both phase and amplitude information simultaneously [8]. Combined with the recent development of digital image sensors, such a technique has been demonstrated as a promising microscopy solution to address some of the design conflicts in the conventional system [9-17]. The basic idea of this technique is to record the interference pattern between

the reference light wave and the wave scattered by small objects. Such an interference pattern is called hologram, after the Greek word ‘holos’, meaning whole. The hologram contains information, by the way of interference fringes, corresponding to both the amplitude and phase of the scattering wave from objects.

In Gabor’s setup, the sample is directly placed between the light source and the intensity recording plane (Fig. 1-3); as such, the axes of both the scattering wave of objects and the reference wave were in parallel (termed in-line holography). The reconstruction of this hologram results in the real image of objects superimposed with an out-of-focus image (termed “twin image”) laying on the same optical axis. There are different approaches to solve this “twin image” problem: 1) introduce an off-axis reference wave [18, 19]; 2) introduce a phase shift of the reference wave [20] ; 3) numerically remove the twin image from post-processing [21-23]. In the context of chip-scale microscopy, the third option is preferable due to the simplicity of the in-line setup, the fast development of digital image acquisition/processing technology and the inherent higher space-bandwidth product of the in-line setup.

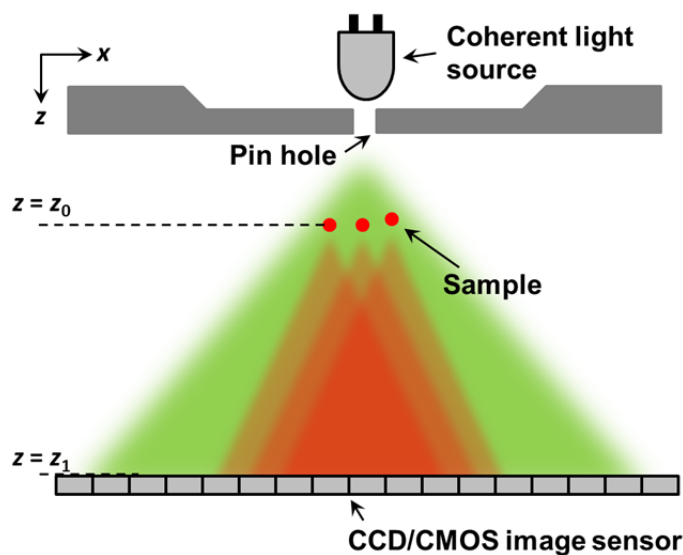


Figure 1-3 (color): The typical setup of digital in-line holographic microscope. The reconstruction process involves the light field propagation back and forth between the imaging domain (where the intensity data is applied) and the object domain (where the object support is applied).

The simplicity and the cost effectiveness of the digital in-line holography platform hold great potentials for different applications [9, 10, 12, 13, 24, 25]. However, there are also several limitations worth noting. First, such an approach relies on the imposed object support in the iterative phase retrieval process; in other words, it only works well for isolated targets with true boundary [26-28]. For a contiguously connected sample like cell cultures, it is difficult to generate an object support mask by intensity thresholding. Second, the iterative phase recovery process may post a heavy load on computational resources. The time to reach a converged solution strongly depends on the scattering property of the sample. It is also possible that no solution can be reached due to the stagnation problem [29]. Third, the interference nature of this approach implies that coherence-based noises, such as cross-interference and speckles, would be presented and would need to be addressed [10, 30, 31]. While methods for mitigating these have been reported [27, 32-34], reconstructed images are still identifiably different, due to artifacts associated with coherence-based noises, from images acquired by the conventional bright-field microscope.

1.3 Structure of this thesis

In a typical microscopy imaging platform, the light path can be generalized to the following steps: photons leave the light source, interact with the sample and finally are detected by the image sensor. Based on such a light path, this thesis presents several new microscopy imaging techniques from three aspects: illumination design, sample manipulation and imager modification.

The first design strategy involves the active control of the illumination sources. Based on this strategy, we will present the first successful implementation of a gigapixel bright-field microscope without mechanical scanning (**Chapter 2**). The active control of illumination sources can also be adapted for chip-scale microscopy imaging. To this end, we will present a lensless microscopy solution termed ePetri-dish (**Chapter 3**). Based on the combination between the active illumination control and tomography reconstruction,

we will further demonstrate the implementation of 3D imaging without involving mechanical scanning (**Chapter 4**).

The second strategy in design considerations is to manipulate the sample. To this end, we will present a fully on-chip, lensless, sub-pixel resolving optofluidic microscope (SROFM). We will demonstrate the device's capabilities by imaging microspheres, *protist Euglena gracilis*, and *Entamoeba invadens* cysts with sub-cellular resolution (**Chapter 5**).

Illumination design	Sample manipulation	Sensor modification
Ch2 Fast gigapixel microscopy Ch3 ePetri dish Ch4 3D digital refocusing	Ch5 Sub-pixel resolving optofluidic microscopy (SROFM)	Ch6 Surface-wave-enabled darkfield aperture (SWEDA) Ch7 Design of light field pixel Ch8 0.5 gigapixel microscopy using a scanner

Figure 1-4 (color): The structure of this thesis. Based on the light path of typical imaging system, this thesis presents several new microscopy imaging techniques from three aspects: illumination design, sample manipulation and imager modification.

The third accessing point in design considerations is the image sensor. Imager modification is an emerging technique that performs pre-detection light field manipulation. We will present two novel optical structure designs: surface-wave-enabled darkfield aperture (SWEDA) and light field pixel. These structures can be directly incorporated onto optical sensors to accomplish pre-detection background suppression and wavefront sensing (**Chapter 6** and **Chapter 7**). Lastly, we will show that the image sensor can also be replaced by a flatbed scanner to achieve ultrahigh pixel count for wide field-of-view imaging (**Chapter 8**).

The structure of this thesis is summarized in Fig. 1-4.

Bibliography

- [1] A. W. Lohmann, "Scaling laws for lens systems," *Applied optics*, vol. 28, no. 23, pp. 4996-4998, 1989.
- [2] V. Westphal, S. O. Rizzoli, M. A. Lauterbach *et al.*, "Video-Rate Far-Field Optical Nanoscopy Dissects Synaptic Vesicle Movement," *Science*, vol. 320, no. 5873, pp. 246-249, April 11, 2008.
- [3] S. W. Hell, "Far-Field Optical Nanoscopy," *Science*, vol. 316, no. 5828, pp. 1153-1158, May 25, 2007.
- [4] M. G. L. Gustafsson, "Nonlinear structured-illumination microscopy: wide-field fluorescence imaging with theoretically unlimited resolution," *Proceedings of the National Academy of Sciences of the United States of America*, vol. 102, no. 37, pp. 13081, 2005.
- [5] S. T. Hess, T. P. K. Girirajan, and M. D. Mason, "Ultra-high resolution imaging by fluorescence photoactivation localization microscopy," *Biophysical journal*, vol. 91, no. 11, pp. 4258-4272, 2006.
- [6] M. J. Rust, M. Bates, and X. Zhuang, "Sub-diffraction-limit imaging by stochastic optical reconstruction microscopy (STORM)," *Nature methods*, vol. 3, no. 10, pp. 793-796, 2006.
- [7] B. Huang, W. Wang, M. Bates *et al.*, "Three-dimensional super-resolution imaging by stochastic optical reconstruction microscopy," *Science*, vol. 319, no. 5864, pp. 810-813, 2008.
- [8] D. Gabor, "A new microscopic principle," *Nature*, vol. 161, no. 4098, pp. 777-778, 1948.
- [9] W. Xu, M. Jericho, I. Meinertzhagen *et al.*, "Digital in-line holography for biological applications," *Proceedings of the National Academy of Sciences of the United States of America*, vol. 98, no. 20, pp. 11301, 2001.
- [10] J. Garcia-Sucerquia, W. Xu, S. K. Jericho *et al.*, "Digital in-line holographic microscopy," *Applied optics*, vol. 45, no. 5, pp. 836-850, 2006.
- [11] L. Repetto, E. Piano, and C. Pontiggia, "Lensless digital holographic microscope with light-emitting diode illumination," *Optics letters*, vol. 29, no. 10, pp. 1132-1134, 2004.
- [12] O. Mudanyali, D. Tseng, C. Oh *et al.*, "Compact, light-weight and cost-effective microscope based on lensless incoherent holography for telemedicine applications," *Lab on a Chip*, vol. 10, no. 11, pp. 1417, 2010.
- [13] D. Tseng, O. Mudanyali, C. Oztoprak *et al.*, "Lensfree microscopy on a cellphone," *Lab Chip*, vol. 10, no. 14, pp. 1787-1792, 2010.
- [14] J. Garcia-Sucerquia, W. Xu, M. H. Jericho *et al.*, "Immersion digital in-line holographic microscopy," *Opt. Lett.*, vol. 31, no. 9, pp. 1211-1213, 2006.
- [15] P. Marquet, B. Rappaz, P. J. Magistretti *et al.*, "Digital holographic microscopy: a noninvasive contrast imaging technique allowing quantitative visualization of living cells with subwavelength axial accuracy," *Optics letters*, vol. 30, no. 5, pp. 468-470, 2005.
- [16] B. Rappaz, P. Marquet, E. Cuhe *et al.*, "Measurement of the integral refractive index and dynamic cell morphometry of living cells with digital holographic microscopy," *Optics express*, vol. 13, no. 23, pp. 9361-9373, 2005.

- [17] F. Charrière, A. Marian, F. Montfort *et al.*, “Cell refractive index tomography by digital holographic microscopy,” *Optics letters*, vol. 31, no. 2, pp. 178-180, 2006.
- [18] E. N. Leith, and J. Upatnieks, “Reconstructed wavefronts and communication theory,” *JOSA*, vol. 52, no. 10, pp. 1123-1128, 1962.
- [19] E. N. Leith, and J. Upatnieks, “Wavefront reconstruction with diffused illumination and three-dimensional objects,” *JOSA*, vol. 54, no. 11, pp. 1295-1301, 1964.
- [20] I. Yamaguchi, and T. Zhang, “Phase-shifting digital holography,” *Optics letters*, vol. 22, no. 16, pp. 1268-1270, 1997.
- [21] G. Liu, and P. Scott, “Phase retrieval and twin-image elimination for in-line Fresnel holograms,” *J. Opt. Soc. Am. A*, vol. 4, no. 1, pp. 159, 1987.
- [22] J. R. Fienup, “Reconstruction of an object from the modulus of its Fourier transform,” *Optics letters*, vol. 3, no. 1, pp. 27-29, 1978.
- [23] G. Koren, F. Polack, and D. Joyeux, “Iterative algorithms for twin-image elimination in in-line holography using finite-support constraints,” *JOSA A*, vol. 10, no. 3, pp. 423-433, 1993.
- [24] W. Bishara, T. W. Su, A. F. Coskun *et al.*, “Lensfree on-chip microscopy over a wide field-of-view using pixel super-resolution,” *Optics Express*, vol. 18, no. 11, pp. 11181-11191, 2010.
- [25] S. Jericho, P. Klages, J. Nadeau *et al.*, “In-line digital holographic microscopy for terrestrial and exobiological research,” *Planetary and Space Science*, vol. 58, no. 4, pp. 701-705, 2010.
- [26] J. R. Fienup, “Reconstruction of a complex-valued object from the modulus of its Fourier transform using a support constraint,” *J. Opt. Soc. Am. A*, vol. 4, no. 1, pp. 118-123, 1987.
- [27] J. Rodenburg, A. Hurst, and A. Cullis, “Transmission microscopy without lenses for objects of unlimited size,” *Ultramicroscopy*, vol. 107, no. 2-3, pp. 227-231, 2007.
- [28] F. Zhang, G. Pedrini, and W. Osten, “Phase retrieval of arbitrary complex-valued fields through aperture-plane modulation,” *Physical Review A*, vol. 75, no. 4, pp. 043805, 2007.
- [29] J. R. Fienup, and C. C. Wackerman, “Phase-retrieval stagnation problems and solutions,” *J. Opt. Soc. Am. A*, vol. 3, no. 11, pp. 1897-1907, 1986.
- [30] M. Malek, D. Allano, S. Coëtmelec *et al.*, “Digital in-line holography: influence of the shadow density on particle field extraction,” *Optics Express*, vol. 12, no. 10, pp. 2270-2279, 2004.
- [31] L. Xu, J. Miao, and A. Asundi, “Properties of digital holography based on in-line configuration,” *Optical Engineering*, vol. 39, no. 12, pp. 3214-3219, 2000.
- [32] S. Lai, B. King, and M. A. Neifeld, “Wave front reconstruction by means of phase-shifting digital in-line holography,” *Optics Communications*, vol. 173, no. 1-6, pp. 155-160, 2000.
- [33] V. Micó, J. García, Z. Zalevsky *et al.*, “Phase-Shifting Gabor Holographic Microscopy,” *Journal of Display Technology*, vol. 6, no. 10, pp. 484-489, 2010.
- [34] A. Greenbaum, U. Sikora, and A. Ozcan, “Field-portable wide-field microscopy of dense samples using multi-height pixel super-resolution based lensfree imaging,” *Lab Chip*, 2012.

Chapter 2

Computational gigapixel microscopy without mechanical scanning

Spatial-bandwidth product characterizes the total resolvable pixels of an imaging system. A typical microscope platform operates on the order of 10 megapixels. In this chapter, we demonstrate a simple and cost-effective imaging method, termed Non-interferometric Aperture-synthesizing Microscopy (NAM), for breaking the spatial-bandwidth product barrier of a conventional microscope. We show that the NAM method is capable for providing two orders of magnitude higher throughput for most existing bright-field microscopes without involving any mechanical scanning. Based on NAM, we report the implementation of a 1.6 gigapixel microscope with a maximum numerical aperture (NA) of 0.5, a field-of-view (FOV) of 120 mm², and a resolution-invariant imaging depth of 0.3 mm. High quality color images of histology slides were acquired by using such a platform for demonstration. The proposed NAM method, readily implemented with a conventional microscope, has the potential to broadly impact digital pathology, histology, phytotomy, immunochemistry and forensic photography.

2.1 Background

The throughput of an optical imaging system is fundamentally limited by the spatial-bandwidth product (i.e., the total resolvable points) of the optics. For a conventional microscope platform, the spatial-bandwidth product is on the order of 10 megapixels, regardless different magnification factors of objective lenses. As a reference point, the resolution of a 20X objective lens (NA of 0.4) is $\sim 0.8 \mu\text{m}$ and the corresponding FOV is $\sim 1.1 \text{ mm}$ in diameter, resulting in a spatial-bandwidth product of ~ 7 megapixels. Barriers to higher spatial-bandwidth product include 1) scale-dependent geometric aberrations, 2) constraints of the fixed mechanical tube length of the relay optics and the fixed objective

parfocal length, 3) the availability of gigapixel digital recording devices. These three barriers are considered very challenging in the realm of optical and electronic design.

In the past years, there have been attempts to apply the interferometric synthetic aperture technique to increase the spatial-bandwidth product of an objective lens [1-11]. Most of these concerned setups record both the intensity and phase information by using interferometric holography approaches, such as off-line holography and phase-shifting holography. The recorded data are then synthesized in the Fourier domain in a deterministic manner. Although improvements in resolution have been demonstrated, such an interferometric synthetic aperture technique is still rarely applied for practical applications in the microscopy community. Limitations of this technique lie in fourfold: 1) interferometric holography recordings in these setups require the use of highly-coherent light sources (i.e., lasers). As such, the reconstructed images are suffered from coherent noise sources, such as speckles noise, fixed pattern noise (induced by diffraction from dust particles and other optical imperfections in the beam path), and multiple interferences between different optical interfaces. The image quality is, therefore, not comparable to that of a conventional microscope. On the other hand, the use of off-axis holography approach also scarifies useful spatial-bandwidth product (i.e., the total pixel number) of the image sensor [12]. 2) Interferometric imaging used in this technique is subjected to the uncontrollable phase fluctuation between different measurements. A priori knowledge of the sample may be needed for setting a reference point in the image recovery process (also shown as phase referring). 3) All of reported setups require mechanical scanning, either for rotating the sample or for changing the illumination angle. Therefore, precise optical alignments, mechanical control in sub-micron level and associated maintenances are all needed for these platforms. In terms of the spatial-bandwidth product, they present no advantage compared to a platform using a conventional microscope with sample scanning and image stitching. 4) The reported platforms are not compatible to a conventional microscope. In other words, it is difficult to incorporate such an imaging technique into most existing microscope platforms without substantial modifications. Due to the high complexity of these platforms, to the best of our knowledge, color imaging capability (pivotal for pathology and histology) has also not been demonstrated so far.

A major step forward to extend the potential of synthetic aperture technique is to develop a method that is capable for breaking the spatial-bandwidth product barrier of a conventional microscope and address above discussed issues in a simple and cost-effective manner. In this chapter, we introduce and demonstrate such an imaging method, termed Non-interferometric Aperture-synthesizing Microscopy (NAM). We show that the NAM method is capable for providing two orders of magnitude higher throughput for most existing bright-field microscopes without involving any mechanical scanning. Based on NAM, we report the implementation of a 1.6 gigapixel microscope with a maximum NA of 0.5, a FOV of 120 mm^2 , and a resolution-invariant imaging depth of 0.3 mm. This chapter is structured as follows. We will first describe the principle and simulation results of the NAM method. Next, we will report on our experimental setup of the gigapixel imaging platform. We will then demonstrate the phase and color imaging capabilities of the proposed platform for biological applications. Finally, we will discuss the application advantages as well as limitations of the NAM platform.

2.2 Principle and simulations

2.2.1 Principle of NAM

Principle of the NAM method is illustrated in Fig. 2-1. To understand the principle, we first consider a 2D sample with an intensity profile $I(x, y)$ and a phase profile $\varphi(x, y)$ (Fig. 1a, left-hand side). We use a conventional microscope with a 2X objective lens (0.08 NA) to acquire low-resolution intensity images of this sample. We assume the sample is placed at the axial position $z = z_0$, while the in-focus position of the objective lens locates at position $z = 0$; in other words, the sample is out-of-focus by the amount of z_0 . In the measurement process, we illuminate the sample with different incident angles and capture corresponding low-resolution intensity images, as shown in the middle part of Fig. 2-1(a). The wave vector of the incidence in x and y direction can be denoted as k_{xi} and k_{yi} . Based on these low-resolution intensity measurements, our goal is to recover high-resolution intensity and phase profiles of the sample (Fig. 2-1(a), right-hand side).

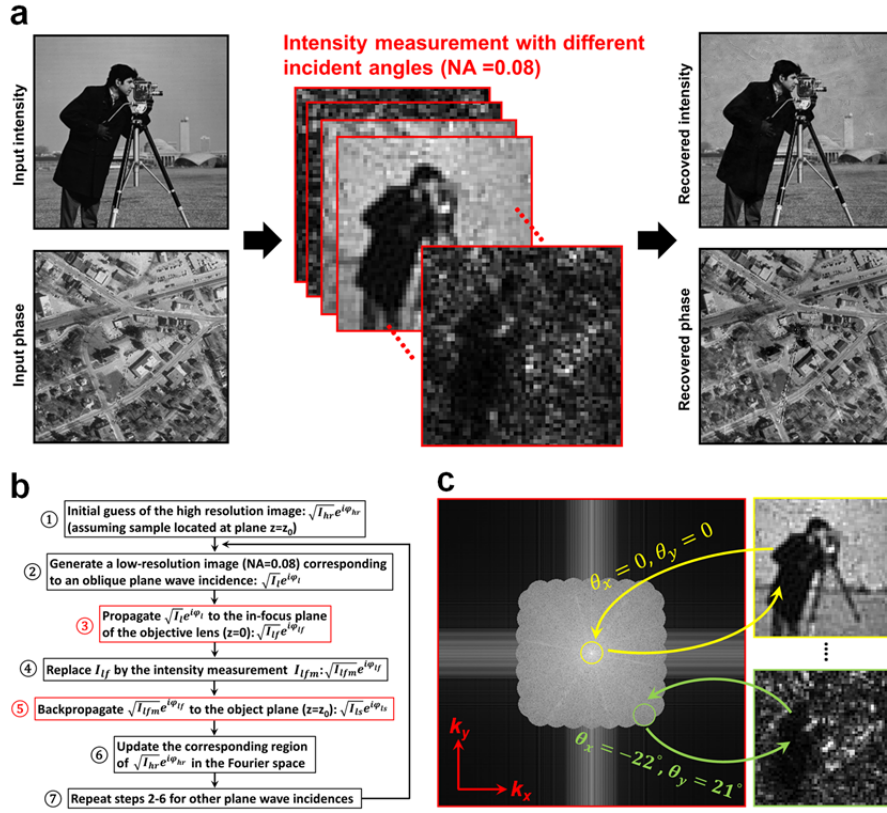


Figure 2-1 (color): Principle and simulation of the proposed NAM approach. (a) We consider a 2D sample with an intensity profile $I(x, y)$ and a phase profile $\varphi(x, y)$. In the measurement process, we illuminate the sample with different incident angles and capture corresponding low-resolution intensity images. Based on these low resolution intensity measurements, we then recover high-resolution intensity and phase profiles of the sample (right-hand side). (b) The recovery procedure of the NAM method. (c) Graphical summary of the recovery procedure: the intensity of the low-pass filtered image is replaced by the actual low-resolution measurement and the corresponding Fourier space of the high-resolution reconstruction is updated accordingly.

The basic idea of the proposed recovery process is to iteratively look for a solution that can satisfy all the intensity measurements. Before diving into the detailed recovery procedure, we would like to first clarify several important concepts: 1) spatial and Fourier domain representations. In the recovery process, we keep switching back and forth between two working domains: one is the spatial domain (i.e. x - y space) and the other is the Fourier

domain (i.e. k_x - k_y space; k_x and k_y are the wave number in x and y directions). The connection between these two domains is through discrete Fourier transform. 2) Oblique incidence. Illuminating the sample by an oblique plane wave with a wave vector (k_{xi}, k_{yi}) is equivalent to shift the spectrum of the sample by the amount of (k_{xi}, k_{yi}) in the Fourier domain. 3) Optical-transfer-function of the objective lens. In the Fourier domain, the objective lens acts as a low-pass filter. The filtering function is a circular pupil with a radius of $NA \cdot k_0$, where k_0 equals $2\pi/\lambda$ (the wave number in vacuum). 4) Free-space propagating. We assume the sample is placed at position $z = z_0$, while the in-focus position of the objective lens locates at $z = 0$. In other words, the image we capture is not the sample profile itself; it is the sample profile propagating by $-z_0$ distance. Such a free-space propagating step can be modeled by a multiplication of a phase factor in the Fourier space. Later this chapter, we will show that free-space propagating in the recovery process allows us to perform digital refocusing without mechanical moving the sample at the z direction, and it is pivotal for extending the imaging depth and correcting the chromatic aberration of the optics.

With these four concepts in mind, we precede to the detailed description of the recovery procedure shown in Fig. 2-1(b): 1) we start with a guess of the high-resolution object function in the spatial domain: $\sqrt{I_{hr}}e^{i\varphi_{hr}}$ ('hr' stands for 'high-resolution'). The guess can be a random complex matrix (for both intensity and phase) or an interpolation of the low-resolution intensity measurement with a random phase. 2) Based on the $\sqrt{I_{hr}}e^{i\varphi_{hr}}$, we then perform low-pass filtering to generate a low-resolution image $\sqrt{I_l}e^{i\varphi_l}$ ('l' stands for 'low-resolution') corresponding to an oblique plane wave incidence. We note that the low-pass filtering process is performed at the Fourier domain of $\sqrt{I_{hr}}e^{i\varphi_{hr}}$. The filter we applied is the optical transfer function of the objective lens discussed in the previous paragraph (concept 3). For an oblique incidence with a wave vector (k_{xi}, k_{yi}) , we simply center such a filter at position $(-k_{xi}, -k_{yi})$ in the Fourier space to perform the filtering. 3) We then propagate the filtered image to the in-focus position of the objective lens and get $\sqrt{I_{lf}}e^{i\varphi_{lf}}$ ('f' here stands for 'focused position'). This step only involves the multiplication of a phase factor in the Fourier space. 4) We then replaced I_{lf} in the low-resolution image

$\sqrt{I_{lf}}e^{i\varphi_{lf}}$ by the actual low-resolution intensity measurement I_{lfm} . As such, the updated low-resolution image corresponding to incident wave vector (k_{xi}, k_{yi}) is $\sqrt{I_{lfm}}e^{i\varphi_{lf}}$. 5) The updated low-resolution image $\sqrt{I_{lfm}}e^{i\varphi_{lf}}$ is then back-propagate to the position of sample plane and we get $\sqrt{I_{ls}}e^{i\varphi_{ls}}$ ('s' here stands for 'sample'). 6) Next, we perform Fourier transform of $I_{ls}e^{i\varphi_{ls}}$ and update the corresponding region of the Fourier space of $\sqrt{I_{hr}}e^{i\varphi_{hr}}$ accordingly. As an example, the region corresponding to the normal incidence locates at the center part of the Fourier space (enclosed by the yellow circle in Fig. 2-1(c)). 7) Repeat steps 2-6 for other incident angles. 8) Repeat step 2-7 until the solution converges. In a typical implementation (including all the simulation and experimental data demonstrated in this chapter), we only repeat step 2-7 for once. Finally, we note that, step 3 and 5 can be ignored if the sample is placed at the in-focus position of the objective lens.

2.2.2 Simulations of NAM

We first investigated the performance of the proposed NAM method by simulations. The simulated sample intensity and phase are shown in the left-hand side of Fig. 2-1(a). The pixel size of these two input profiles is 275 nm and the wavelength of the simulated incidence is 632 nm (also see the discussion on sampling requirement in Section 2.2.3). The sample was illuminated by plane waves with 137 different incident angles, filtered by a 2X objective lens (0.08 NA) and then captured by an image sensor with 5.5 μm pixel size. In this simulation (Fig. 2-1), we assume the sample is placed at the in-focus position of the objective lens (the case for defocusing will be discussed in Fig. 2-3). The resulting low-resolution images, added with 1% random speckle noise, are shown in the middle part of Fig. 2-1(a). Based on these low-resolution images, we then reconstructed the high-resolution image following the recovery procedure discussed above, with a maximum NA of 0.5 in the Fourier space. Intensity and phase profiles of the reconstructed image are shown in the right-hand side of Fig. 2-1(a). We can see that, high-resolution images of the sample can be recovered without involving phase measurement in the data acquisition process. In other words, interferometry-based setup is not needed in the proposed NAM method. We graphically summarized the recovery procedure in Fig. 2-1(c): the intensity of

the low-pass filtered image is replaced by the actual low-resolution measurement and the corresponding Fourier space of the high-resolution reconstruction is updated accordingly.

To further demonstrate the relationship between low-resolution measurements and the high-resolution reconstruction, we show 9 (out of 137) low-resolutions raw images and their corresponding regions in the reconstructed Fourier spectrum in Fig. 2-2.

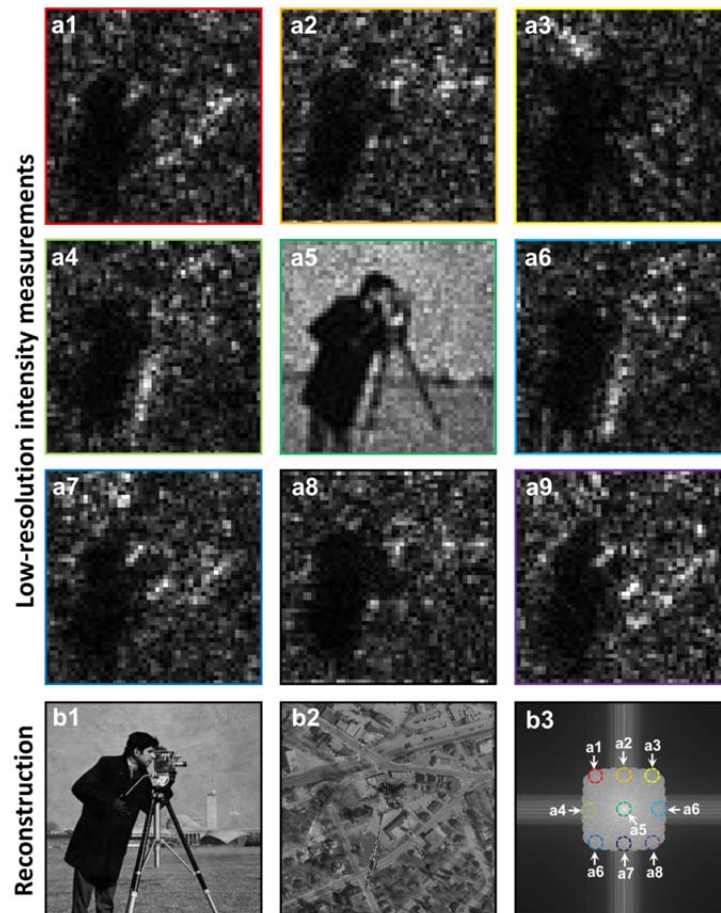


Figure 2-2 (color): The relationship between low-resolution measurements and the high-resolution reconstruction. (a1-a9) Low-resolution measurements (9 out of 137). (b1-b2) The reconstructed intensity and phase images. (b3) The Fourier space of the recovered image. Corresponding regions for low-resolution measurements are highlighted.

In a conventional microscope, the resolution degrades as the sample moves away from the in-focus position; to achieve the optimal resolution, one needs to use the stage to

mechanically bring the sample back into focus. In the proposed NAM method, such a sample focusing step can be done digitally rather than mechanically. To perform digital refocusing in NAM, we only need to include two free-space propagating steps in the recovery procedure (step 3 and 5 in Fig. 2-1(b)). In Fig. 2-3, we perform a set of simulations to verify the capability of NAM for digital refocusing. From this figure, we can see that the high-resolution reconstruction (column 2 and 3) is invariant to the sample defocusing. Reconstructions without digital refocusing are also provided in column 4 and 5 in Fig. 2-3 for comparison.



Figure 2-3 (color): Extending imaging depth by digital refocusing. Each row represents a different defocused amount at z direction. Column 1 is the low-resolution image. Column 2 and 3 are the recovered high-resolution intensity and phase profiles with digital refocusing. Column 4 and 5 are the recovered high-resolution intensity and phase profiles without digital refocusing.

The numerical analysis demonstrated in this sub-section verifies the principle of the proposed NAM method. Since we can reconstruct the high-resolution image with a low NA lens, the FOV can be decoupled from the resolution of the lens and the throughput of the imaging system is not limited by the spatial-bandwidth product of the optics anymore.

2.2.3 Sampling requirement of NAM

There are two questions regarding the sampling requirement of the proposed NAM method: 1) given the NA of an objective lens, what is the largest pixel size we can use for acquiring the low-resolution intensity images; 2) given the synthetic NA of the reconstructed image, what is the largest pixel size we can use for representing the reconstructed intensity image. In this sub-section, we try to answer these two questions. We further defined the pixel size ratio between the raw image and the reconstructed image as the ‘enhancement factor’ of the NAM method (the larger this factor, the higher the system throughput).

Since we can recover both intensity and phase information with NAM, the answer to question 1 is the same as the sampling requirement for coherent optical systems: $\lambda/(2 \cdot NA_{obj})$. For question 2, we note that, the synthetic NA is for the electric field E (with amplitude and phase). The final reconstruction, on the other hand, is for the intensity profile I ($I = E \cdot E^*$, where ‘*’ denotes for complex conjugate). Such a multiplication of electric field in the spatial domain corresponds to a convolution operation in the Fourier domain. As such, the passband of the reconstructed intensity image double in the Fourier domain. Therefore, the largest pixel size we can use for representing the reconstructed intensity image is $\lambda/(4 \cdot NA_{syn})$ at the sample plane. If we choose the largest pixel sizes both for the raw image and the reconstructed image, the enhancement factor of NAM can then be expressed as:

$$Enhancement\ factor = 2 \cdot NA_{syn} / NA_{obj} \quad (2-1)$$

For implementing the NAM method in this chapter, we use a 2X objective with 0.08 NA and an image sensor with 5.5 μm pixel size. From the answer to question 1, we can see that the largest pixel size we can use at the image plane is $2 \cdot \lambda / (2 \cdot NA_{obj}) = 5.88 \mu\text{m}$ for blue light. The 5.5 μm pixel size of our image sensor is, therefore, in accord with such a requirement. On the other hand, based on the answer to question 2, pixel sizes (at the

sample plane) of the reconstructed image are $0.33 \mu\text{m}$, $0.29 \mu\text{m}$ and $0.27 \mu\text{m}$ for red, green and blue wavelengths. For simplicity, we choose a reconstructed pixel size of $0.275 \mu\text{m}$ for these three wavelengths in our implementation, corresponding to an enhancement factor of 10.

2.2.4 Computational cost of NAM

A major difference between the proposed NAM method and conventional microscopy techniques lies in the image recovery process. Therefore, it is worth to discuss the computational cost of such a process in detail. Assuming the low-resolution image we captured using the image sensor contains n pixels and we use m different LEDs for illuminations, the computational complexity of NAM can be estimated in the following: 1) in step 2 of the recovery process, we perform a fast Fourier transform (FFT) to generate the low-resolution image $\sqrt{I_l}e^{i\varphi_l}$. The corresponding computational cost is $n \cdot \log(n)$. 2) In step 6, we perform another FFT to update the corresponding region of the Fourier space of $\sqrt{I_{hr}}e^{i\varphi_{hr}}$. The corresponding computational cost is $n \cdot \log(n)$. 3) In step 7, the above computation is repeated for all incident angles; therefore, we get $m \cdot 2 \cdot n \cdot \log(n)$. 4) In step 8, the above computation is repeated for once; therefore, we get $2 \cdot m \cdot 2 \cdot n \cdot \log(n)$. Other steps in the recovery process are negligible compared to the above value.

In summary, the computational complexity of the proposed NAM method is $4 \cdot m \cdot n \cdot \log(n)$, given that m is the total number of oblique incidences and n is the total number of pixels of a low-resolution image.

2.3 Experimental characterizations of NAM

To further validate the proposed NAM method in experiment, we used an Olympus BX 41 microscope platform with a 2X objective lens (0.08 NA, Olympus) and a CCD camera (Kodak KAI-29050, $5.5 \mu\text{m}$ pixel size) as our experimental imaging setup. The field number of the 2X objective lens is 26.5; in other words, the aberration-corrected FOV at the sample plane is 13.25 mm in diameter. We placed a programmable LED matrix under the sample stage as the illumination source (Fig. 2-4(a) and 2-4(b)). This LED matrix

contains 32*32 surface-mount full-color LEDs (SMD 3528). The central wavelengths of the full-color LED are 632 nm, 532 nm and 472nm for red, green and blue, with a 5 nm bandwidth (also see the inset of Fig. 2-4(b)). The measured distance (at z direction) between the sample stage and the LED array (i.e., 'H') was 83 mm. The size of this 32*32 LED array is 128 mm; in the words, the distance between adjacent LEDs is 4 mm). An Atmel ATMEGA-328 microcontroller provided the logical control for this LED matrix. To achieve maximum brightness, the matrix was driven statically rather than in normal scanning mode, eliminating the duty cycle and boosting currents through the LEDs at its maximum level. The measured light intensities were 0.9, 1.2 and 0.5 W/m² for color red, green and blue, respectively.

2.3.1 Resolution improvement by NAM

The improvement in resolution provided by NAM was demonstrated by imaging a USAF resolution target in Fig. 2-4(c) and 2-4(d). In this experiment, we used 137 red LEDs as our light sources for oblique illuminations. The corresponding maximum NA of the reconstructed image is ~0.5 in the diagonal direction of the Fourier space. Fig. 2-4(c1) shows the full FOV image of the USAF target. Fig. 2-4(c2) and 2-4(c3) show the zoom-in views of the raw data, with a pixel size of 2.75 μm (5.5 μm divided by the magnification factor). The corresponding high-resolution NAM images are shown in Fig. 2-4(d1) and 2-4(d2) for comparison, where the pixel size is 0.275 μm . From these figures, we can clearly see the resolution improvement by using the NAM method. In Fig. 2-5, we further demonstrate cases with different numbers of LED light sources and their corresponding NAM reconstructions with different synthetic NAs. This experiment further verified that the FOV can be decoupled from the resolution of the optics via NAM; as such, we can get ultra-wide FOV and high-resolution at the same time.

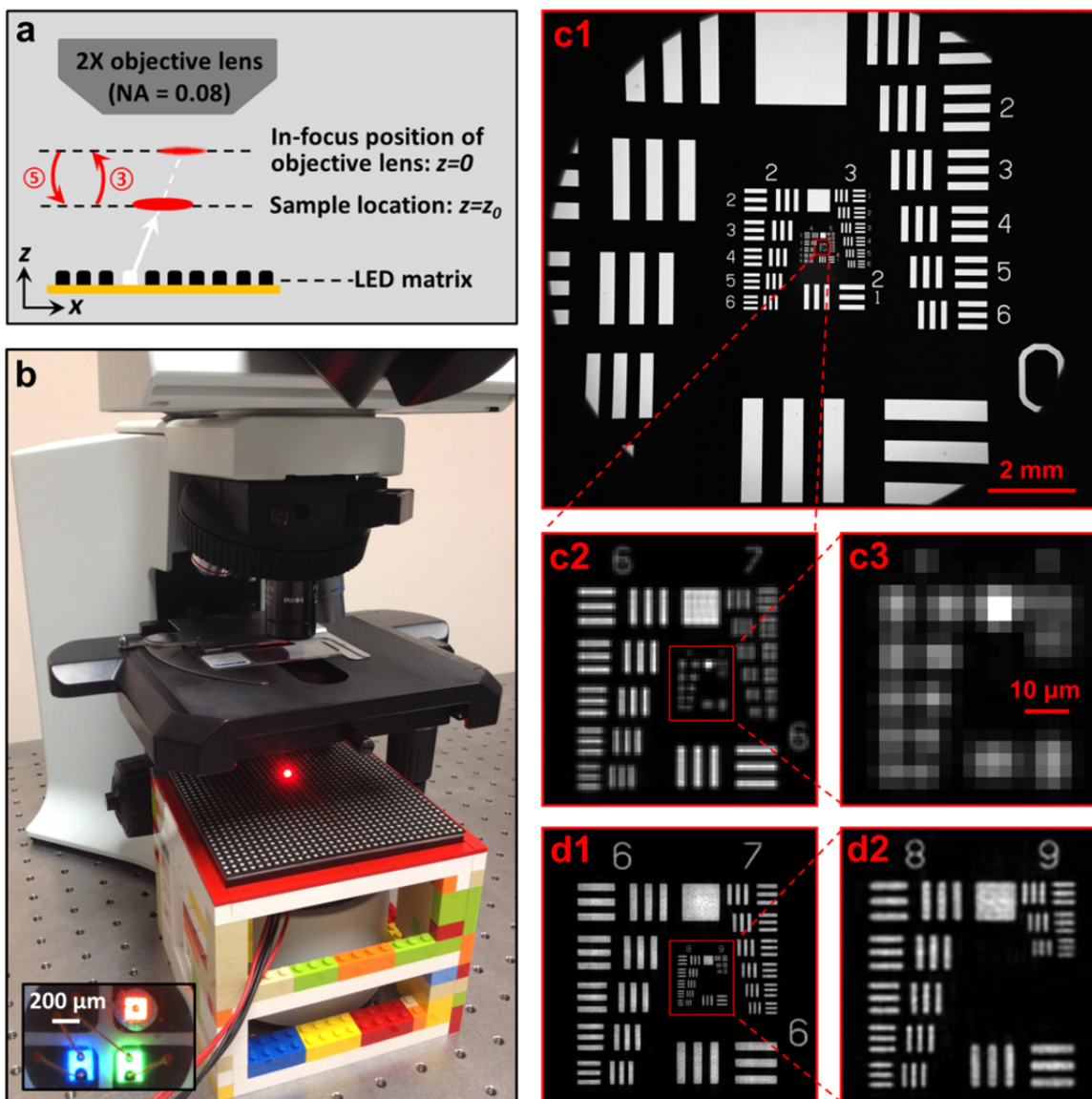


Figure 2-4 (color): Experimental setup of the gigapixel microscope. (a) Scheme of the setup. Step 3 and 5 in the image recovery process are highlighted. These two steps are critical for extending the imaging depth of NAM. (b) A 32*32 programmable LED matrix is placed beneath the sample stage for illuminations. (Inset) Each LED can provide red, green and blue illuminations. (c1) The full FOV image of the USAF resolution target. (c2 and c3) Zoom-in views of the raw data, with a pixel size of $2.75 \mu\text{m}$. (d1 and d2) The corresponding reconstructed NAM images, where the pixel size is $0.275 \mu\text{m}$.

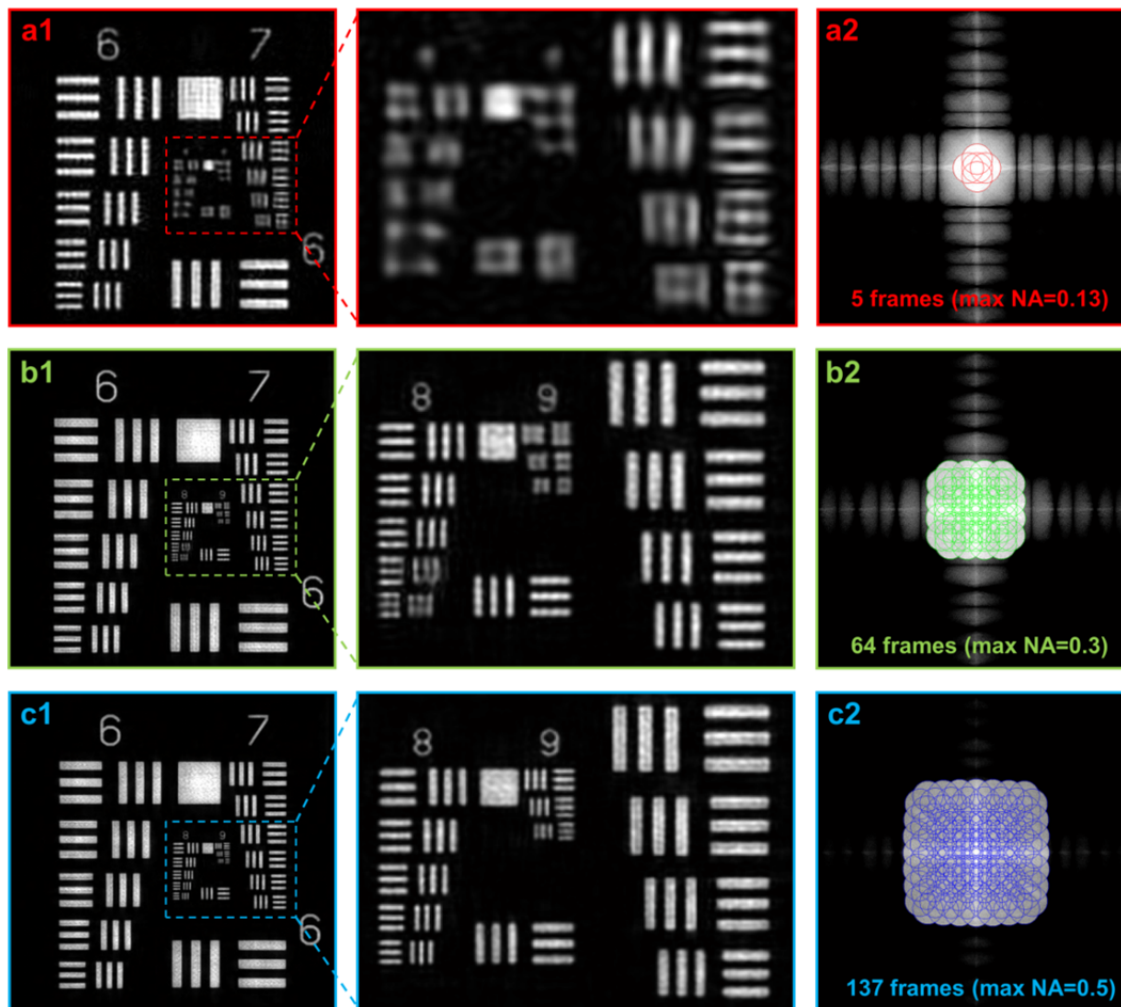


Figure 2-5 (color): NAM reconstructions with different numbers of LED light sources and their corresponding spectrums in the Fourier space. (a) 5 frames reconstruction with a maximum NA of 0.13. (b) 64 frames reconstruction with a maximum NA of 0.3. (c) 137 frames reconstruction with a maximum NA of 0.5. Each small circle in (a2)-(c2) represents the spectrum region corresponding to one low-resolution measurement.

2.3.2 Extending imaging depth by digital refocusing

Another limitation of the conventional microscope platform is the limited depth-of-field. As a reference point, the depth-of-field of a 20X objective lens with 0.4 NA is about 5 μm . In this regard, a precise mechanical stage is needed in the conventional setup to mechanically bring the sample back into the in-focus position of the objective lens. In the

proposed NAM method, such a sample focusing step can be done digitally rather than mechanically. To perform digital refocusing in NAM, we only need to include two light-field propagating steps in the recovery procedure (step 3 and 5 in Fig. 2-1(a)).

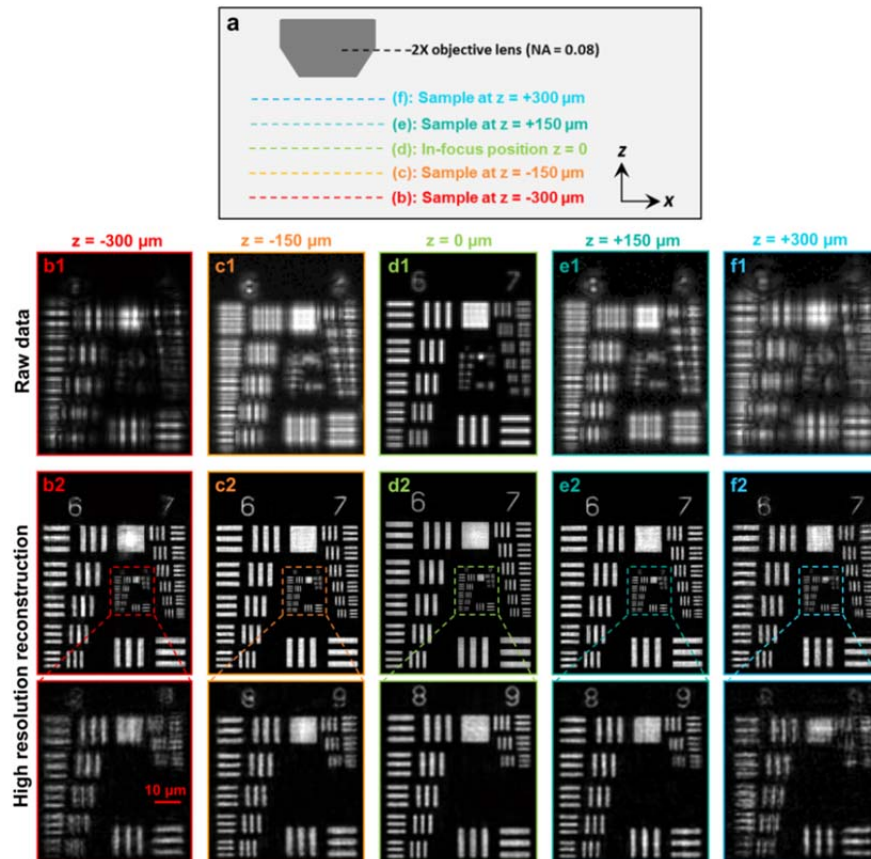


Figure 2-6 (color): Extending imaging depth by digital refocusing. (a) The USAF target is moved to different z positions with defocused distances ranging from $-300 \mu\text{m}$ to $+300 \mu\text{m}$. (b1)-(f1) Low-resolution raw data corresponding to different defocused distances. (b2)-(f2) High-resolution reconstructed images with digital refocusing.

In Fig. 2-6, we performed an experiment to validate such a capability of NAM. We first moved the sample (USAF target) to different z positions with defocused distances ranging from $-300 \mu\text{m}$ to $+300 \mu\text{m}$, as shown in Fig. 2-6(a). We then acquired low-resolution images (corresponding to 137 different LEDs) for all these defocused positions, as shown in Fig. 2-6(b1)-(f1). Finally, we reconstructed high-resolution intensity profiles of the sample in Fig. 2-6(b2)-(f2), following the recovery procedure discussed before. Line

traces of the reconstructed images are also provided in Fig. 2-7. From these reconstructed images, we can see that the proposed NAM method is capable for achieving resolution-invariant imaging depth of 0.3 mm. In Fig. 2-8, we further compared the case of image reconstructions with and without digital refocusing.

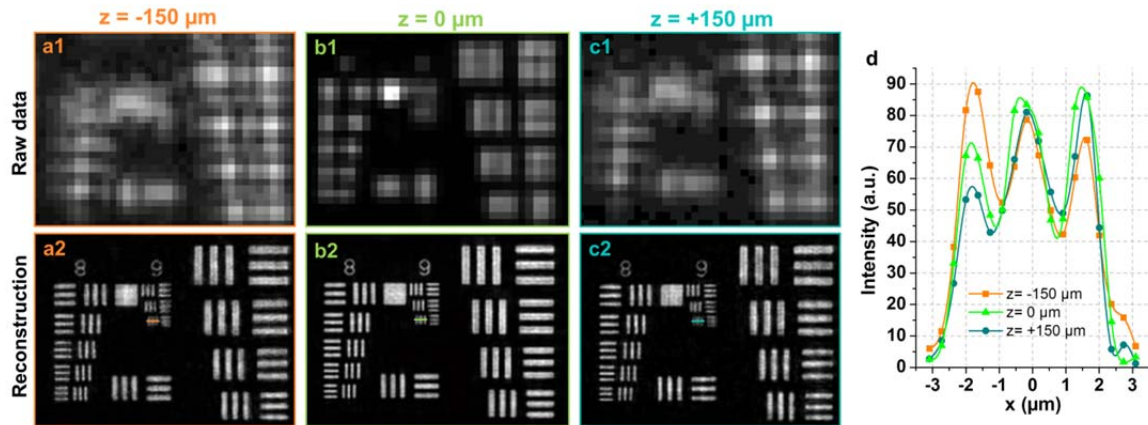


Figure 2-7 (color): Characterization of the imaging-depth of the NAM platform. (a1)-(c1) Low-resolution raw data corresponding to different defocused distances. (a2)-(c2) High-resolution reconstructed images with digital refocusing. (d) Line traces for the smallest features in (a2)-(c2).

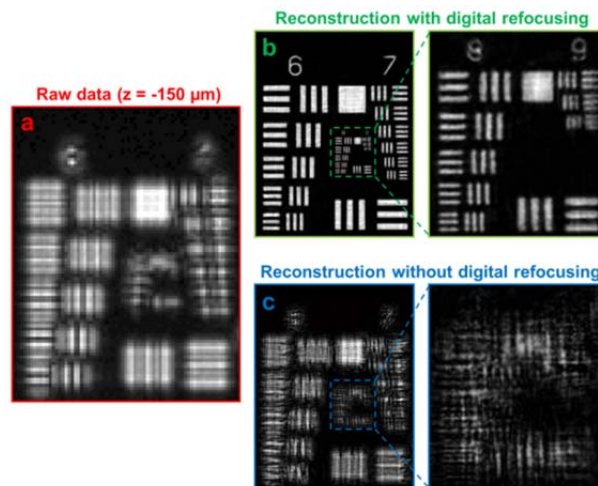


Figure 2-8 (color): Comparison between cases with and without digital refocusing. (a) The raw data taken at position $z = -150 \mu\text{m}$. High resolution reconstructions with (b) and without (c) digital refocusing.

2.3.3 Auto-focusing index

In real applications, the exact z -position of the sample is not a priori knowledge. To address this problem, we defined a parameter to locate the z -position of the sample automatically. We called such a parameter ‘auto-focusing index’, and it is defined by the following equation:

$$\text{Auto-focusing index} = 1 / \sum (\sqrt{I_{lf}} - \sqrt{I_{lfm}}) \quad (2-2)$$

, where $\sqrt{I_{lf}}$ is the amplitude image from the low-pass filtering, $\sqrt{I_{lfm}}$ is the actual low-resolution measurement. The summation in Eq. (2-2) is for all oblique incidences. The logic behind Eq. (2-2) is that the solution converges better for a correct z -position. In other words, if the sample is placed at $z_0 = 100 \mu\text{m}$ and we try to reconstruct the high-resolution image assuming $z_0 = -100 \mu\text{m}$, the solution won’t converge (corresponding to a smaller auto-focusing index).

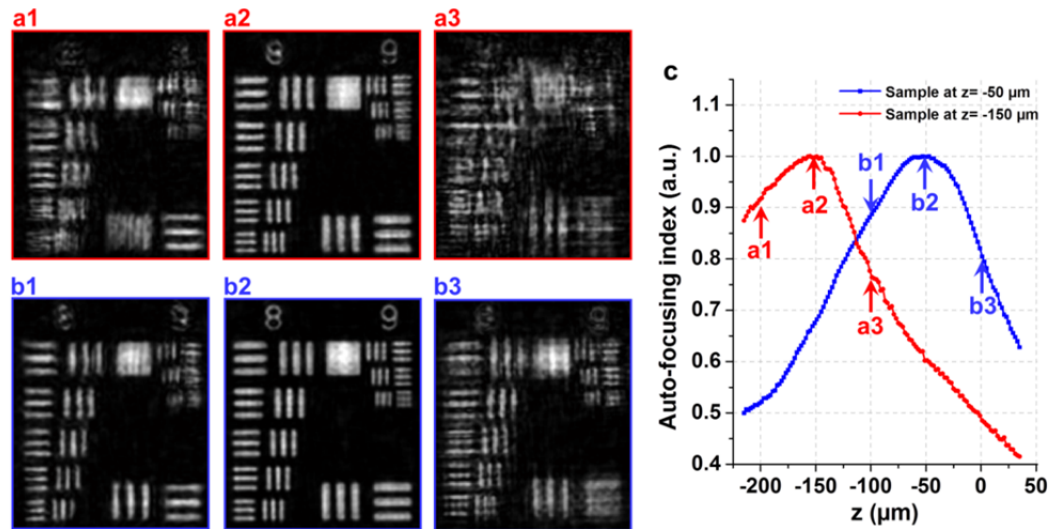


Figure 2-9 (color): Auto-focusing index for locating the axial position of the sample automatically. (a1)-(a3) Different reconstructions for the sample placed at $z_0 = -150 \mu\text{m}$. (b1)-(b3) Different reconstructions for the sample placed at $z_0 = -50 \mu\text{m}$. (c) The maximum values of the auto-focusing index indicate the estimated z -positions of the sample, which are in a good agreement with the actual values.

Fig. 2-9 demonstrates the use of the auto-focusing index for locating the axial position of the sample automatically. We first placed the sample at $z_0 = -150 \mu\text{m}$. We then calculated the auto-focusing index for different z -positions. The maximum value of the auto-focusing index indicates the estimated z -position of the sample, as shown in Fig. 2-9 (a) and (c) (color code: red). We then repeat the experiment by placing the sample at $z_0 = -50 \mu\text{m}$, as shown in Fig. 2-9(b) and (c) (color code: blue). We can see that the estimated positions are in a good agreement with the actual positions of the sample.

The capability to perform digital refocusing via the proposed NAM method represents another significant improvement over the conventional microscope platform, especially for 1) cases where samples are not perfectly aligned over the entire FOV, and for 2) correcting chromatic aberrations digitally (assigning different defocused distances for different colors).

2.4 Demonstration of imaging capabilities of NAM

In this section, we demonstrate imaging capabilities of the NAM method for biological applications. Two samples were used for this purpose: one is a blood smear (human chronic lymphocytic leukemia smear, Carolina) and the other is a pathology slide (human adenocarcinoma of breast section, Carolina).

2.4.1 High-resolution intensity and phase imaging via NAM

In section 2.2, we have demonstrated, through simulations, the capability of the NAM method for recovering both the intensity and phase profiles of a sample. In this section, we verify such a capability through two biological samples. The first sample is the blood smear, with the result shown in Fig. 2-10; the second sample is the pathology slide, with the result shown in Fig. 2-11. The experimental setting for acquiring these two figures is the same as before. From these two figures, we can clearly see the resolution improvement provided by the NAM method. We also note that, in Fig. 2-11(b) and (c), the reconstructed high-resolution phase image reveals different details of the sample (refer to the region

highlighted by the black arrow; such a feature will be further verified using a conventional microscope in Fig. 2-15).

The ability to perform phase imaging is useful in numerous applications. For example, phase profile of a histopathology slide contains information about the molecular scale organization of tissue and can be used as an intrinsic marker for cancer diagnosis [13]. Phase information of a sample can also be used to measure the optical path length of cells or organelles [14], to determine the growth pattern of cell cultures [15] or to perform blood screening [16]. Currently, most of full-field phase imaging techniques involve the use of interferometry in one form or another. As such, these platforms require fairly sophisticated and well-designed optical alignments.

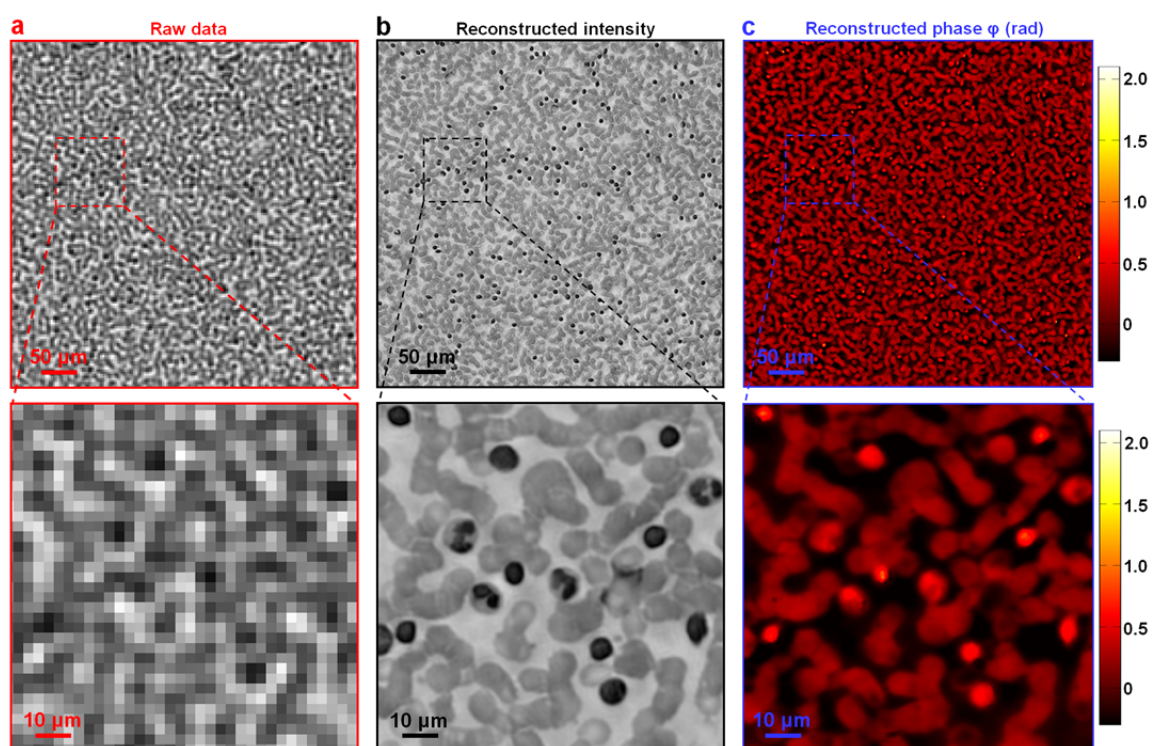


Figure 2-10 (color): High-resolution intensity and phase imaging via NAM (blood smear). (a) The low-resolution raw data of a blood smear. Reconstructed high-resolution intensity (b) and (c) phase profiles.

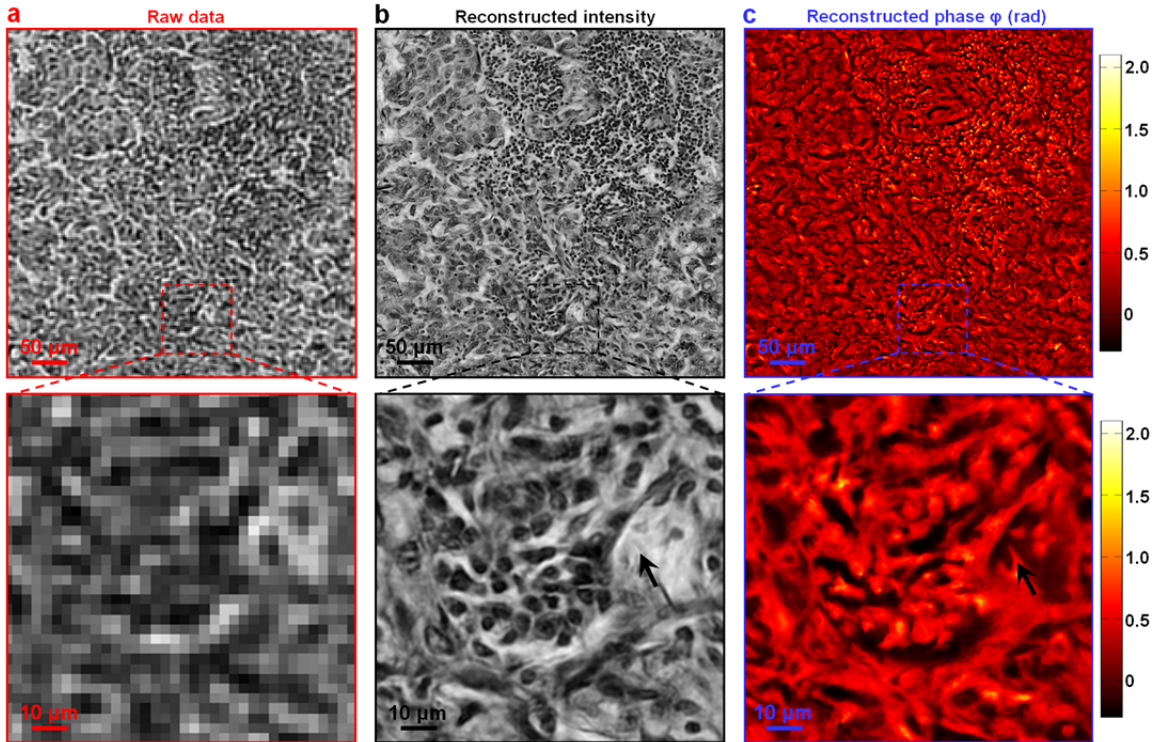


Figure 2-11 (color): High-resolution intensity and phase imaging via NAM (pathology slide). (a) The low-resolution raw data of a pathology slide. Reconstructed high-resolution intensity (b) and (c) phase profiles. The region highlighted by the black arrow reveals different details of the sample.

Compared to conventional interferometry-based phase imaging techniques, the proposed NAM method represents an easy and cost-effective solution for researchers and clinicians to incorporate phase imaging functionality into their current microscope systems. Based on NAM, specialized phase microscopy techniques become accessible to average microscopists or even high school students.

2.4.2 Parallel computing and image blending for large data sets

In Section 2.2, we have discussed the image recovery procedure and its associated computational cost. However, when it comes to large data sets, extra steps are needed to further accelerate the recovery process and optimize memory accesses. In this sub-section, we discuss two extra steps we used for reconstructing the full FOV image in the NAM

platform. In the first step, we divided the full FOV raw image (5320 by 4370 pixels) into smaller portions (196 by 196 pixels). Each small portion was independently processed by the recovery procedure discussed in section 2.2. In the second step, we combined the recovered images of different portions by alpha blending [17]. Fig. 2-12 demonstrates the image-blending process for creating the final full FOV gigapixel image. From the blending result shown in the right-hand side of Fig. 2-12, we can see that there is no observable boundary in the stitching region (the width of the blending region equals to the size of 6 raw pixels).

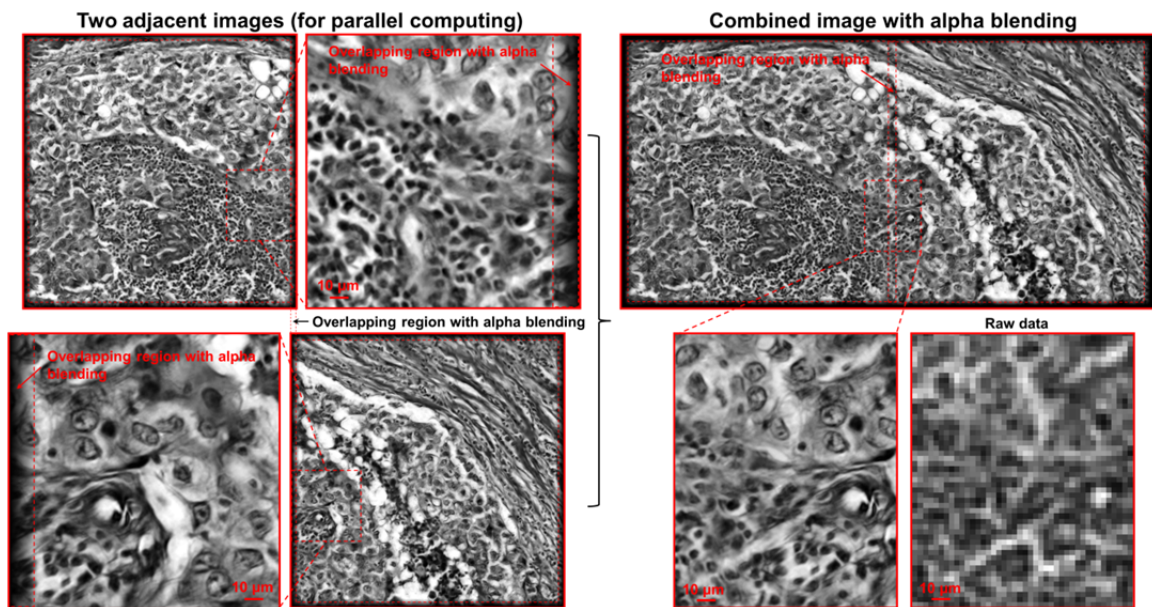


Figure 2-12 (color): Demonstration of image blending. The large format raw image (5320 by 4370) was divided into smaller portions (196 by 196 pixels) for parallel computing. Images in the left are two adjacent recovered images (1960 by 1960 pixels) and the right one is the combined image by alpha blending. No observable boundary is presented in the stitching region.

Benefits of these two extra steps lie in threefold: 1) each small portion of the raw image can be processed independently, a requirement for parallel computing; 2) reduce the memory requirement of the computer; 3) the light from LEDs can be treated as plane waves.

Using a personal computer with an Intel i7 CPU, the processing time for each small image (converting 196 by 196 raw pixels to 1960 by 1960 pixels) is ~4 seconds with Matlab. The processing time for creating the entire full FOV image is ~10 mins by parallel computing (using all 4 cores of the CPU). To further reduce the processing time, there are two solutions: 1) use a GPU unit. A GPU unit can reduce the processing time by at least 10 folds, since the major operation in our recovery process is FFT. 2) Implement the algorithm using other low-level programming language, such as C++.

2.4.3 Gigapixel color imaging via NAM

To demonstrate the application of the NAM method for high-throughput digital pathology, we acquired a 1.6 gigapixel color image of a pathology slide in Fig. 2-13.

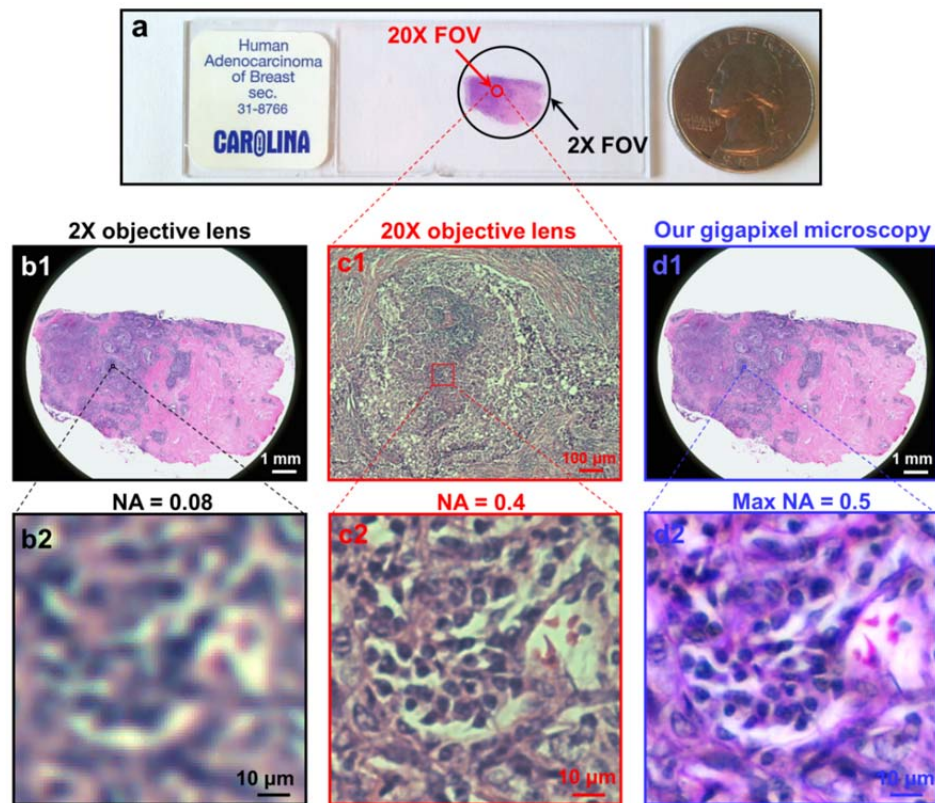


Figure 2-13 (color): Gigapixel color imaging via NAM. (a) FOVs of the slide for 2X and 20X objective lenses. (b) FOV and the corresponding NA of a 2X objective. (c) FOV and the corresponding NA of a 20X objective. (d) FOV and the corresponding NA of our gigapixel microscope platform.

Fig. 2-13(a) shows two different FOVs of the slide for 2X and 20X objective lenses (indicated by the black and red arrows). For the case of 2X objective lens, the FOV is ~ 13.25 mm in diameter and the corresponding NA is 0.08, as shown in Fig. 2-13(b). On the other hand, the NA of a 20X objective is 0.4, much larger than that of a 2X lens, while the corresponding FOV is only 1.1 mm in diameter, as shown in Fig. 2-13(c). The high-throughput imaging performance of our platform is demonstrated in Fig. 2-13(c). The FOV of our platform is the same as the 2X lens (i.e., 13.25 mm in diameter) while the maximum NA is ~ 0.5 , resulting in more than 1.6 gigapixel across the entire image by Nyquist rate (also refer to Section 2.2.3). Fig. 2-14 further demonstrates the use of digital refocusing for correcting the chromatic aberration and creating the high-resolution color image. As shown in Fig. 2-14 (a)-(c), raw data for red, green and blue colors are refocused to z-positions of $-70 \mu\text{m}$, $28 \mu\text{m}$, and $-16 \mu\text{m}$ for high-resolution reconstructions.

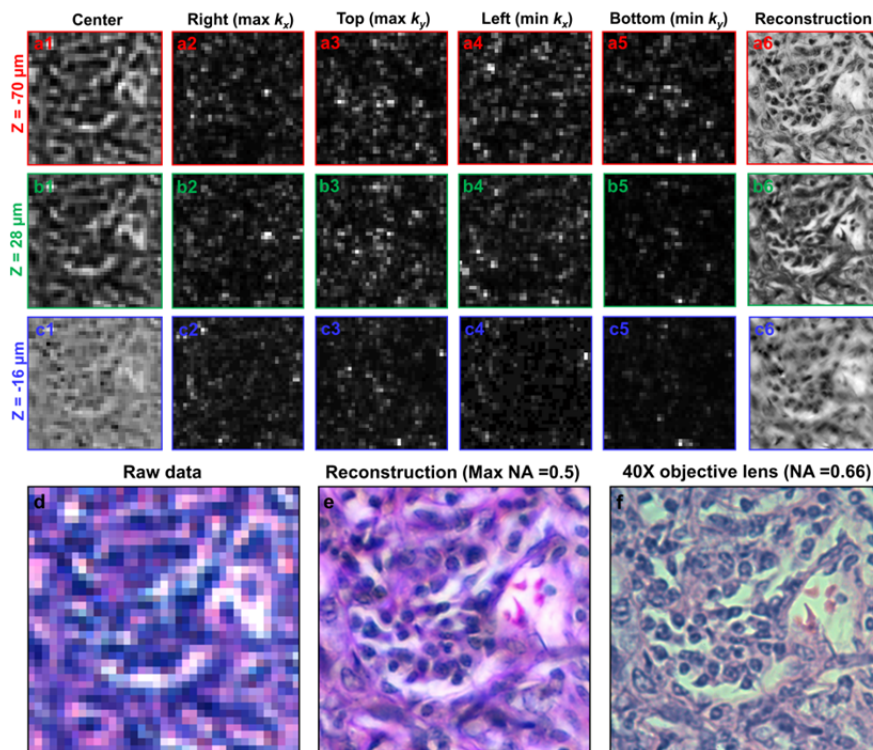


Figure 2-14 (color): Comparison between the raw data and the recovered color image with NAM. Raw data and the corresponding reconstructed images are shown in (a) for red, (b) for green and (c) for blue. (d) The raw color image. (e) The recovered color image with digital refocusing. (f) Image captured by a 40X objective lens and a color image sensor.

In this example of gigapixel color imaging, we use 137 different LED light sources for illuminations. For each LED, at least two images are captured with a different exposure time. These images are then combined to form a high dynamic-range image. The total acquisition time is ~ 3 mins for each color, mainly limited by the low light intensity of the LED matrix. With a brighter LED matrix, the acquisition time can be reduced to ~ 50 seconds with the same CCD in the current setup (maximum frame rate of the CCD: 5.5 fps). We note that, there is no theoretical limit on the throughput of the proposed platform. The practical limit is the data transfer rate of the image sensor.

To further validate the performance of the proposed gigapixel imaging platform, a detailed comparison of image-quality between NAM and different objective lenses is given in Fig. 2-15.

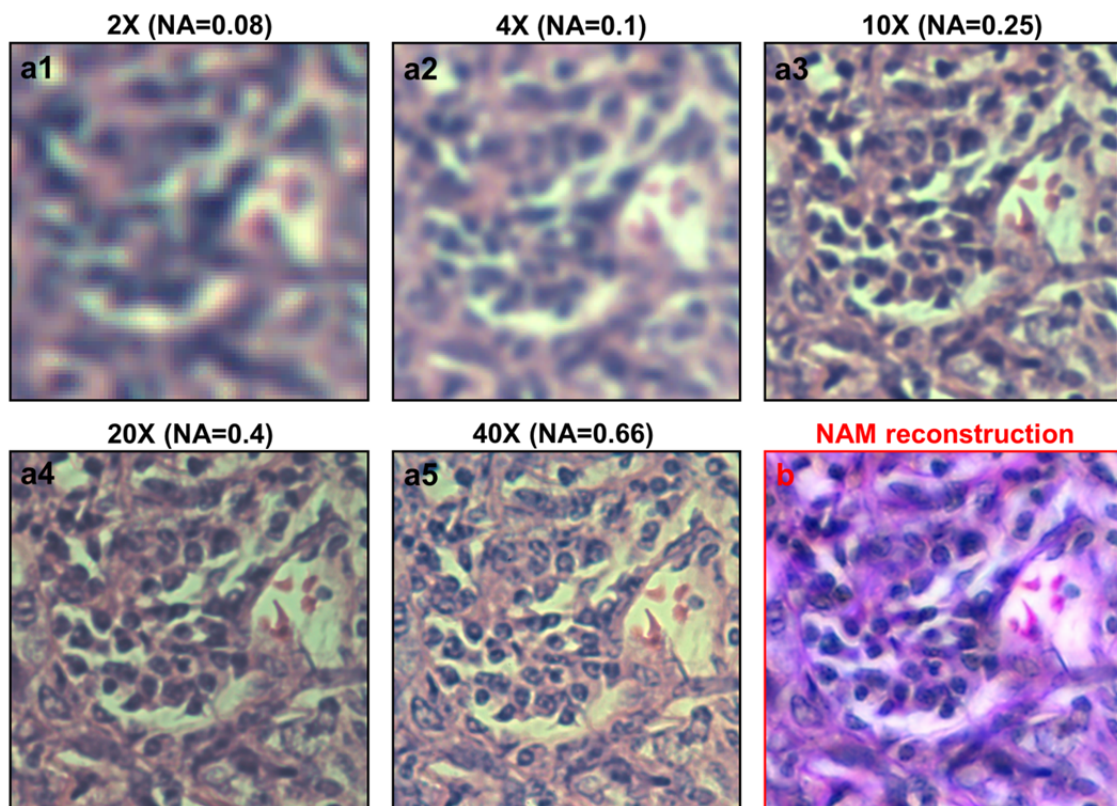


Figure 2-15 (color): Comparison of image quality between NAM and different objective lenses. Image captured by a 2X (a1), 4X (a2), 10X (a3), 20X (a4) and 40X (a5) objective lenses. (b) The recovered color image of NAM.

2.5 Discussions

To summarize, we have demonstrated a simple and cost-effective high-throughput microscopy imaging method named Non-interferometric Aperture-synthesizing Microscopy (NAM). Such a method is able to break the spatial-bandwidth product barrier of a conventional microscope without involving any mechanical scanning. Based on NAM, we demonstrated a 1.6 gigapixel microscope platform with a maximum NA of 0.5, a FOV of 120 mm², and a resolution-invariant imaging depth of 0.3 mm. The acquired images using NAM are closely comparable to those obtained with a conventional microscope.

There are several advantages associated with the proposed NAM method that are worth noting:

1) Compatible to most existing microscopes. In the NAM method, we only need to capture low-resolution intensity images of the sample (i.e., non-interferometric measurements). No phase measurement is needed in the data acquisition process. The setup configuration is the same as the conventional microscope platform.

2) Simple, cost-effective and high-throughput. The only modification we made to the conventional microscope platform is to add a LED matrix under the sample stage. Such an LED matrix is commercially available and in low-cost (~\$20). With this simple modification, we are able to increase the throughput of most existing microscopes by two orders of magnitude.

3) No mechanical scanning involved. Different from other synthetic-aperture and scanning-based wide FOV microscopy techniques, mechanical scanning is not needed in the proposed NAM method. As such, it simplifies the platform design, reduces associated costs and allows for a higher throughput limit. We note that the practical throughput limit of the NAM method is only determined by the data transfer rate of the camera.

4) Capable for digital refocusing. To achieve the optimal resolution in the conventional microscope platform, one needs to use a stage to mechanically bring the sample back into focus. In the proposed NAM method, such a sample focusing step can be done digitally rather than mechanically. We demonstrated, with both simulations and experiments, that the proposed NAM platform is capable for achieving resolution-invariant imaging depth of 0.3 mm. The ability to perform digital refocusing via the proposed NAM

method represents another significant improvement over the conventional microscope. It is especially useful for cases where samples are not perfectly aligned over the entire FOV. We also demonstrated the application of digital refocusing for correcting chromatic aberrations of the optics.

5) Capable for color imaging. High-throughput color imaging is considered pivotal in digital pathology, histology, and immunochemistry. In our NAM platform, color imaging can be easily achieved via a color LED matrix. The reconstructed image is also free from chromatic aberrations of the optics (by digital refocusing).

6) Capable for phase imaging. Phase profile of a biological sample contains information about the molecular scale organization of sample and can be used as an intrinsic marker for different applications. The ability to perform phase imaging is also useful for digital image processing, such as cell segmentation and cell counting. Currently, most of full-field phase imaging techniques require fairly sophisticated and well-designed optical alignments. The proposed NAM method provides an easy and cost-effective solution for researchers and clinicians to incorporate phase imaging functionality into their current microscope systems. Based on NAM, specialized phase microscopy techniques become accessible to average microscopists or even high school students.

7) Throughput scalable. We have demonstrated that, resolution and FOV were not coupled in the NAM method. To scale the proposed NAM method for higher throughput, one can simply use a lower NA objective lens with more LED illuminations.

8) The proposed NAM method can also be extended to other spectrum such as THz and X-ray regions, where lenses are poor and of very limited numerical aperture.

There are three future improvements that are worth further investigations:

1) In the current platform, the acquisition time for a 1.6 gigapixel image is about 3 mins, limited by the low light intensity of the LED. The implementation with a brighter LED matrix will cut down the acquisition time to ~50 seconds.

2) The image processing time for a 1.6 gigapixel image is about 10 mins. We can shorten this number significantly by GPU-assist processing.

3) By integrating the tomography reconstruction technique into the proposed method, we can potentially extend the NAM for 3D imaging.

Bibliography

- [1] J. Di, J. Zhao, H. Jiang *et al.*, "High resolution digital holographic microscopy with a wide field of view based on a synthetic aperture technique and use of linear CCD scanning," *Appl. Opt.*, vol. 47, no. 30, pp. 5654-5659, 2008.
- [2] T. R. Hillman, T. Gutzler, S. A. Alexandrov *et al.*, "High-resolution, wide-field object reconstruction with synthetic aperture Fourier holographic optical microscopy," *Opt. Express*, vol. 17, no. 10, pp. 7873-7892, 2009.
- [3] L. Granero, V. Micó, Z. Zalevsky *et al.*, "Synthetic aperture superresolved microscopy in digital lensless Fourier holography by time and angular multiplexing of the object information," *Appl. Opt.*, vol. 49, no. 5, pp. 845-857, 2010.
- [4] M. Kim, Y. Choi, C. Fang-Yen *et al.*, "High-speed synthetic aperture microscopy for live cell imaging," *Opt. Lett.*, vol. 36, no. 2, pp. 148-150, 2011.
- [5] T. Turpin, L. Gesell, J. Lapidés *et al.*, "Theory of the synthetic aperture microscope." pp. 230-240.
- [6] C. J. Schwarz, Y. Kuznetsova, and S. Brueck, "Imaging interferometric microscopy," *Optics letters*, vol. 28, no. 16, pp. 1424-1426, 2003.
- [7] P. Feng, X. Wen, and R. Lu, "Long-working-distance synthetic aperture Fresnel off-axis digital holography," *Optics Express*, vol. 17, no. 7, pp. 5473-5480, 2009.
- [8] V. Mico, Z. Zalevsky, P. García-Martínez *et al.*, "Synthetic aperture superresolution with multiple off-axis holograms," *JOSA A*, vol. 23, no. 12, pp. 3162-3170, 2006.
- [9] C. Yuan, H. Zhai, and H. Liu, "Angular multiplexing in pulsed digital holography for aperture synthesis," *Optics letters*, vol. 33, no. 20, pp. 2356-2358, 2008.
- [10] V. Mico, Z. Zalevsky, and J. García, "Synthetic aperture microscopy using off-axis illumination and polarization coding," *Optics communications*, vol. 276, no. 2, pp. 209-217, 2007.
- [11] S. Alexandrov, and D. Sampson, "Spatial information transmission beyond a system's diffraction limit using optical spectral encoding of the spatial frequency," *Journal of Optics A: Pure and Applied Optics*, vol. 10, no. 2, pp. 025304, 2008.
- [12] U. Schnars, and W. P. O. Jüptner, "Digital recording and numerical reconstruction of holograms," *Measurement science and technology*, vol. 13, no. 9, pp. R85, 2002.
- [13] Z. Wang, K. Tangella, A. Balla *et al.*, "Tissue refractive index as marker of disease," *Journal of Biomedical Optics*, vol. 16, no. 11, pp. 116017-116017-7, 2011.
- [14] N. Lue, W. Choi, G. Popescu *et al.*, "Live Cell Refractometry Using Hilbert Phase Microscopy and Confocal Reflectance Microscopy†," *The Journal of Physical Chemistry A*, vol. 113, no. 47, pp. 13327-13330, 2009.
- [15] M. Mir, Z. Wang, Z. Shen *et al.*, "Optical measurement of cycle-dependent cell growth," *Proceedings of the National Academy of Sciences*, vol. 108, no. 32, pp. 13124-13129, 2011.
- [16] M. Mir, H. Ding, Z. Wang *et al.*, "Blood screening using diffraction phase cytometry," *Journal of Biomedical Optics*, vol. 15, no. 2, pp. 027016-027016-4, 2010.
- [17] E. S. Young, R. X. Zhao, A. Khurana *et al.*, "System and method for performing blending using an over sampling buffer," Google Patents, 2000.

Chapter 3

ePetri dish, an on-chip cell imaging platform

The active control of illumination sources can also be adapted for chip-scale microscopy imaging. In this chapter, we report on a chip-scale microscopy solution, termed Sub-pixel Perspective Sweeping Microscopy (SPSM) and demonstrate a proof-of-concept self-imaging digital Petri dish solution [1]. This on-chip platform has the ability to automatically image confluent cell sample with sub-cellular resolution over a large field-of-view. As such, it is well suited for long-term cell culture imaging and tracking applications. This chapter is structured as follows. We will first present our prototype setup and the principle of SPSM. Then, we will report on our large field-of-view on-chip imaging of Giemsa-stained confluent HeLa cell samples. We will then report on our experimental demonstration of long-term cell imaging and tracking of embryonic stem cell culture growth with the ePetri platform. Next, we will discuss the resolution and limitations of the SPSM method. Finally, we will discuss the application advantages of the ePetri platform.

3.1 Background

Recent rapid advances and commercialization efforts in CMOS imaging sensor has led to broad availability of cheap and high pixel density sensor chips. In the past few years, these sensor chips enabled the development of new microscopy implementations that are significantly more compact and cheaper than traditional microscopy designs. The optofluidic microscope [2-4] and the digital in-line holographic microscope [5-11] are two examples of these new developments. Both of these technologies are designed to operate without lenses and, therefore, circumvent their optical limitations, such as aberrations and chromaticity. Both technologies are suitable for imaging dispersible samples, such as blood, fluid cell cultures and other suspensions of cells or organisms. However, neither can

work well with confluent cell cultures or any sample in which cells are contiguously connected over a sizable length scale.

In the case of the optofluidic microscope, imaging requires the microfluidic flow of the specimens across a scanning area. Adherent cells are simply incompatible with this imaging mode. In digital in-line holographic microscopy, the interference intensity distribution of a target under controlled light illumination is measured and then an image reconstruction algorithm is applied to render microscopy images of the target. There have been two major types of algorithms that have been reported [12-14]. In both cases, the image quality depends critically on the extent of the target, the scattering property and the signal-to-noise ratio (SNR) of the measurement processes [6, 8, 9, 15-17]. The method works well for well-isolated targets, such as diluted blood smear slides. However, to our knowledge, such approaches have not been applied to targets that occupy more than 0.1 mm^2 in total contiguous area coverage with sub-micron resolution [5-8, 18]. The reason of this limitation is well-known: the loss of phase information during the intensity recording process. In order to recover the phase information, object support has to be used in the iterative phase recovery algorithm, which involves the light field propagation back and forth between the imaging domain (where the intensity data are applied) and object domain (where *a priori* object constrains are applied) [13]. When the test object is real or non-negative, it is easy to apply the powerful non-negativity support constraint to extract the phase information from the recorded diffraction intensity [13]. However, for digital in-line holography, light field in the object domain is complex valued, and therefore, the phase recovery is possible only if the support of the object is sufficiently isolated (i.e., sparsity constrains) [16, 17, 19, 20] or the edges are sharply defined (true boundary) [16, 17, 20]. Furthermore, the interference nature of the technique implies that coherence based noise sources, such as speckles and cross-interference, would be present and would need to be addressed [8, 9, 21]. While methods for mitigating these have reported [15, 16, 22, 23], the generated images are, nevertheless, identifiably different from images acquired with conventional microscopes due to coherence-based noise sources.

The need for a high-quality, autonomous and cost-effective microscopy solution for imaging confluent cell culture samples, especially for longitudinal studies, is a strong one

[24]. To name a few specific examples, the determination of daughter fates before the division of neural progenitor cells [25], the existence of haemogenic endothelium [26], neural and hematopoietic stem and progenitor divisional patterns and lineage choice [27, 28], the in-vitro tissue culture studies using the neutral red dye [29], the studies of dynamics of collective cell migration [30], detection of toxic compound [31], and drug screening [32, 33]. In these cases, the labor intensive nature of these experiments and the challenge of efficiently imaging large assays have typically plagued this type of experiment format.

A chip-scale microscopy method that can automatically image growing or confluent cell cultures can significantly improve Petri-dish-based cell culture experiments. In fact, with this approach providing a compact, low-cost and disposable microscopy imaging solution, we can start to transit Petri-dish-based experiments from the traditionally labor-intensive process to an automated and streamlined process. This technological shift from an inert Petri dish to a self-imaging Petri dish, which we term ePetri, is appropriately timely as well, because, the cost of high performance CMOS imaging sensors (which are widely used in cellphone cameras and webcams) have recently reached a price point where they can be used as recyclable or disposable components. We believe that such a self-imaging Petri dish, can significantly impact cell-culture-based procedures in both medicine and science.

3.2 Principle of sub-pixel perspective sweeping microscopy

The principle of SPSM is summarized in Fig. 3-1. In this method, we simply culture cells or place cells of interest directly on the surface of a CMOS image sensor. To start, consider an idealized image sensor that has a high density grid of infinitesimally small pixels. In such a case, as long as the cells are right on the sensor, this idealized sensor would be able to collect a high resolution shadow image of the cells with excellent acuity. Unfortunately, currently available sensor chips have rather large pixels (2.2 microns in our particular experiment). This implies that the direct shadow images we collect with our sensor chips are intrinsically coarse [34, 35]. Specifically, the raw shadow image resolution would be no better than two times the pixel size (as dictated by Nyquist criterion considerations). To

address this, we take the following approach to improve resolution or, more specifically in our case, to generate a denser grid of smaller virtual pixels.

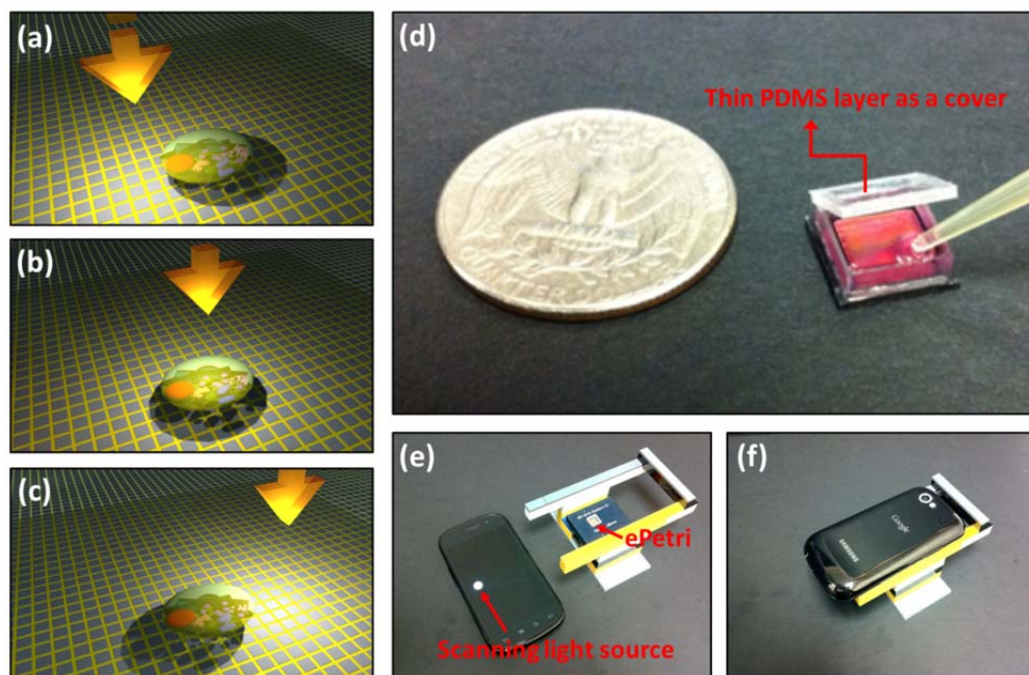


Figure 3-1: (color) Principle of SPSM and the ePetri prototype. (a-c) With the incremental tilt/shift of the illumination, the target cells' shadow will incrementally shift across the sensor pixels. These sub-pixel shifted low resolution images will be used to reconstruct the high resolution image by using pixel super resolution algorithm. (d) The ePetri prototype. A thin PDMS layer is used as a cover to prevent the evaporation of the culture media while allowing for CO₂ exchange between the well and exterior. (e-f) The ePetri imaging platform. We used the LED screen of a smartphone as the scanning light source. The holder is built with LEGO blocks.

First, we take note of the fact that there is a thin transparent passivation layer that separates the cells from the actual light sensitive region of the sensor chip. With this recognition in mind, we sequentially tilt/shift an incoherent illumination source above the sample and acquire a sequence of raw images. With the incremental tilt/shift of the illumination, the target cells' shadow will incrementally shift across the sensor pixels (Fig.

3-1(a-c)). The amount of shadow shift is proportional to the passivation layer thickness and the tilt/shift extent of the light source. As long as the shadow shift between each raw image frame is much smaller than the physical pixel size, we can then combine the information from multiple sub-pixel-shifted low resolution (LR) shadow images to create a single high resolution (HR) image with a pixel super-resolution algorithm [36-41].

The algorithm we used in this experiment is a simple, fast and non-iterative method [38] that preserves the estimation optimality in the Maximum-Likelihood sense. In this note, we briefly describe the general pixel super resolution model and solution. Detailed description can be found in Ref. [37-39, 41]. We denote the N measured low-resolution images by $Y_k (k = 1, 2 \dots N)$. These images are used to reconstruct a single improved high resolution image, denoted as X . The images are all represented by lexicographically ordered column vectors. The low resolution image can be modeled by the following equation

$$Y_k = DHF_k X + V_k (k = 1, 2 \dots N) \quad (3-1)$$

The matrix F_k stands for the sub-pixel shift operation for the image X . The matrix H is the pixel transfer function of the image sensor. The matrix D stands for the decimation operation, representing the reduction of the number of observed pixels in the measured images. V_k represents Gaussian additive measurement noise with zeros mean and auto-correlation matrix $W_k = E\{V_k V_k^T\}$.

The Maximum-Likelihood estimation of X can be described as following expression

$$\hat{X} = \text{ArgMin}\{\sum_{k=1}^N (Y_k - DHF_k X)^T W_k^{-1} (Y_k - DHF_k X)\} \quad (3-2)$$

And the closed-form solution for \hat{X} is shown to be

$$\hat{X} = H^{-1} R^{-1} P \quad (3-3)$$

, where $R = \sum_{k=1}^N F_k^T D^T D F_k$, $P = \sum_{k=1}^N F_k^T D^T Y_k$. It can be proved that, R is a diagonal matrix and the computation complexity of this approach is $O(n \cdot \log(n))$, where n is the number of pixels. For readers interested in building their own ePetri, a free Matlab-based super-resolution software package can be downloaded at Ref. [42].

Our ePetri prototype based on SPSM imaging, is shown in Fig. 3-1(d). This prototype was built on a commercial available CMOS image sensor with a 6mm*4mm

imaging area filled with 2.2 micron pixels (Aptina MT9P031). The microlens layer and color filter on the sensor surface were removed to provide us with direct access to the sensor pixels. In a separate experiment, we determined that the sensor top passivation layer was about 0.9 μm thick. We glued a home-made square plastic well to the image sensor with poly-dimethylsiloxane (PDMS) (see Methods for details). We then used a thin PDMS layer ($\sim 100 \mu\text{m}$) as a cover for this ePetri prototype. The thin PDMS layer served to prevent the evaporation of the culture media while allowing for CO_2 exchange between the well and exterior. For illumination, we used the LED screen of a smartphone as the scanning illumination light source, as shown in Fig. 3-1(e-f). A holder was built with LEGO building blocks to house the image sensor socket board and the smartphone. The screen of smartphone was set at about 2.0 cm away from the image sensor. In this method, the alignment between the smartphone and the image sensor is not a critical consideration. During imaging, we arranged the perspective illumination angle from -60 degree to +60 degree with respect to the surface of the image sensor. The entire platform can be placed in an incubator for automatic long term cell imaging and tracking, as we shall report in a later section. Fig. 3-2 shows the scanning pattern on the smartphone screen.

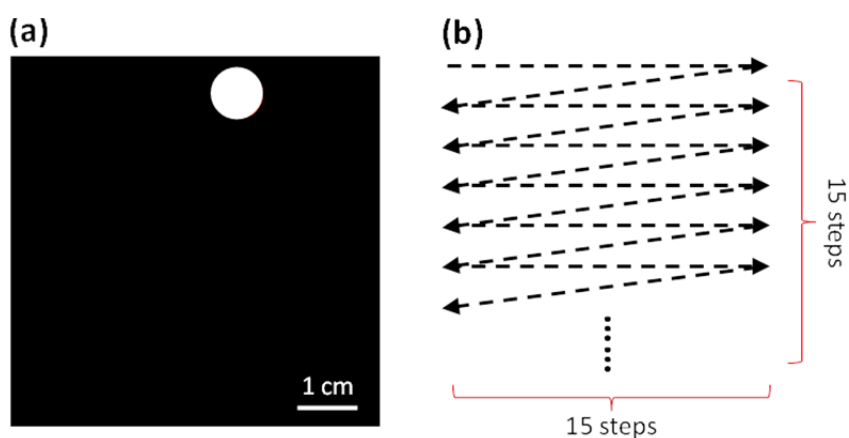


Figure 3-2 (color): (a) The scanning pattern on the smartphone screen, with 640*640 pixel size. (b) We use 15*15 steps for illumination. When the bright spot moves away from the center of smartphone screen, the readout from the image sensor chip will decrease because of the large incident angle; therefore, in our setup, the bright spot size linearly increases when it moves away from the center of the screen.

We used a smartphone screen as illumination to highlight the point that the light intensity requirement of this imaging scheme is low. The scheme can flexibly work with a LED display panel, a television screen or a LED matrix. In our experiments, the average light intensity incident on a sensor pixel was 0.015 W/m^2 . As a point of reference, a halogen-lamp-based conventional microscope typically delivers intensity of 20 W/m^2 on a sample.

3.3 Wide field-of-view cell imaging using ePetri

In this section, we demonstrate the ability of the ePetri prototype to image confluent cell samples and perform longitudinal cell study from within an incubator.

3.3.1 Color imaging of the stained confluent cell sample

To demonstrate the ability of this ePetri prototype to image confluent cell samples, we cultured HeLa cells on the ePetri platform (Fig. 3-1(f)) for about 48 hours. The sample was then stained with Giemsa (detailed procedures of fixation and staining are explained in the Methods section). The entire image area was $6 \text{ mm} \times 4 \text{ mm}$. We used 15×15 scanning steps for each color illumination. The image capture rate was set at 10 frames per second with the pixel clock of the image sensor running at 70 MHz. The entire data acquisition process took about 20 seconds.

Fig. 3-3(a) shows the reconstructed color image of the confluent HeLa cell sample. The image enhancement factor used in the algorithm to generate the image was set at 13. In other words, each pixel at the low-resolution raw image level ($2.2 \mu\text{m}$) was enhanced into a 13×13 pixel block in the reconstructed image. The entire image of Fig. 3-3(a) contains about 8.45×10^8 pixels. The prototype took about 22 second to capture each raw image set for each color. Given the sheer amount of data generated, the data transfer rate of $\sim 100 \text{ MB/s}$ between the image sensor and the computer via Ethernet connection imposed a throughput limit. After transferring the raw data into the computer, it took us 2-3 minutes to reconstruct the entire high-resolution image using a personal computer with an Intel i7 CPU. We note that, the solution for the reconstructed image was non-iterative, deterministic and was optimized in the Maximum-Likelihood sense. The relative long time

for image reconstruction was simply attributable to the fact that we were dealing with a large amount of data. However, with the use of a GPU unit, we expect the image processing time can be cut down to less than one second for the entire image. As we believe the primary use of ePetri would be for tracking cell culture growth directly from within an incubator, we do not believe that the current data transfer limitation or the current processing speed of the prototype will be the bottleneck for the proposed platform.

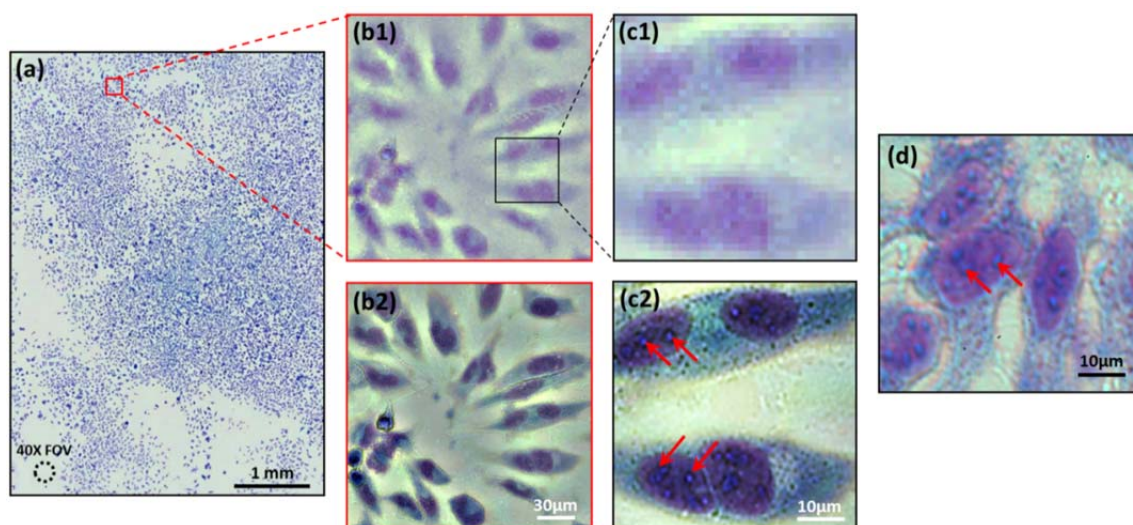


Figure 3-3 (color): (a) Large-field-of-view color imaging of the confluent cell sample. The field of view of a 40X objective lens is also shown in left bottom. (b1) and (c1), raw images of a small region of (a). (b2) and (c2), the reconstructed high resolution images corresponding to (b1) and (c1). (d) The conventional microscopy image, with 40X objective lens (0.66 N.A.), acquired from similar cells cultured on a Petri dish. The slightly color difference between (d) and (c2) may due to the reflective surface of the image sensor of the ePetri platform.

The amount of details in the reconstructed color image is too large to fully display on a computer screen or print on a printer; we have provided vignette views of selected regions for comparison in Fig. 3-3. Fig. 3-3(b1) and (c1) show the raw images from a small region of Fig. 3-3(a). Fig. 3-3(b2) and (c2) shows the corresponding reconstructed high resolution image of (b1) and (c1). From the reconstructed high resolution image in

Fig. 3-3(b2) and (c2), we can readily discern organelles within the HeLa cell, such as multiple nuclear granules (indicated by red arrows), and the nucleus. The images also closely corresponded to conventional microscopy images acquired from similar cells cultured on a Petri dish (see Fig. 3-3(d), image acquired with an Olympus BX 51 microscope with a 40X, NA = 0.66 objective). This strongly indicates that the ePetri can directly replace and improve (by providing a wide field-of-view) upon the conventional microscope for cell culture analysis. The comparison between the conventional microscopy image and the image acquired by the ePetri is shown in Fig. 3-4.

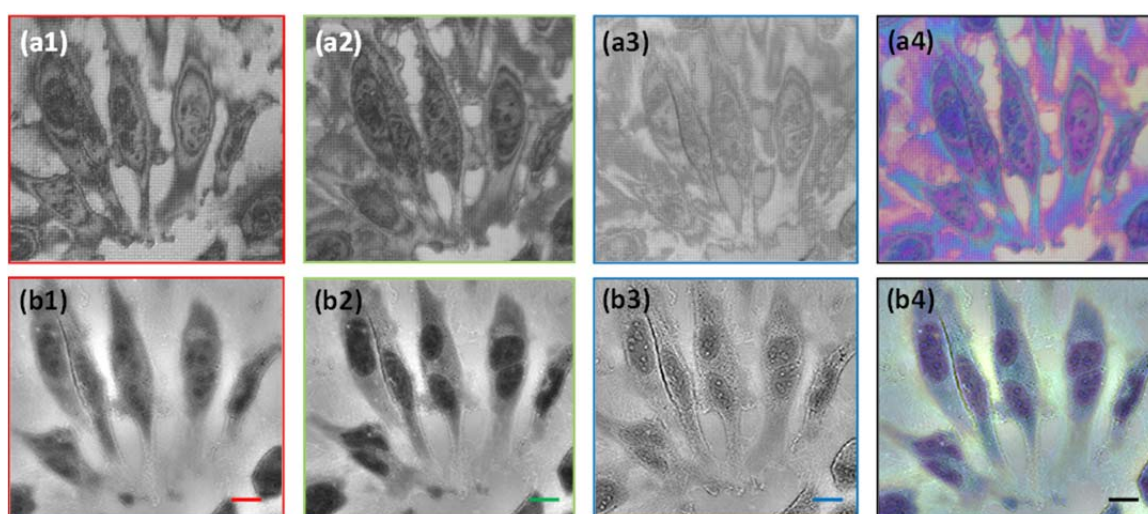


Figure 3-4 (color): The comparison between the conventional microscopy image (in reflection mode) and the image acquired by the ePetri platform. The HeLa cells were cultured on a CMOS sensor chip, fixed and stained with Giemsa. (a1-a3): the conventional microscopy images with red, green and blue LED illuminations (Olympus BX41 with a 20X objective, 0.5 N.A.). (a4) is the color image based on (a1) to (a3). Note that, the sensor chip is not transparent, and thus, these microscopy images are taken in the reflection mode. The color we saw in (a4) is due to the light interference between the sensor surface and sample. The grid pattern in (a1) to (a4) is the pixel array of the image sensor (2.2 μm pixel size). (b1) to (b3): the reconstructed high resolution images of ePetri platform under the red, green, blue light source scanning. (b4) is the reconstructed color image based on (b1) to (b3). Scale bar = 20 μm .

3.3.2 Longitudinal cell imaging and tracking

The ePetri platform can also be used to perform longitudinal cell imaging and study from within an incubator. Two experiments were performed to demonstrate such a capability. In the first experiment, we seeded HeLa cells onto the ePetri and the entire imaging platform (as shown in Fig. 3-5(b)) was placed into the incubator. An Ethernet cable connected our prototype to a personal computer outside the incubator for data transfer. In this experiment, we took a complete image set at 15 minutes interval for the entire growth duration of 48 hours. The number of cells grew from 40+ to hundreds in this period. Fig. 3-5 (a) shows the reconstructed images of the cells from a specific sub-location acquired at $t = 10\text{hr}$, $t = 17.5\text{hr}$, $t = 25\text{hr}$ and $t = 32.5\text{hr}$. Based on the time-lapse cell imaging data, we can detect and track each individual cell's movements in space and time, and generate corresponding lineage trees (i.e., mother-daughter relationship). For example, Fig. 3-5(c) shows tracking trajectories of three cell families annotated by a biologist. The lineage trees for these cell families are also shown in Fig. 3-5(c).

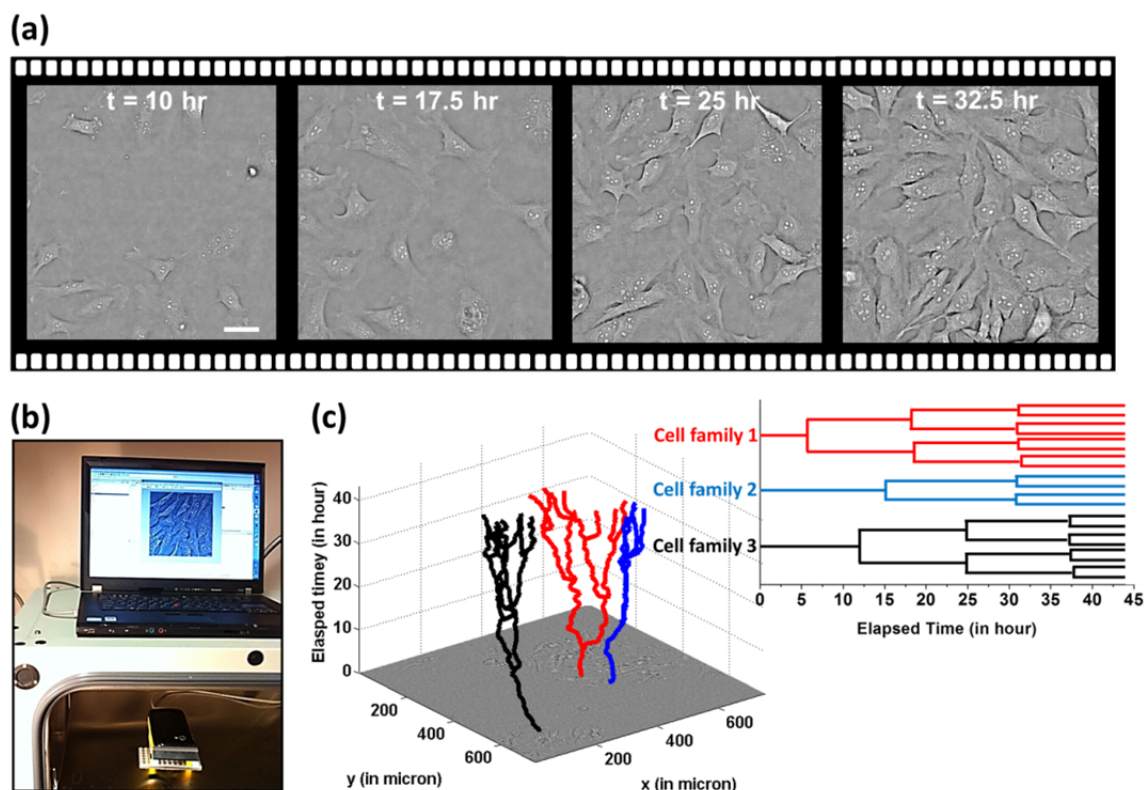


Figure 3-5 (color): (a) Time-lapse imaging of HeLa cell culture on the ePetri platform. Scale bar 20 μm . (b) The experimental setup. The ePetri platform was placed into the incubator; the data was read out by an Ethernet cable to a personal computer. A customized program was created to automatically reconstruct and display the image onto the screen for user monitoring. (c) The tracking trajectories of three cell families and the corresponding lineage trees for these cell families.

In order to further demonstrate the versatility of the ePetri as a general platform for culturing various types of cells, we perform a second experiment using embryonic stem (ES) cells. These cells are derived from the inner cell mass of developing embryos. ES cells offer tremendous biomedical potential on two inter-related levels: first, they provide a model system for uncovering the fundamental mechanisms governing cell fate decision-making and differentiation; second, they are the basis for a new generation of regenerative therapies for a wide range of neurodegenerative, autoimmune, and hematopoietic diseases, among others.

In order to visualize the process of stem cell differentiation and the spatial heterogeneity in cell fate decisions, we cultured them on ePetri and followed changes in cell morphology during the differentiation process. We used the E14 mouse ES cell line as a specific example of ES cells. We cultured E14 mouse ES cells in vitro and imaged them both under stem cell maintaining conditions and under differentiation-inducing conditions. Initially, we imaged stem cells while maintaining their pluripotent state. For this stage, cells were resuspended using 0.25% trypsin plated and 10^4 cells were plated on the ePetri chip (2×10^4 cells per cm^2). We pre-coated the ePetri with fibronectin (5 $\mu\text{g}/\text{ml}$) for 3 hours prior to plating the cells, in order to allow cells to adhere efficiently to the sensor surface. Cells were then maintained in a standard stem cell medium (High glucose DMEM, supplemented with 15% FBS, L-glutamine/Pen/Strep, NEAA, sodium pyruvate, and 0.1 mM 2-mercaptoethanol) enriched with LIF (1000U/ml, Millipore) in order to sustain pluripotency. The media were replaced daily to resupply nutrients and maintain a proper pH level. In the differentiation stage, cells were first plated at low density (~ 5000 cells) on a fibronectin-coated ePetri. Initially, cells were maintained in pluripotency-sustaining media for 24 hours to allow adherence of the cells. After that point, the media was replaced with N2B27, a defined serum free media. In order to induce differentiation, pluripotency-sustaining signaling molecules were not included. Media were being replaced every two days until cells differentiated and began to exhibit various morphologies.

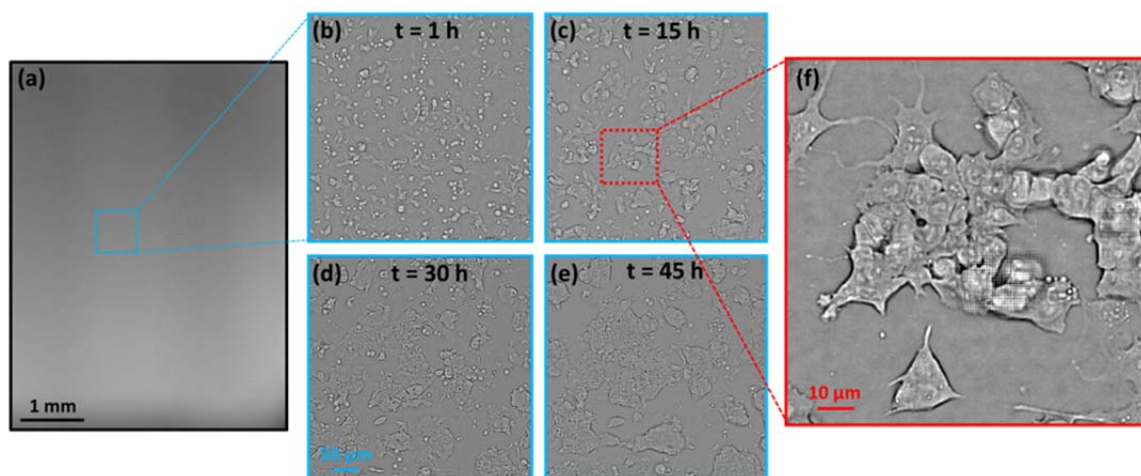


Figure 3-6 (color): Time-lapse imaging of first-stage embryonic stem cell culture on the ePetri platform. For this stage, cells were maintained in a standard stem cell medium.

Initially, we imaged stem cells while maintaining their pluripotent state, as shown in Fig. 3-6. Then, in the second stage of this experiment, we imaged the differentiation process and the dynamical morphological changes in stem cells. Media were being replaced every two days until cells differentiated and began to exhibit various morphologies.

Fig. 3-7 (a) shows the reconstructed images of ES cells at the differentiation stage. Fig. 3-7(b1)-(b9) show a specific sub-location (corresponded to cell type 1) acquired at different time. We were able to identify at least three cell variations in the reconstructed image (denoted by arrow in Fig. 3-7(a)). From the morphologies, we estimate the likely identities of the cells in Fig. 3-8(a) were adipocytes, the cells in Fig. 3-8(b) were undifferentiated ES cells, and the cells in Fig. 3-8(c) were neural progenitor cells. Based on the time-lapse cell imaging data, we can track the cell division event for each type of cell, as shown in Fig. 3-8(a), (b) and (c). The time increment between each image frame is about 0.5 hr. This experiment clearly demonstrates that the ePetri can collect microscopy resolution images over the entire area of the sensor, which is orders of magnitude larger than the field-of-view of a conventional microscope with comparable resolution.

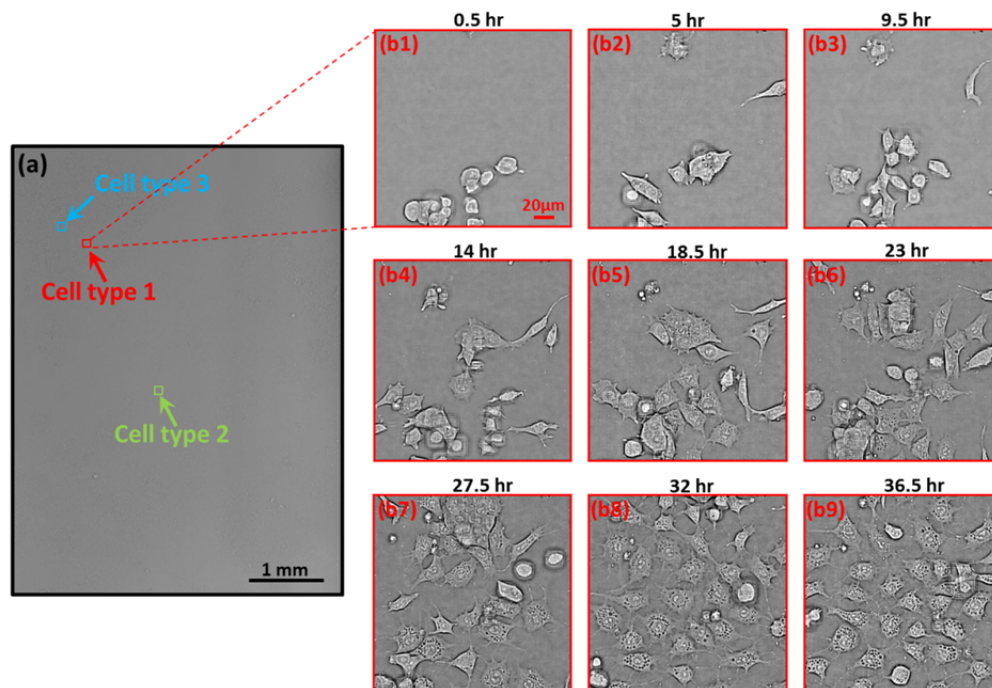


Figure 3-7 (color): Time-lapse imaging of embryonic stem cell culture on the ePetri platform. (a) Based on the morphologies, at least three types of cells were found in the reconstructed image, denoted by the red, green and blue arrows. (b1-b9) A specific sub-location for cell type 1 (adipocytes) acquired at different time. The observable differentiation for this cell type occurred at about 20 hours after the stem cell plating.

Thus we were able to visualize dynamically one of the striking characteristics of ES cells – their intrinsic heterogeneity. In addition to morphological heterogeneity, ES cells are known to exhibit wide variations in gene expression. Furthermore, individual cells often differentiate at different times and locations and choose different fates even when exposed to the same media conditions in the same Petri dish. Consequently, the ability to continually monitor ES cells over time across a very large area could provide qualitatively new insights into the behavior of these cells across a variety of protocols and experiments.

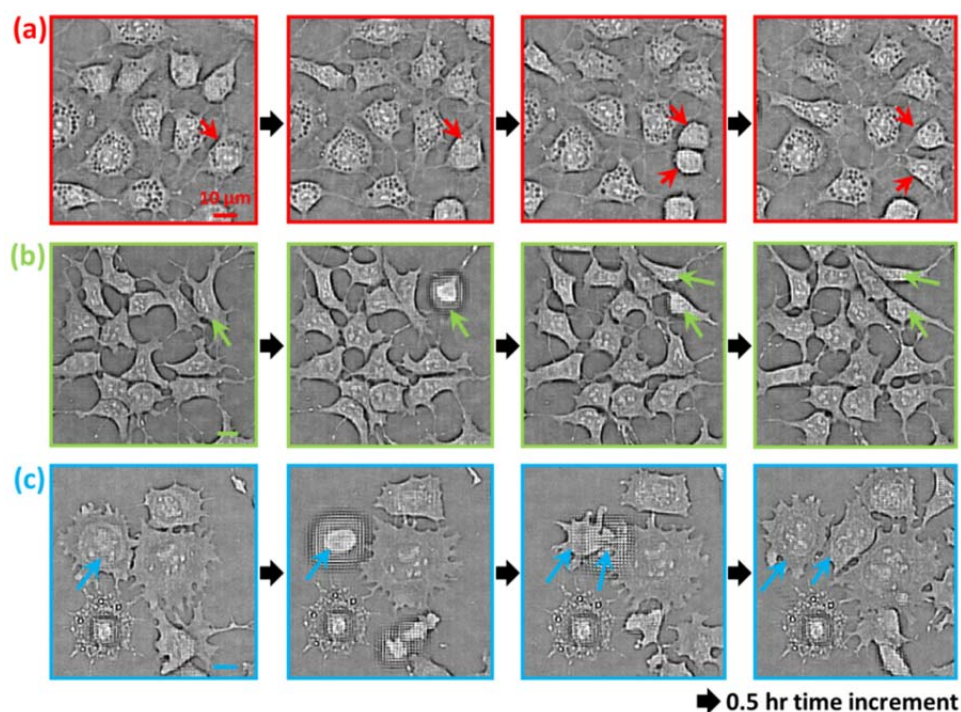


Figure 3-8 (color): Tracking of cell division (denoted by the arrows) for cell type 1 (a), type 2 (b), and type 3 (c). The defocus effect in some of the images is due to the cell detaching from the sensor surface when cell division occurs. The time increment between each image frame is about 0.5 hr. The location of these cell types are denoted at Fig. 3-7(a).

3.4 Resolution of the ePetri platform

The optical resolution of ePetri platform was investigated by imaging 500nm microspheres (Polysciences) that were directly placed on the image sensor surface. The imaging process was identical to the one previously described for HeLa cell culture. For a single 500nm microsphere, the bright center of the microsphere was clearly resolved (shown in Fig. 3-9(a)), with the full-width at half maximum (FWHM) of 690 nm. Since microscopy resolution is formally defined based on a given microscope's ability to resolve two closely spaced feature points, we further analyzed the case of two closely spaced microspheres to better establish our prototype's resolution. Fig. 3-9(a) also showed the reconstructed images of two closely packed 500 nm microspheres with center-to-center distance of 660

nm. The data trace clearly showed a valley between the two peaks and, thus, established that the resolution of our prototype was 660 nm or better. To further verify this point, Fig. 3-9(b) shows the magnified small feature of the stained HeLa cell sample and the FWHM of this feature was estimated to be 710 nm, which was in good agreement with the estimated resolution limit.

We do, hereby, note that the resolution of the SPSM will deteriorate if the target samples are placed at a substantial distance above the sensor surface. The exact resolution-to-height function is not trivially expressible and instead depends on the angular distribution function of the sample scattering, presence/absence and characteristics of pixel lens, characteristics of the pixel structure, sensor passivation layer thickness, and the physical dimensions of the light sensitive area on each sensor pixel [43, 44]. The last four parameters are proprietary information that are not publicly disclosed by the chip maker. We believe the method we just described provide an adequate resolution characterization recipe for readers interested in building their own ePetri, especially if a different sensor chip type is used.

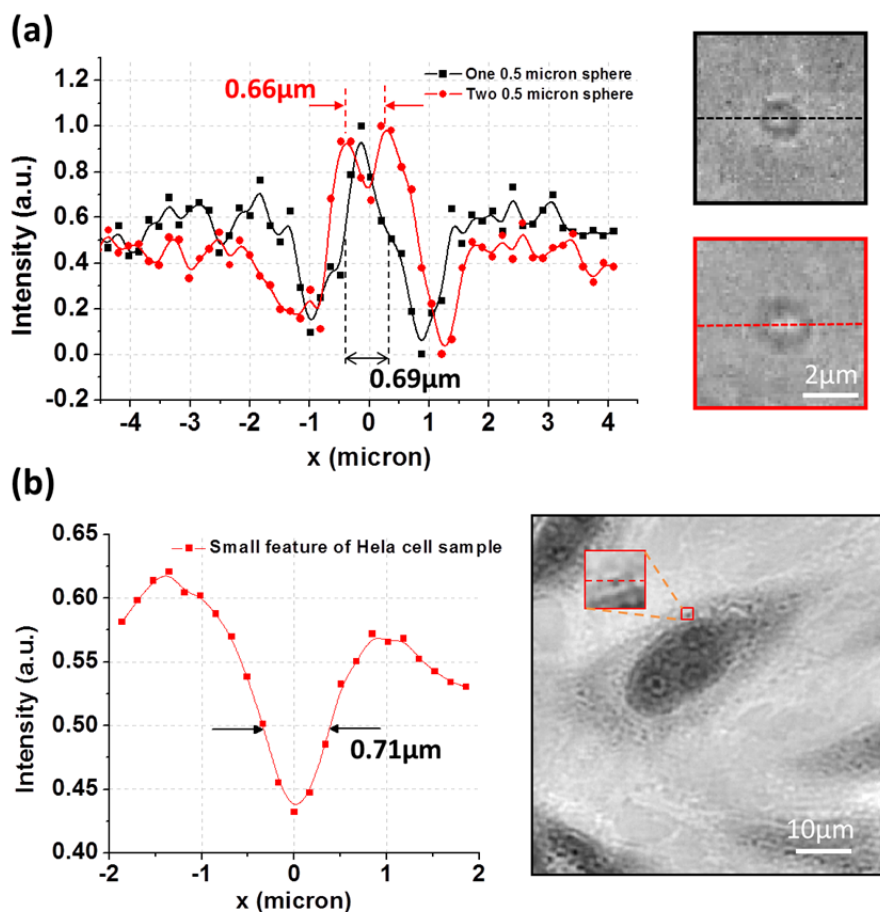


Figure 3-9 (color): Resolution of the proposed platform. (a) The line traces of images of one 500 nm microsphere (black line) and two 500 nm microspheres (red line). (b) The line traces of the small feature of reconstructed high resolution HeLa cell image.

3.5 Discussions

We have developed a new lensless microscopy imaging method, sub-pixel perspective sweeping microscopy (SPSM) that is able to image confluent cell culture with high resolution and incoherent light sources. The images are closely comparable with those obtained with a conventional microscope. Our prototype has a demonstrated resolution of 660 nm. This imaging method can be applied to implement a smart Petri dish, ePetri, which is capable of performing high resolution and autonomous imaging of cells plated on or growing on a low-cost CMOS sensor chip. Our preliminary cell culture experiment

indicates that the ePetri can be a useful tool for in-vitro long-term cell observations. To demonstrate that this imaging platform can be easily assembled, our prototype was constructed out of Lego blocks, a smartphone and an imaging sensor chip.

There are three aspects to the ePetri technology that are worth further investigations:

1) At present, our ePetri is incapable of performing fluorescence imaging. In principle, we can create a fluorescence-capable ePetri by simply coating the sensor chip with an appropriate filter material. However, the added thickness of the filter can significantly separate the cell culture from the sensor's light sensitive region and result in resolution deterioration. On the other hand, if the filter layer is too thin, we may not be able to sufficiently block the fluorescence excitation light field from the sensor. In the near future, we plan to examine several ePetri design permutations (for example, grid pattern scanning [45, 46]) that is able to circumvent this problem.

2) Our ePetri prototype sustained cell culture growth by immersing the cells in a nutrient filled fluid, rather than providing them with a solid growth substrate. A thick solid growth substrate would have compromised resolution in much the same way a thick filter would have. For experiments that absolutely require solid growth substrate, we encourage the user to experimentally seek an appropriate compromise that can sustain cell growth without deteriorating resolution beyond the user's requirements.

3) Our current ePetri can acquire a full set of data (~20 seconds) to render a high-resolution image in a time period of 2-3 minutes. We did not optimize our system for speed as our focus here is on tracking cell culture growth - a relatively slow process. Interested user can certainly optimize the system for speed by improving on all aspects of the system.

There are several advantages associated with this technology that are worth noting:

1) Low cost. The ePetri uses a CMOS imaging sensor as the base substrate for cell culture growth. Post-experiment, the sensor can either be disposed or washed-and-reused. Given the low cost of these sensor chips, they are unlikely to represent a major cost component in most cell culture experiments.

2) Disposable. In certain biohazardous experiments, the ability to treat the sensor chips as disposable units would significantly reduce any associated risks.

3) Direct readout from the incubator. As our demonstration experiment shows, the ePetri is sufficiently compact to fit comfortably in a typical incubator. In fact, given its footprint, it would be possible to fit multiple ePetri units into the same incubator. Upon connecting the ePetri to an exterior processor via an appropriate data cable, a user can start to collect images of the growing cell culture without removing the unit from the incubator. This advantage saves labor and cut down on the perturbations the cell culture is subjected to. It is also possible to design a compact and portable incubator ePetri combination that is suitable for point-of-care diagnostic and/or other uses.

4) Continuous from-the-incubator monitoring. On a related point, an ePetri user would be able to monitor cell growth continuously. In bioscience research, this represents a good means for performing longitudinal studies. In medical applications, this can significantly cut down on the diagnostic time for medical procedures that requires culture growth based assessment. As an example, the ePetri can replace the standard Petri dish for tuberculosis, staph and other bacterial infection diagnosis. Whereas standard medical practice would start initiate a bacteria culture growth and then check the growth at relatively long time intervals (checking frequently would be too time consuming), a modified ePetri may potentially be able to continuously and autonomously monitor for growth changes and notify the user to examine the sample when significant changes have been detected.

5) Platform technology. Finally, we note that the ePetri is a platform technology. Since the top surface of the sensor chip is unmodified, a user is free to build upon it. It is very possible to simply use the ePetri as an imaging platform for a large number of sophisticated lab-on-a-chip designs, such as microorganisms detection based on the use of closed dielectrophoretic cages [47], droplet-based platforms for cell encapsulation and screening [48], microfluidics-based phenotyping imaging and screening of multicellular organisms [49], and high throughput malaria infected erythrocyte separation and imaging [50] . It is also possible to modify the ePetri to serve as a self-contained incubator and imaging unit.

Bibliography

- [1] G. Zheng, S. A. Lee, Y. Antebi *et al.*, “The ePetri dish, an on-chip cell imaging platform based on subpixel perspective sweeping microscopy (SPSM),” *Proceedings of the National Academy of Sciences*, vol. 108, no. 41, pp. 16889-16894, 2011.
- [2] X. Heng, D. Erickson, L. Baugh *et al.*, “Optofluidic microscopy ---- method for implementing a high resolution optical microscope on a chip,” *Lab on a Chip*, vol. 6, no. 10, pp. 1274-1276, 2006.
- [3] X. Cui, L. Lee, X. Heng *et al.*, “Lensless high-resolution on-chip optofluidic microscopes for *Caenorhabditis elegans* and cell imaging,” *Proceedings of the National Academy of Sciences*, vol. 105, no. 31, pp. 10670, 2008.
- [4] G. Zheng, S. A. Lee, S. Yang *et al.*, “Sub-pixel resolving optofluidic microscope for on-chip cell imaging,” *Lab on a Chip*, vol. 10, no. 22, pp. 3125-3129, 2010.
- [5] L. Repetto, E. Piano, and C. Pontiggia, “Lensless digital holographic microscope with light-emitting diode illumination,” *Optics letters*, vol. 29, no. 10, pp. 1132-1134, 2004.
- [6] O. Mudanyali, D. Tseng, C. Oh *et al.*, “Compact, light-weight and cost-effective microscope based on lensless incoherent holography for telemedicine applications,” *Lab on a Chip*, vol. 10, no. 11, pp. 1417, 2010.
- [7] W. Xu, M. Jericho, I. Meinertzhagen *et al.*, “Digital in-line holography for biological applications,” *Proceedings of the National Academy of Sciences of the United States of America*, vol. 98, no. 20, pp. 11301, 2001.
- [8] J. Garcia-Sucerquia, W. Xu, S. K. Jericho *et al.*, “Digital in-line holographic microscopy,” *Applied optics*, vol. 45, no. 5, pp. 836-850, 2006.
- [9] M. Malek, D. Allano, S. Coëtmelec *et al.*, “Digital in-line holography: influence of the shadow density on particle field extraction,” *Optics Express*, vol. 12, no. 10, pp. 2270-2279, 2004.
- [10] D. Gabor, “A new microscopic principle,” *Nature*, vol. 161, no. 4098, pp. 777-778, 1948.
- [11] S. O. Isikman, W. Bishara, S. Mavandadi *et al.*, “Lens-free optical tomographic microscope with a large imaging volume on a chip,” *Proceedings of the National Academy of Sciences*, vol. 108, no. 18, pp. 7296, 2011.
- [12] G. Liu, and P. Scott, “Phase retrieval and twin-image elimination for in-line Fresnel holograms,” *J. Opt. Soc. Am. A*, vol. 4, no. 1, pp. 159, 1987.
- [13] J. R. Fienup, “Reconstruction of an object from the modulus of its Fourier transform,” *Optics letters*, vol. 3, no. 1, pp. 27-29, 1978.
- [14] G. Koren, F. Polack, and D. Joyeux, “Iterative algorithms for twin-image elimination in in-line holography using finite-support constraints,” *JOSA A*, vol. 10, no. 3, pp. 423-433, 1993.
- [15] S. Lai, B. King, and M. A. Neifeld, “Wave front reconstruction by means of phase-shifting digital in-line holography,” *Optics Communications*, vol. 173, no. 1-6, pp. 155-160, 2000.
- [16] J. Rodenburg, A. Hurst, and A. Cullis, “Transmission microscopy without lenses for objects of unlimited size,” *Ultramicroscopy*, vol. 107, no. 2-3, pp. 227-231, 2007.

- [17] J. R. Fienup, "Reconstruction of a complex-valued object from the modulus of its Fourier transform using a support constraint," *J. Opt. Soc. Am. A*, vol. 4, no. 1, pp. 118-123, 1987.
- [18] G. Biener, A. Greenbaum, S. O. Isikman *et al.*, "Combined reflection and transmission microscope for telemedicine applications in field settings," *Lab on a Chip*, 2011.
- [19] L. Denis, D. Lorenz, E. Thiébaud *et al.*, "Inline hologram reconstruction with sparsity constraints," *Optics letters*, vol. 34, no. 22, pp. 3475-3477, 2009.
- [20] F. Zhang, G. Pedrini, and W. Osten, "Phase retrieval of arbitrary complex-valued fields through aperture-plane modulation," *Physical Review A*, vol. 75, no. 4, pp. 043805, 2007.
- [21] L. Xu, J. Miao, and A. Asundi, "Properties of digital holography based on in-line configuration," *Optical Engineering*, vol. 39, no. 12, pp. 3214-3219, 2000.
- [22] V. Micó, J. García, Z. Zalevsky *et al.*, "Phase-Shifting Gabor Holographic Microscopy," *Journal of Display Technology*, vol. 6, no. 10, pp. 484-489, 2010.
- [23] C. S. Guo, L. L. Lu, G. X. Wei *et al.*, "Diffractive imaging based on a multipinhole plate," *Optics letters*, vol. 34, no. 12, pp. 1813-1815, 2009.
- [24] T. Schroeder, "Long-term single-cell imaging of mammalian stem cells," *Nature Methods*, vol. 8, no. 4s, pp. S30-S35, 2011.
- [25] A. R. Cohen, F. L. A. F. Gomes, B. Roysam *et al.*, "Computational prediction of neural progenitor cell fates," *Nat Meth*, vol. 7, no. 3, pp. 213-218, 2010.
- [26] H. M. Eilken, S. I. Nishikawa, and T. Schroeder, "Continuous single-cell imaging of blood generation from haemogenic endothelium," *Nature*, vol. 457, no. 7231, pp. 896-900, 2009.
- [27] M. R. Costa, F. Ortega, M. S. Brill *et al.*, "Continuous live imaging of adult neural stem cell division and lineage progression in vitro," *Development*, vol. 138, no. 6, pp. 1057, 2011.
- [28] B. Dykstra, J. Ramunas, D. Kent *et al.*, "High-resolution video monitoring of hematopoietic stem cells cultured in single-cell arrays identifies new features of self-renewal," *Proceedings of the National Academy of Sciences*, vol. 103, no. 21, pp. 8185-8190, May 23, 2006, 2006.
- [29] G. Repetto, A. del Peso, and J. L. Zurita, "Neutral red uptake assay for the estimation of cell viability/cytotoxicity," *Nature Protocols*, vol. 3, no. 7, pp. 1125-1131, 2008.
- [30] T. E. Angelini, E. Hannezo, X. Trepas *et al.*, "Glass-like dynamics of collective cell migration," *Proceedings of the National Academy of Sciences*, vol. 108, no. 12, pp. 4714, 2011.
- [31] E. Borenfreund, and J. A. Puerner, "Toxicity determined in vitro by morphological alterations and neutral red absorption," *Toxicology Letters*, vol. 24, no. 2-3, pp. 119-124, 1985.
- [32] P. F. Cavanaugh, P. S. Moskwa, W. H. Donish *et al.*, "A semi-automated neutral red based chemosensitivity assay for drug screening," *Investigational new drugs*, vol. 8, no. 4, pp. 347-354, 1990.
- [33] L. I. Zon, and R. T. Peterson, "In vivo drug discovery in the zebrafish," *Nat Rev Drug Discov*, vol. 4, no. 1, pp. 35-44, 2005.
- [34] D. Lange, C. W. Stormont, C. A. Conley *et al.*, "A microfluidic shadow imaging system for the study of the nematode *Caenorhabditis elegans* in space," *Sensors and Actuators B: Chemical*, vol. 107, no. 2, pp. 904-914, 2005.

- [35] L. Wei, T. Knoll, and H. Thielecke, "On-chip integrated lensless microscopy module for optical monitoring of adherent growing mammalian cells," *Engineering in Medicine and Biology Society (EMBC), 2010 Annual International Conference of the IEEE*, pp. 1012-1015, Aug. 31, 2010-Sept. 4, 2010.
- [36] P. Milanfar, *Super-Resolution Imaging*. CRC Press, 2010.
- [37] R. Hardie, K. Barnard, and E. Armstrong, "Joint MAP registration and high-resolution image estimation using a sequence of undersampled images," *IEEE Transactions on Image Processing*, vol. 6, no. 12, pp. 1621-1633, 1997.
- [38] M. Elad, and Y. Hel-Or, "A fast super-resolution reconstruction algorithm for pure translational motion and common space-invariant blur," *IEEE Transactions on Image Processing*, vol. 10, no. 8, pp. 1187-1193, 2001.
- [39] S. Farsiu, M. Robinson, M. Elad *et al.*, "Fast and robust multiframe super resolution," *IEEE Transactions on Image Processing*, vol. 13, no. 10, pp. 1327-1344, 2004.
- [40] S. Farsiu, D. Robinson, M. Elad *et al.*, "Advances and challenges in super resolution," *International Journal of Imaging Systems and Technology*, vol. 14, no. 2, pp. 47-57, 2004.
- [41] S. Farsiu, M. Elad, and P. Milanfar, "Multiframe demosaicing and super-resolution of color images," *IEEE Transactions on Image Processing*, vol. 15, no. 1, pp. 141-159, 2006.
- [42] "<http://users.soe.ucsc.edu/~milanfar/software/superresolution.html>."
- [43] X. Heng, X. Cui, D. Knapp *et al.*, "Characterization of light collection through a subwavelength aperture from a point source," *Optics express*, vol. 14, no. 22, pp. 10410-10425, 2006.
- [44] Y. M. Wang, G. Zheng, and C. Yang, "Characterization of acceptance angles of small circular apertures," *Optics Express*, vol. 17, no. 26, pp. 23903-23913, 2009.
- [45] J. Wu, X. Cui, G. Zheng *et al.*, "Wide field-of-view microscope based on holographic focus grid illumination," *Optics letters*, vol. 35, no. 13, pp. 2188-2190, 2010.
- [46] J. Wu, G. Zheng, Z. Li *et al.*, "Focal plane tuning in wide-field-of-view microscope with Talbot pattern illumination," *Optics letters*, vol. 36, no. 12, pp. 2179-2181, 2011.
- [47] G. Medoro, N. Manaresi, A. Leonardi *et al.*, "A lab-on-a-chip for cell detection and manipulation," *Sensors Journal, IEEE*, vol. 3, no. 3, pp. 317-325, 2003.
- [48] J. Clausell-Tormos, D. Lieber, J.-C. Baret *et al.*, "Droplet-Based Microfluidic Platforms for the Encapsulation and Screening of Mammalian Cells and Multicellular Organisms," *Chemistry & biology*, vol. 15, no. 5, pp. 427-437, 2008.
- [49] M. M. Crane, K. Chung, J. Stirman *et al.*, "Microfluidics-enabled phenotyping, imaging, and screening of multicellular organisms," *Lab on a Chip*, vol. 10, no. 12, pp. 1509-1517, 2010.
- [50] H. W. Hou, A. A. S. Bhagat, A. G. Lin Chong *et al.*, "Deformability based cell margination-A simple microfluidic design for malaria-infected erythrocyte separation," *Lab on a Chip*, vol. 10, no. 19, pp. 2605-2613, 2010.

Chapter 4

Digital 3D refocusing using a LED matrix

The active control of the illumination light source can also be combined with tomography reconstruction technique for 3D imaging. In this chapter, we present the implementation of digital 3D refocusing approach using a simple LED matrix [1]. Images of a starfish embryo were acquired by using such an approach for demonstration.

4.1 Background

Appropriate illumination of the specimen is an important factor in achieving high resolution and high quality images in microscopy and critical photomicrography. Most modern laboratory microscopes are equipped with the Köhler illumination setup, which was first introduced in 1893 by August Köhler, and is now recommended by most microscope manufacturers. Such a Köhler illumination setup is composed of collector lens, field diaphragm, condenser diaphragm and condenser lens. It can provide specimen illumination that is uniformly bright and free from glare [2]. More advanced illumination schemes have also been reported in recent years, including structured illumination [3, 4], light sheet illumination [5], focus-grid illumination [6] and non-diffracted Bessel beam illumination [7].

With the maturation of LED technology, the use of LEDs as the light source for optical microscopy can bring certain cost- and usage- advantages [4, 8, 9]. In this chapter, we demonstrate a simple and cost-effective microscopy illumination scheme by replacing the optical condenser with a programmable LED array. The proposed illumination scheme has several advantages. 1) A conventional bright field image can be acquired by digitally matching the illumination numerical aperture (NA) to the collection NA (i.e. NA of objective lens). 2) A dark field image of the specimen can be acquired by simply turning on the LEDs at the edge of the array, where the illumination NA is beyond the collection NA.

3) We can sequentially turn on each individual LED and capture a sequence of specimen images. These images contain the information for different view angles, and therefore we can post-process them to digitally refocus the specimen into different depths. 4) The aforementioned imaging schemes can be accomplished simultaneously by a single LED scan process. We can select the images corresponding to LEDs within the collection NA to form a bright field image. On the other hand, the images corresponding to LEDs beyond the collection NA can be used for dark field imaging. Furthermore, we can re-align all the images (with different view angles) to digitally refocus the specimen into different depths. 5) No mechanical moving parts are involved in the proposed scheme. The scanning rate of the LEDs can easily operate in the kHz domain. The limiting factor in our prototype is the capturing frame rate / data transfer rate of the camera. Due to the rapid development of the semiconductor industry, we believe that such a data transfer rate will not be a significant bottleneck for the proposed illumination scheme in the near future. 6) The proposed scheme is cost-effective and compatible with most modern laboratory microscopes.

4.2 Principle and experimental setup

The proposed illumination scheme is shown in Fig. 4-1(a), where the optical condenser is replaced by an LED array. To understand the principle, we first consider only one LED lit in the LED array. The location of this LED can be denoted as (x_i, y_i) , as shown in Fig. 4-1(b). Assuming the distance (at the z direction) between the LED array and specimen is 'H', the illumination NA of this LED can be defined as

$$\frac{r}{\sqrt{r^2+H^2}} \quad (4-1)$$

, where $r = \sqrt{(x_i - x_c)^2 + (y_i - y_c)^2}$ and (x_c, y_c) is the location of the center of the LED matrix. For microscopy bright-field imaging, the illumination NA is matched to the collection NA of the objective lens. Such a matching procedure can be performed by adjusting the size of the condenser diaphragm in the Köhler illumination setup. In the proposed scheme in Fig. 4-1(a), we can calculate the illumination NA for each individual LED by using Eq. (4-1). We can then separate them into two groups using the following criteria. Group 1: illumination NA > collection NA; group 2: illumination NA < collection

NA. To achieve the bright field illumination condition, we simply turn off the group 1 LEDs and turn on the group 2 LEDs. Fig. 4-1(c) shows an example of NA matching by using the proposed scheme for the bright field imaging (the LEDs at the edge, whose illumination NA is larger than the collection NA, are turned off).

Another important microscopy method is dark field microscopy. Darkfield microscopy can be used to enhance the contrast in unstained samples [10, 11]. It works by illuminating the sample with light that will not be collected by the objective lens, and thus, it will not form part of the image. In a conventional microscopy setup, a light stop is placed at the condenser to create a dark field illumination cone. For the proposed scheme, we can simply turn on the LEDs in group 1 to collect the scattering light component from the specimen and turn off the LEDs in group 2 to reject the direct light illumination. Such an illumination scheme is illustrated in Fig. 4-1(d), where we need only turn on the LEDs whose illumination NA is larger the collection NA.

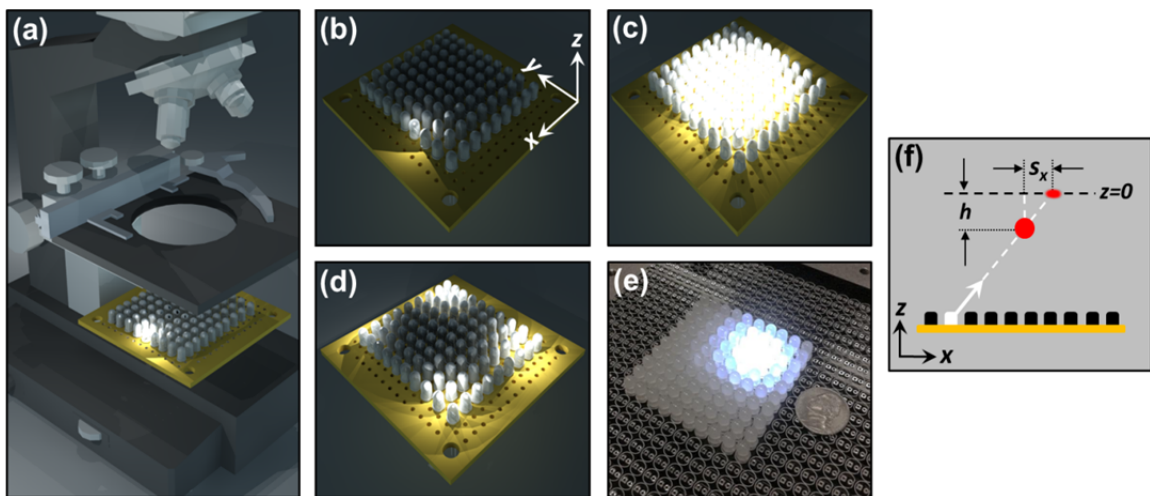


Figure 4-1 (color): The proposed illumination scheme. (a) The optical condenser is replaced by a programmable LED array. No lens is placed between the LED array and the sample stage. (b) One LED is turned on for illumination. (c) The LEDs in central part are turned on for the bright field imaging. (d) The LEDs at the edge are turned on for dark field imaging. (e) The actual LED array prototype used in our experiment. (f) A simple ray-trace diagram showing different z -planes result in different image shifts (also see Eq. (4-2)).

As we can see from Fig. 4-1(a), each individual LED illuminated the specimen at a specific incident angle. Therefore, each frame of the captured image provided a unique perspective view of the specimen. Conceptually, the idea is similar to tilted-view microscopy [12], where the sample is mechanically tilted to provide different view angles. Based on Fourier slice theorem, each image provides us information on one slice of 3D Fourier space. Therefore, based on the captured images with different LEDs, we can reconstruct the specimen at different depths. The process is equivalent to tomography reconstruction. The data processing procedures can be described in the following steps. 1) Select the images from group 2 LEDs. 2) For different LEDs in group 2, the incident angles are different, and thus the shifts of the specimen at different depths are also different. This second step is to calculate image shifts in x and y directions (denoted as ' S_x, S_y ') for different depths (denoted as ' h ') based on the following equation:

$$S_x(h) = x_i h/H, S_y(h) = y_i h/H \quad (2)$$

, where (x_i, y_i) is location of the LED and ' H ' is the distance between the LED array and specimen (Fig. 4-1(f)). 3) Each captured image is normalized by its maximum intensity (i.e. the maximum pixel value of the image). 4) The normalized images are back shifted by the amount of (s_x, s_y) and merged to one image [13]. 5) (Optional) the merged image can be further deblurred with the point spread function (PSF) of the objective lens at that certain depth ' h '. The PSF can be estimated from the Airy pattern.

4.3 Demonstration in biological imaging

To demonstrate the capabilities of the proposed approach, we used an Olympus BX41 microscope with a 10X (0.3 NA) objective lens as our demonstration imaging setup. We replaced the condenser with a programmable LED array as shown in Fig. 4-1(e). This LED array contained 10*10 phosphor-based diffused white LEDs (Betlux BL-L513UWC, with 160 degree wide illumination angles), which were mounted on a PCB board (the PCB board can support up to 25*25 LEDs). The measured distance (at z direction) between the sample stage and the LED array (i.e., ' H ') was 80 mm. The size of this 10*10 LED array was 54 mm (i.e., the distance between adjacent LEDs is 6 mm). This 10*10 array was

driven in a traditional row/column format using a Macroblock constant-current LED driver (MBI5027) and a demultiplexed transistor-switched column select. An Atmel ATMEGA-328 microcontroller provided the logical control on the lines. To achieve maximum brightness, the array was driven statically rather than in normal scanning mode, eliminating the duty cycle and boosting current through the LEDs to 125 mA (the measured light intensity is ~ 0.9 W/m²) with 100 ohms on the MBI5027 resistive input for current control.

We next used the proposed system for bright field and dark field imaging demonstrations (Fig. 4-2). We used a microscope slide of starfish embryo (Carolina Biological Supply) as the specimen. The experimental procedures can be described as follows: 1) turn on the individual LEDs one by one; 2) capture the corresponding images (total 100 frames are captured for 10*10 LEDs); 3) sum the images from the group 2 LEDs to create the bright field image, as shown in Fig. 4-2(a); 4) sum the images from the group 1 LEDs to create the darkfield image, as shown in Fig. 4-2(b). The entire image capturing process required 2 seconds. The scanning rate of LEDs can reach the kHz regime, and the limiting factor in our prototype was the data transfer rate of the CMOS image sensor (Aptina MT9M001; we captured images at 50 fps).

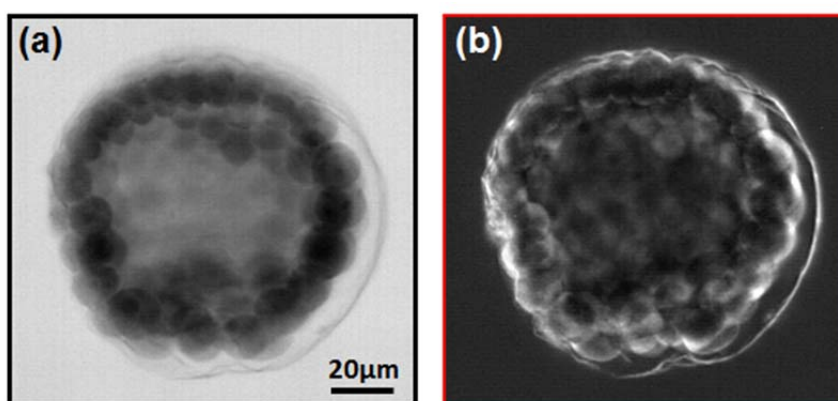


Figure 4-2 (color): Demonstration of bright-field and dark-field imaging. The bright field (a) and dark field (b) images of a starfish embryo captured using the proposed illumination scheme.

Next, we demonstrate the most important feature of the proposed scheme: digital refocusing. In the previous experiment shown in Fig. 4-2, we captured 100 frames (one for each individual LED) and then regrouped them to form a bright field/dark field image. In fact, this 100-frame data set contained useful information on the 3D structure of the specimen and it can be used to digitally refocus the specimen into different depths.

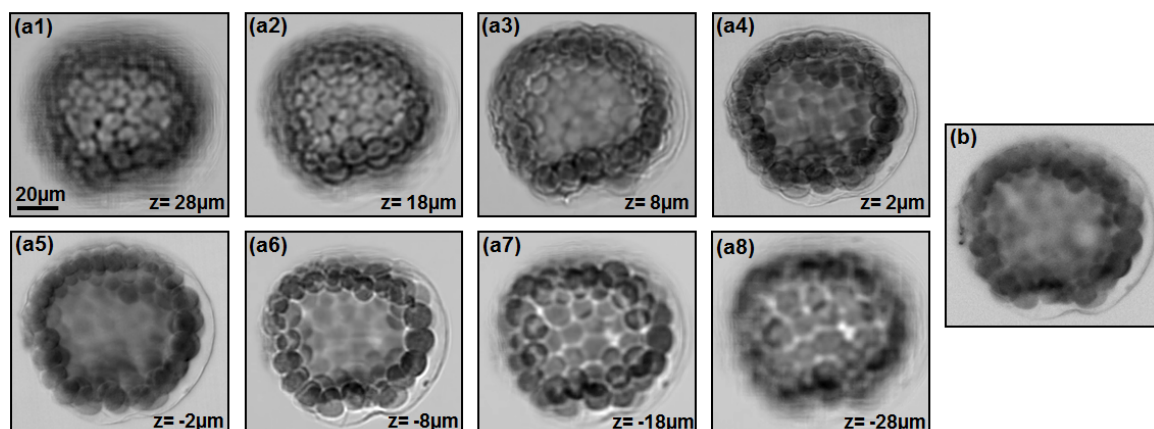


Figure 4-3: Demonstration of digital 3D refocusing. (a1-a8) Based on the captured images for different individual LEDs, we can digitally refocus the starfish embryo into different depths. No mechanical scanning is involved in this process. (b) The image taken by the conventional Köhler illumination. We use a halogen lamp as the light source with an illumination NA of 0.3 (matching to 0.3 NA objective lens).

The result of digital refocusing following the above procedure is shown in Fig. 4-3(a1)-(a8). Fig. 4-3(b) is image taken by the conventional Köhler illumination. From this figure, we can see the cell development of the starfish embryo at different sections. We note that the sectioning ability of our approach is determined by the objective lens. For a conventional microscopy setup with a plane wave illumination, the captured image is a superposition of images from different depth sections through the entire depth of field. By using the proposed illumination scheme, we can separate all these different sections from the captured images. Most importantly, we can accomplish this without mechanically moving the sample or changing the setup. The image processing time was less than 0.2 second by using a personal computer with an Intel i7 CPU.

4.4 Discussion

A special case of Eq. (4-2) is ' $h = 0$ ', i.e. the image in focus. In this case, the reconstructed image is equivalent to the image taken by the conventional Köhler illumination approach. Fig. 4-4 shows such a comparison. The slight difference in image contrast can be attributed to the difference of the light-emitting spectra of the two approaches (the point spread function of objective lens is different for different wavelengths).

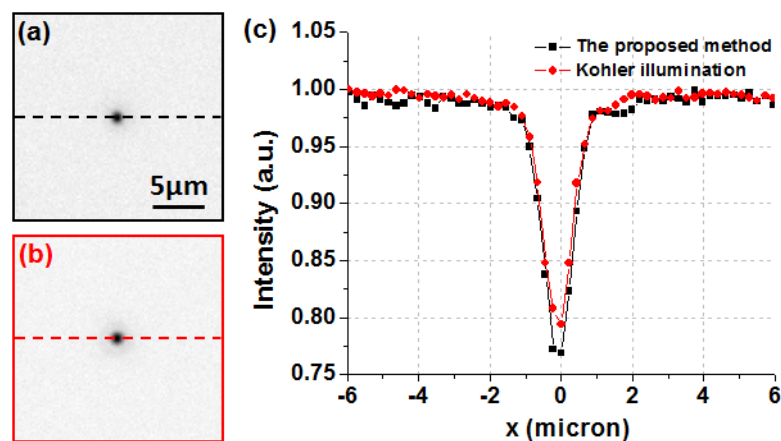


Figure 4-4 (color): Comparison between the proposed method and Köhler illumination. The images of a 0.5 μm bead by using (a) the proposed method (b) Köhler illumination. (c) The line traces of (a) and (b).

To summarize, a simple microscopy illumination scheme based on a cost-effective programmable LED array is proposed in this letter. A sequence of images is captured, one for each individual LED. Each image provides a unique view angle of the specimen. We showed that these images can be post-processed to render a bright field image, dark field image, and more importantly, sectioned images at different depths. The ability to digitally refocus the specimen into different depths without mechanically scanning the sample is useful for quantitative phase imaging [14], 3D position sensing and metrology. We note that the proposed illumination scheme is not a simple tradeoff between time and imaging functionalities. A relatively long capturing time (2 seconds) allows us to acquire multiple frames, and thus the signal to noise ratio of the final result is also higher than in a single

frame (Note that the bit depth of the image sensor is limited). This is similar to averaging frames to reduce noise in the conventional still microscope. We also note that the illumination angle of the diffuse LEDs we used spanned a range of 160 degrees, therefore the maximum illumination NA was close to one. To further enhance the light collecting efficiency, we can place the LED array at the back focal plane of the condenser (the rest of microscope setup would remain unchanged).

Bibliography

- [1] G. Zheng, C. Kolner, and C. Yang, "Microscopy refocusing and dark-field imaging by using a simple LED array," *Optics letters*, vol. 36, no. 20, pp. 3987-3989, 2011.
- [2] J. James, *Light microscopic techniques in biology and medicine*. Springer, 1976.
- [3] M. G. L. Gustafsson, "Nonlinear structured-illumination microscopy: wide-field fluorescence imaging with theoretically unlimited resolution," *Proceedings of the National Academy of Sciences of the United States of America*, vol. 102, no. 37, pp. 13081, 2005.
- [4] V. Poher, H. Zhang, G. Kennedy *et al.*, "Optical sectioning microscopes with no moving parts using a micro-stripe array light emitting diode," *Optics Express*, vol. 15, no. 18, pp. 11196-11206, 2007.
- [5] J. Huisken, J. Swoger, F. Del Bene *et al.*, "Optical sectioning deep inside live embryos by selective plane illumination microscopy," *Science*, vol. 305, no. 5686, pp. 1007, 2004.
- [6] J. Wu, G. Zheng, Z. Li *et al.*, "Focal plane tuning in wide-field-of-view microscope with Talbot pattern illumination," *Optics letters*, vol. 36, no. 12, pp. 2179-2181, 2011.
- [7] F. O. Fahrbach, P. Simon, and A. Rohrbach, "Microscopy with self-reconstructing beams," *Nature photonics*, 2010.
- [8] V. Bormuth, J. Howard, and E. SCHÄFFER, "LED illumination for video enhanced DIC imaging of single microtubules," *Journal of microscopy*, vol. 226, no. 1, pp. 1-5, 2007.
- [9] V. Murthy, T. F. Sato, D. F. Albeanu *et al.*, "LED Arrays as Cost Effective and Efficient Light Sources for Widefield Microscopy," *PLoS ONE*, vol. 3, no. 5, 2008.
- [10] G. C. Cox, *Optical imaging techniques in cell biology*, Boca Raton :: CRC/Taylor & Francis, 2007.
- [11] G. Zheng, X. Cui, and C. Yang, "Surface-wave-enabled darkfield aperture for background suppression during weak signal detection," *Proceedings of the National Academy of Sciences*, vol. 107, no. 20, pp. 9043, 2010.
- [12] P. J. Shaw, D. A. Agard, Y. Hiraoka *et al.*, "Tilted view reconstruction in optical microscopy. Three-dimensional reconstruction of *Drosophila melanogaster* embryo nuclei," *Biophysical journal*, vol. 55, no. 1, pp. 101-110, 1989.
- [13] G. Zheng, S. A. Lee, S. Yang *et al.*, "Sub-pixel resolving optofluidic microscope for on-chip cell imaging," *Lab Chip*, 2010.
- [14] A. Barty, K. Nugent, D. Paganin *et al.*, "Quantitative optical phase microscopy," *Optics letters*, vol. 23, no. 11, pp. 817-819, 1998.

Chapter 5

Sub-pixel resolving optofluidic microscope

The second strategy in design considerations is to manipulate the sample. In this chapter, we present a fully on-chip, lensless microscope device, termed sub-pixel resolving optofluidic microscope (SROFM) [1]. This device utilizes microfluidic flow to deliver specimens directly across an image sensor to generate a sequence of low-resolution projection images, where resolution is limited by the sensor's pixel size. This image sequence is then processed to reconstruct a single high resolution image, where features beyond the Nyquist rate of the LR images are resolved. We demonstrate the device's capabilities by imaging microspheres, *protist Euglena gracilis*, and *Entamoeba invadens* cysts with sub-cellular resolution.

5.1 Background

There is a growing interest in miniaturized microscopy systems [2-12]. Compact, inexpensive and portable imaging systems can fulfill many needs in biological research, point-of-care analysis and field diagnostics. For example, an on-chip microscope, produced at scale at existing semiconductor foundries and capable of imaging blood cell or parasite morphology in high resolution, would bring affordable healthcare diagnostics to less developed populations in rural settings, where it is too costly to deploy expensive conventional microscopes and skilled technicians.

In recent years, two classes of on-chip microscopy methods have been extensively reported to address these needs. The first method, optofluidic microscopy (OFM) [2], scans target objects across an aperture array using a microfluidic flow. The second method, inline holography [3], computationally renders images of target objects from interferometry measurements of the objects' scattered light field. Both methods achieve resolutions better than the sensor pixel size, but each has its respective strengths and tradeoffs. The inline

holography approach works well with samples prepared on glass slides and represents a good direct alternative to conventional microscopy. The OFM approach works directly with fluid samples and has the potential for integration with streamlined and high throughput microfluidic systems. The OFM achieves its highest sharpness at the floor of the microfluidic channel and its resolution is limited by the aperture size [4, 13]. The resolution degrades as a function of sample-to-floor separation [4]. Inline holography's resolution is directly related to the SNR of the capture image and sensor pixel size.

Recently, Bishara *et al.* combined inline holography with a multiframe pixel super-resolution approach to effectively shrink their image pixel size and thereby attain higher resolution images [14]. Multiframe pixel super-resolution approaches rely on combining information from multiple sub-pixel-shifted low resolution (LR) images to create a single high resolution (HR) image. Effectively, pixel super-resolution approaches take advantage of over-sampling in the time domain (capturing a sequences of images rather than a single image) to compensate for under-sampling in the spatial domain, for which the resolution is limited by the image sensor pixel size. To capture such a sequence of shifted LR images, either a fixed image sensor could image a spatially translating object, or a translating image sensor could image a fixed object. In either case, the success of the applied pixel super-resolution algorithm for HR image restoration depends critically on the precise control over and knowledge of the relative sub-pixel shifts between subsequent LR images. In the inline holography experiment reported in Ref. 13, a mechanical stage was employed 10cm above the sample to generate these sub-pixel shifts by precisely translating an optical fiber coupled with a light source.

Interestingly, not only is this multiframe pixel super-resolution approach adaptable for use in OFM as well, but it also greatly simplifies the microscopy scheme. More specifically, the microfluidic flow of the samples across the sensor suffices for generating sub-pixel shifts and precludes the need for an additional precision scanning setup. Furthermore, the resolution enhancement provided by the aperture arrays employed in current OFM system can be replaced by the enhancement provided by applying the pixel super-resolution algorithm. Without the aperture arrays, the OFM would be an even

simpler on-chip microscopy design, consists solely of a microfluidic channel emplaced upon a commercial 2D sensor chip.

In this chapter, we report on the implementation of a sub-pixel resolving optofluidic microscope (SROFM) based on this concept of applying pixel super-resolution algorithms in a new and simplified OFM scheme. We first give an overview of the entire imaging scheme, and then define in detail some of the more critical hardware design requirements and image processing techniques used, including methods for sub-pixel-shift estimation and a shift-and-add pixel super-resolution algorithm. We then present SROFM images of microspheres, *protist Euglena gracilis*, and *Entamoeba invadens* cysts and characterize the resolution limit of SROFM. Next, we discuss some of the advantages of SROFM, including the ability to image various different three-dimensional projections of rotating samples, and demonstrate our results in reconstructing high resolution video, where the time-varying interaction between the sample and the microfluidic flow is shown. Finally, we conclude with a discussion on possible biomedical and bioscience applications for SROFM.

5.2 The SROFM device

5.2.1 Principle of SROFM

The SROFM technique involves flowing a sample within a microfluidic channel directly above the surface of a CMOS image sensor (Fig. 5-1(a)). A sequence of pixel-size-limited low resolution (LR) direct-projection images of the sample, in which the sample within subsequent LR images is shifted by a sub-pixel amount, is captured and processed using a pixel super-resolution algorithm to produce a single high resolution (HR) image. The microscopy scheme is based on the OFM technique described earlier, except that it does not require a metal layer or an aperture array.

The SROFM hardware is compact, measuring approximately 1.5 cm x 1.5 cm in size (Fig. 5-1(b)), and consists of a polydimethyl-siloxane (PDMS) microfluidic channel (Fig. 5-1(c)) of width between 50 μm and 300 μm and height between 15 μm and 27 μm , with an inlet and outlet hole, bonded directly to an inexpensive, commercially available CMOS image sensor (Aptina MT9T001), with 3.2 μm pixel size. We designed the channel

height to be just slightly larger than the dimensions of the samples being imaged and removed the color filter and microlens layer on the sensor surface to ensure the samples flowed as close as possible to the sensor's active sensing layer. The microfluidic channel was attached to the CMOS sensor at an angle between 10 to 30 degrees with respect to the x direction of the CMOS pixel grid to ensure that the captured LR image sequence contained the necessary sub-pixel translations in both the x and y directions. Our choice of angle struck a balance between using a smaller angle with an imaging-area-of-interest with fewer pixel rows (and hence higher frame rate) and using a larger angle to obtain sufficient displacement along the y-direction with fewer frames. Our experiments were conducted under light intensity of 1.2 W/m^2 (comparable to room light) provided by a conventional LED lamp and we employed a single frame exposure time of 0.3 ms.

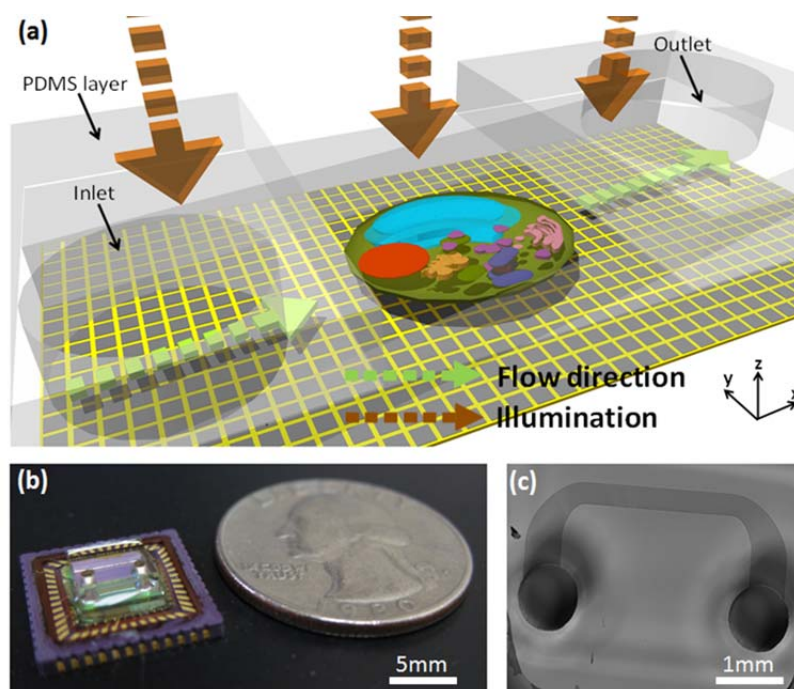


Figure 5-1 (color): Schematic of the SROFM device. (a) A sample, depicted as a cell in the figure, is flown in a microfluidic channel on top of an image sensor and the LR projection images are recorded. (b) Photograph of an actual sub-pixel resolving optofluidic microscope (SROFM) device. (c) Image of the microfluidic channel directly captured by the SROFM image sensor.

5.2.2 Fabrication of SROFM device

The device is comprised of two parts; a CMOS image sensor and a PDMS microfluidic channel. We used MT9T031C12STC (3.2 μm pixel, Aptina) for the image sensors. We removed the color filter and the microlens layer by treating the sensor under oxygen plasma for 10 min (80 W).

The PDMS channel is fabricated by conventional soft lithography; SU-8 (SU-8 2002, 2007, 2015, Microchem) mold is fabricated on a 3-inch silicon wafer by mask photolithography. The mold is then casted by poly-dimethylsiloxane (Sylgard, Dow-Corning) of 1:10 mix with base and curing agent, baked at 80°C for 1 hour. The fluidic channel is peeled, punched, and cut. The surfaces of the fluidic channel and the sensor are cleaned with ethanol and oxygen plasma, and then bonded to each other.

Polyethylene glycol (PEG, Sigma-Aldrich) surface treatment is used to render the channel surface hydrophilic and to reduce cell adhesion [15]. PEG solution is injected into the channel and the device is left under UV [4] lamp for 30 min. Then, the channel is flushed with DI water and dried.

5.3 On-chip imaging using the SROFM device

5.3.1 Imaging of non-rotating sample

For imaging, a liquid containing an adequate concentration of target objects is introduced into the channel from the inlet and the pressure difference between the inlet and outlet and capillary action induce a flow, delivering the samples across the sensor pixel grid of the CMOS sensor. Samples were typically imaged at a flow velocity of 200 $\mu\text{m}/\text{s}$, with a frame rate of 500 fps and a field-of-view (FOV) of 250 μm by 3mm. Note that the ultimate throughput limitation of SROFM is the speed of the CMOS image sensor. Even with our sensors (Aptina MT9T001), assuming the same fixed data transfer rate, with a more restricted FOV of 50 μm by 100 μm and maximum frame rate of 75000 fps, our current device could image a continuous stream of cells at a rate of 1300 HR images/sec with each image possibly containing multiple cells; to further increase the throughput of our device, we could use a high speed global shutter CMOS image sensors.

In multiframe pixel super-resolution techniques, the quality of the reconstructed HR image depends largely on knowledge of the precise sub-pixel shifts between subsequent images, collectively termed the motion vector of the LR image sequence. While the motion vector of a LR image sequence is in theory a known set of values in pixel super-resolution schemes involving precision scanning stages or actuators, implementation of a compact, micro-scanning system would not only be difficult and costly, but also prone to structural stability issues that could affect the accuracy of the motion vector. In contrast, the motion vector in SROFM can be estimated, quite accurately, by analyzing the rough position of the sample across the LR image sequence since the flow of the sample is highly stable within the microfluidic channel (low Reynolds number). For the simplest assumption of a sample flowing at constant velocity, the motion vector can be calculated from the location of the sample in the first and last frames. However, in many cases, the sample's motion is not strictly uniform or purely translational due to the geometry of the sample itself, defects in the microfluidic channel or changes in the flow rate. To compensate for this non-uniform motion, we developed several fast image processing techniques, discussed in the supplementary material S1, to estimate the motion vector from the LR sequence.

Once the motion vector of the LR image sequence is calculated, a shift-and-add pixel super-resolution algorithm can be applied to reconstruct a single HR image [16]. Such an algorithm consists of shifting each LR image by the relative sub-pixel shift given by the computed motion vector and adding them all together to fill a blank HR image grid of enhancement factor of n , where each n -by- n pixel area of the HR image grid corresponds to a single 1-by-1 pixel area of the LR image grid. The Wiener deconvolution method is then used to remove pixel blurring in the final HR image. Fig. 5-2 shows both LR and HR SROFM images of several microscopic objects: a 15 μm microsphere, *protist Euglena gracilis* ($d = \sim 15\mu\text{m}$) and *Entamoeba invadens* cysts ($d = \sim 25\mu\text{m}$). Taking into account the Nyquist sampling criteria and image sensor pixel size of 3.2 μm , the resolution limit of each LR image should be 6.4 μm . Note that each individual LR image contains very little spatial information about the sample other than its rough location and size, but each HR image is clearly improved in resolution. Conventional microscope images taken with a 20x objective are also shown for comparison.

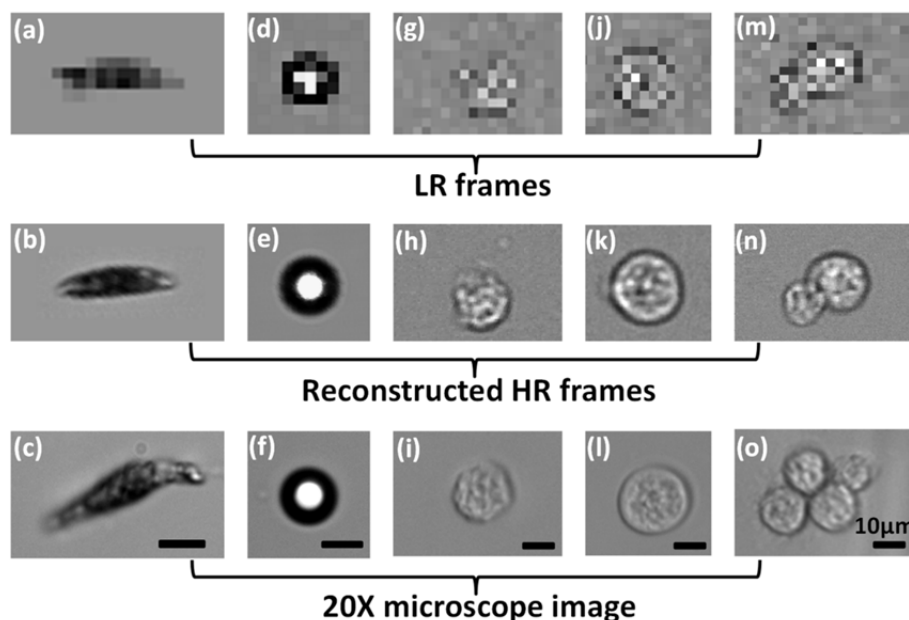


Figure 5-2: Images obtained from the SROFM device. *Euglena gracilis* (a-c), microsphere (d-f) and *Entamoeba invadens* cysts (g-o). Raw low-resolution (LR) images from the sensor (Top row), high-resolution (HR) images reconstructed from the sequence of LR images (Middle row), and conventional bright field microscope images taken with 20x objective lens (Bottom row). 40 to 50 LR frames were used to reconstruct each HR image.

5.3.2 Imaging of rotating sample

SROFM is not only simpler than the previous aperture-based OFM, but also more robust and able to image samples flowing with non-uniform translational motion and even rotation. Since the motion vector of a LR image sequence with SROFM is estimated from the image sequence itself, precise flow control is no longer required. Hence, whereas aperture-based OFM would utilize an additional electrokinetic driving scheme to ensure uniform flow, SROFM devices can be used with a drop-and-flow scheme, where a small volume of liquid sample is injected from the inlet and drawn into the channel by capillary action and the pressure difference between inlet and outlet. Even though the flow rate will gradually decrease as pressure between the inlet and the outlet equalizes, a non-linear motion vector can be estimated and used to reconstruct a high quality HR image.

Furthermore, SROFM can image samples flowing with rotational movement, as long as the rate of rotation is slow relative to the image capture frame rate. Fig. 4b shows the sequence of HR images of a cell near the channel side wall, flowing with both in-plane and out-of-plane rotation.

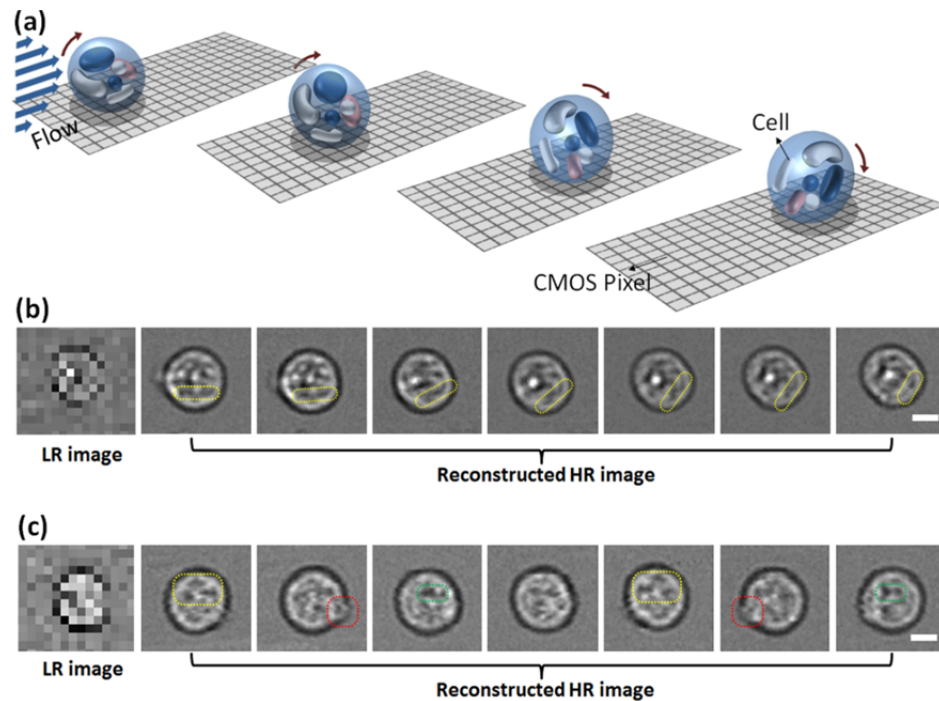


Figure 5-3 (color): Sequential HR images of rotating cells (scale bar 10 μm). (a) Cells flowing with rotational movement allow the SROFM to capture images of different projections, revealing the three-dimensional inner cellular structures. (b) HR sequence of an *Entamoeba invadens* cyst traveling with in-plane rotation. Note that the highlighted part of the sample is rotating in the sequence. The length of the dark spot in the highlighted region is also decreasing in the time lapse, indicating that the sample has out-of-plane rotation as well. (c) Sample translating with out-of-plane rotation. The highlighted regions with the same color reveal that the pairs of images are rotated 180 degrees out-of-plane of each other. Each pair of images is distinct from the others, showing the complex inner structure of the cell from a different projection plane.

SROFM's ability to image samples with rotational movement provides us with the unique opportunity to image samples from different perspectives. When cells rotate out-of-plane while flowing through the channel, we can observe the cells from different projections, and hence better resolve their three-dimensional inner structures. The requisite rotational motion for such imaging is naturally provided by the interaction of the cell with the non-uniform flow velocity profile of pressure-driven laminar fluid flow in the microfluidic channel. Fig. 4c shows sequential HR images of an *Entamoeba invadens* cyst rolling in the channel. Note that pairs of images highlighted with the same color are mirror images of each other, indicating that the cell has rotated 180 degrees along the direction of flow. These images reveal the three-dimensional location of each of the dark and bright spots in the cyst, as well as its external morphology. 350 frames of the LR image sequence were used to reconstruct the HR images, with 50 LR frames used for each HR frame. The motion blur due to the rotation within each 50 frames is not itself significant in the HR images, but if the rate of rotation of the sample is too fast relative to the translational movement, then the rotation blur would degrade the image quality. Additional modification in the design of the microfluidic channel could help control the rotation of the sample to achieve consistent rotational imaging without significant motion-blur. As such, we can perform rotational imaging with SROFM without any additional scanning stages or multiple light sources. The flexible ability of SROFM in imaging samples that are rotating or flowing with non-uniform velocities is a significant advantage over other designs.

5.3.3 Reconstruction of high-resolution video

SROFM can not only acquire HR still images of samples, but also capture HR videos of the samples as they flow through the channel and interact with the fluid. This is accomplished by using a sliding window sampling approach in combination with the pixel super-resolution algorithm (Fig. 5, See supplementary material S2 for the reconstructed HR video). We demonstrate HR video of *Entamoeba invadens* cysts flowing within the channel. In S2, we observe multiple non-rotating cysts flowing across the channel, a single rotating cyst and a single cyst flowing with out-of-plane rotation. To reconstruct each frame of each HR video, 45 LR frames were used with an enhancement factor $n = 7$.

SROFM's implementation of pixel super-resolution HR video reconstruction may find many practical applications, including the monitoring of the dynamic behavior, rotation and deformation, of a cell in a fluidic channel and creation of synthetic "video zoom", where a region of interest within a video sequence is enlarged and enhanced by some factor.

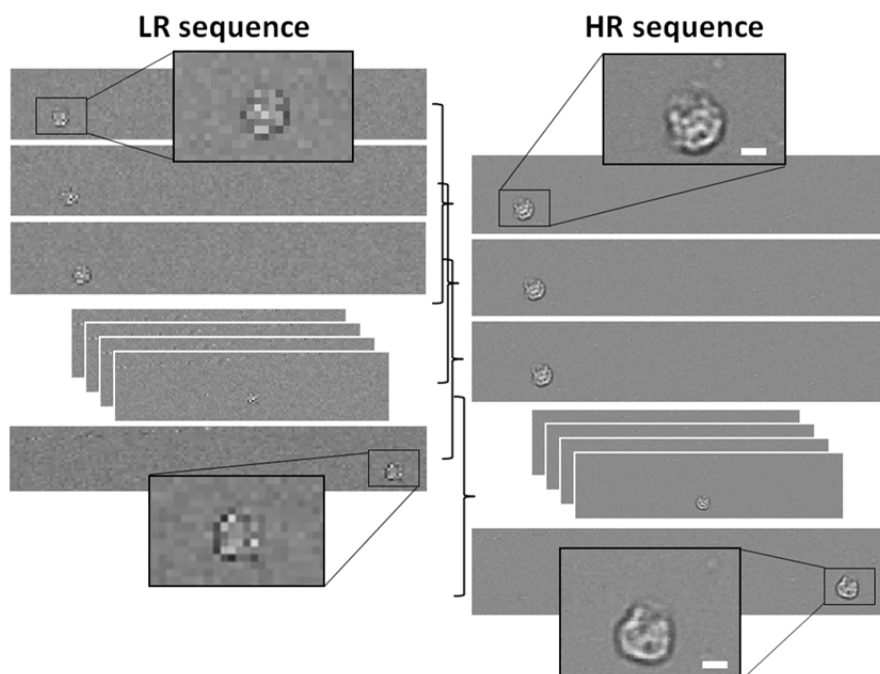


Figure 5-4: Reconstruction of HR video using the multiframe pixel super-resolution algorithm (scale bar = 10 μm).

5.3.4 Resolution of SROFM

To establish the extent of resolution improvement, we imaged a solution of 0.5 μm microspheres. Figure 3 shows the reconstructed HR image of a 0.5 μm sphere with the enhancement factor of 10 and 13. The centers of these microspheres can clearly be resolved and identified with the full width half maximum of 0.80 μm and 0.65 μm . The second data set implies that our prototype has a resolution limit of $\sim 0.75 \mu\text{m}$ (adjacent particles can be resolved as long as they are 3 or more HR pixels apart). Note that the resolution of a conventional microscope resolution with 20x objective lens is 0.84 μm , which can be obtained by

$$r = 0.61\lambda/NA \quad (5-1)$$

, where NA is the numerical aperture of the objective lens and λ is the wavelength of light. For aperture-based OFM, 0.8 μm resolution has been achieved with 1- μm apertures [4]. It has been shown that the resolution of aperture-based OFM is dependent on the aperture diameter and that a 450-nm aperture can achieve ~ 400 nm resolution [17]. Resolution of SROFM can also be improved by using smaller LR pixel size and/or higher enhancement factor with longer LR sequences.

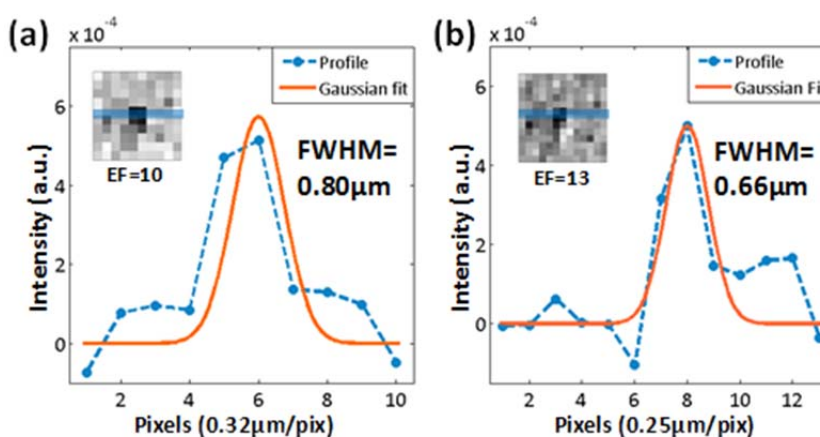


Figure 5-5 (color): Resolution of the SROFM prototype obtained with 0.5 μm microspheres. (a) Intensity profile of the 0.5 μm sphere from image reconstructed with an enhancement factor of 10 (inset). (b) Intensity profile of the same sphere reconstructed with an enhancement factor of 13 (inset). FWHMs of the profiles in (a) and (b) are 0.8 μm and 0.66 μm , respectively.

5.4 Discussion

We proposed and demonstrated a new on-chip optofluidic microscope that utilizes a multiframe pixel super-resolution algorithm to capture and reconstruct HR images and videos of biological samples. The novel combination of a pixel super-resolution and optofluidic approach towards microscopy removes the need for bulky and expensive lenses, coherent illumination sources and precision microscanning mechanisms. In addition, the SROFM system also allows us to capture images and videos of rotating samples in high

resolution and, thereby, reveal three-dimensional sub-cellular structures from different perspectives.

SROFM's simplicity, compactness, and cost-effectiveness make it well-suited for drop-and-flow screening of fluidic samples such as blood, urine or water. We believe that the SROFM technique can potentially play a significant role in the eventual development and commercialization of a mass-distributed, portable microscope for point-of-care analysis and third-world diagnostics, for the detection of water-borne parasites, blood-borne parasites and diseases involving blood cell deformations.

Bibliography

- [1] G. Zheng, S. A. Lee, S. Yang *et al.*, "Sub-pixel resolving optofluidic microscope for on-chip cell imaging," *Lab Chip*, vol. 10, no. 22, pp. 3125-3129, 2010.
- [2] X. Heng, D. Erickson, L. Baugh *et al.*, "Optofluidic microscopy --- method for implementing a high resolution optical microscope on a chip," *Lab on a Chip*, vol. 6, no. 10, pp. 1274-1276, 2006.
- [3] J. Garcia-Sucerquia, W. Xu, M. Jericho *et al.*, "Immersion digital in-line holographic microscopy," *Optics letters*, vol. 31, no. 9, pp. 1211-1213, 2006.
- [4] X. Cui, L. Lee, X. Heng *et al.*, "Lensless high-resolution on-chip optofluidic microscopes for *Caenorhabditis elegans* and cell imaging," *Proceedings of the National Academy of Sciences*, vol. 105, no. 31, pp. 10670, 2008.
- [5] N. Lindquist, A. Lesuffleur, H. Im *et al.*, "Sub-micron resolution surface plasmon resonance imaging enabled by nanohole arrays with surrounding Bragg mirrors for enhanced sensitivity and isolation," *Lab on a Chip*, vol. 9, no. 3, pp. 382-387, 2009.
- [6] S. Seo, T. Su, D. Tseng *et al.*, "Lensfree holographic imaging for on-chip cytometry and diagnostics," *Lab on a Chip*, vol. 9, no. 6, pp. 777-787, 2009.
- [7] E. Schonbrun, W. Ye, and K. Crozier, "Scanning microscopy using a short-focal-length Fresnel zone plate," *Optics letters*, vol. 34, no. 14, pp. 2228-2230, 2009.
- [8] G. Zheng, X. Cui, and C. Yang, "Surface-wave-enabled darkfield aperture for background suppression during weak signal detection," *Proceedings of the National Academy of Sciences*, vol. 107, no. 20, pp. 9043, 2010.
- [9] E. Schonbrun, A. Abate, and P. Steinvurzel, "High-throughput fluorescence detection using an integrated zone-plate array," *Lab on a Chip*, vol. 10, no. 7, pp. 852-856, 2010.
- [10] G. Zheng, and C. Yang, "Improving weak-signal identification via predetection background suppression by a pixel-level, surface-wave enabled dark-field aperture," *Optics letters*, vol. 35, no. 15, pp. 2636-2638, 2010.

- [11] D. Breslauer, R. Maamari, N. Switz *et al.*, “Mobile Phone Based Clinical Microscopy for Global Health Applications,” *PLoS ONE*, vol. 4, no. 7, pp. e6320, 2009.
- [12] J. Wu, X. Cui, G. Zheng *et al.*, “Wide field-of-view microscope based on holographic focus grid illumination,” *Opt. Lett.*, vol. 35, no. 13, pp. 2188-2190, 2010.
- [13] Y. Wang, G. Zheng, and C. Yang, “Characterization of acceptance angles of small circular apertures,” *Opt. Express*, vol. 17, pp. 23903-23913, 2009.
- [14] W. Bishara, T. Su, A. Coskun *et al.*, “Lensfree on-chip microscopy over a wide field-of-view using pixel super-resolution,” *Optics Express*, vol. 18, no. 11, pp. 11181-11191, 2010.
- [15] S. Hu, X. Ren, M. Bachman *et al.*, “Surface modification of poly (dimethylsiloxane) microfluidic devices by ultraviolet polymer grafting,” *Anal. Chem.*, vol. 74, no. 16, pp. 4117-4123, 2002.
- [16] M. Elad, and Y. Hel-Or, “A fast super-resolution reconstruction algorithm for puretranslational motion and common space-invariant blur,” *IEEE Transactions on Image Processing*, vol. 10, no. 8, pp. 1187-1193, 2001.
- [17] X. Heng, X. Cui, D. W. Knapp *et al.*, “Characterization of light collection through a subwavelength aperture from a point source,” *Opt. Express*, vol. 14, no. 22, pp. 10410-10425, 2006.

Chapter 6

Surface-wave-enabled darkfield aperture

The third accessing point in design considerations is the image sensor. Imager modification is an emerging technique that performs pre-detection light field manipulation. In this chapter, we present a novel optical structure design, termed surface-wave-enabled darkfield aperture (SWEDA) [1], which can be directly incorporated onto optical sensors to accomplish pre-detection background suppression. This SWEDA structure consists of a central hole and a set of groove pattern that channels incident light to the central hole via surface plasmon wave and surface scattered wave coupling. We show that the surface wave component can mutually cancel the direct transmission component, resulting in near-zero net transmission under uniform normal-incidence illumination. In this chapter, we report the implementation of two SWEDA structures. The first structure, circular-groove based SWEDA, is able to provide polarization independent suppression of uniform illumination with a suppression factor of 1230. The second structure, linear-groove-based SWEDA, is able to provide a suppression factor of 5080 for TM wave and can serve as a highly compact (length = 5.5 micron) polarization sensor (the measured TE/TM transmission ratio is 6100). A detection system that can effectively suppress background contributions (prior to detection) and allow detection of small signals in extremely compact device architectures is potentially useful for a broad range of applications from on-chip bio-sensing to metrology and microscopy.

6.1 Background

There is a growing interest in miniaturized microscopy systems [2-11]. Compact, inexpensive and portable imaging systems can fulfill many needs in biological research, point-of-care analysis and field diagnostics. For example, an on-chip microscope, produced at scale at existing semiconductor foundries and capable of imaging blood cell or parasite

morphology in high resolution, would bring affordable healthcare diagnostics to less developed populations in rural settings, where it is too costly to deploy expensive conventional microscopes and skilled technicians.

The ability of a sensor to observe a weak optical signal in the presence of a strong background can be significantly limited even if the sensor is fully capable of measuring the same weak signal in the absence of background [12, 13]. There are several factors that can contribute to this degradation in sensitivity, and their relative significance is dependent on the measurement scenarios involved.

The case of stars in the sky provides a good illustration of some of these limitations. A bright star that is quite visible at night may disappear from our sight during the day. This disappearing act is attributable to two major factors. First, the bright daytime background can introduce a proportionate noise term that the brightness of the star must exceed in order to be observable. Second, our eyes naturally adjust their dynamic range to accommodate the bright daytime background. As the bit depths of most measurement systems (including our eyes) are finite, we necessarily view the sky with a coarser brightness scale during the day. If the incremental brightness of the star versus the background is smaller than this gradation scale, the star is simply indistinguishable from its background.

The approach of adding bit depth can address part of the problem; however, it is an ‘engineering’ solution that comes at a price of more sophisticated electronics and greater data volume. Moreover, it does not eliminate the proportionate noise term from the background. Interference arrangements can potentially be employed to destructively interfere and cancel the background (for situations where the light sources involved are coherent). However, such schemes are understandably elaborate and non-trivial to employ. A sensor that can intrinsically cancel a strong background prior to signal detection would be a simpler solution with broad applicability.

In this chapter, we report a novel sensor structure that accomplishes this type of darkfield sensing for coherent light field in a robust, compact and simple format. This structure, termed surface-wave-enabled darkfield aperture (SWEDA), operates by interfering surface wave with the direct light transmission component in such a way that a uniform light field at normal incidence will actually generate no detectable signal in a

sensor bearing this structure. A sensor bearing SWEDA is insensitive to the background normal-incidence light field but is, instead, highly sensitive to weak localized light field variations or light fields at non-zero incident angles that disrupt the exquisitely balanced interference condition.

We will next describe the operating principle of the proposed structure. Then, we will report on our simulations and experimental implementation of a polarization-independent SWEDA, which utilizes a circular groove pattern for surface wave coupling. We next extend the SWEDA concept to a polarization-sensitive case by using a linear groove pattern for surface wave coupling. Finally, we report on our experimental demonstration of the ability of the circular-groove-based SWEDA to detect weak signals in the presence of a strong background; we also present a proof-of-concept that, amongst other applications, shows that sensors based on such structures can be used to implement a new class of darkfield microscopes.

6.2 SWEDA concept

The light interaction between the subwavelength features on a metal-dielectric interface has been a subject of intensive study in recent years [14-31]. It has been shown that appropriately patterned rings of metal corrugation around a hole can significantly change the total amount of light transmission through the aperture [15, 17, 18, 22, 23, 25, 27]. One primary component involved in such a light-interaction between the central hole and the metal corrugation is the surface plasmon (SP) wave, the electromagnetic surface wave existing at the interface between a dielectric and a noble metal [32]. SP wave exhibits intrinsic field localization at the interface and thus allow for the manipulation of light in the subwavelength scale. Recently, some theoretical and experimental results [18, 21-24, 28, 30] also show that SP wave is not the only component involved in the light-interaction of subwavelength features on the metal-dielectric interface. A surface scattered component also plays a role at the short range interaction. Therefore, the mediated-transmission behavior of this corrugation based aperture can be intuitively explained as follows. When light falls on a patterned groove structure on the metal, it couples into the surface wave, including the SP wave and the surface scattered wave. By choosing the groove periodicity

such that the surface wave launched at each groove adds up in phase, we can generate a strong propagative surface wave that is directed towards the hole. The surface wave can then be converted back to a propagating optical wave at the central hole. In essence, the groove structure serves as an antenna for light collection and uses the surface wave to transport the collected optical power to the hole. Using this approach, researchers have reported both light transmission enhancement and suppression [15, 17, 18, 22, 25, 33].

Our SWEDA design differs from previous surface-wave-modulated aperture design by exactly balancing the direct transmission component of the central hole and the surface wave component induced from the grooves (for clarity, we refer to the center opening as the central hole and the entire structure as the aperture). This creates a situation where the two transmission components can interact significantly – thus providing an additional means for light manipulation. To be specific, we precisely control the amplitude of the surface wave by changing the periodicity and depth of the groove structure. Through judicious choice of the groove structure and the central hole size, we can arrive at a situation where the surface wave component is equal in strength to the direct transmission component. Furthermore, we can adjust the phase lag between the surface wave and the direct transmission component by choosing the gap between the innermost groove and hole appropriately. If we adjust this phase lag such that the optical wave generated by the surface wave component is 180 degree out-of-phase with the direct transmission component, the two components will destructively interfere and result in little or no light transmits through the hole in the presence of uniform normal-incidence illumination. Since this destructive interference condition critically depends on an exact balance of the two mentioned components, a small change in spatial distribution of the input light field intensity or phase will disrupt the destructive interference condition and permit significant light transmission through the hole.

In the context of high sensitivity optical signal detection, the advantage of SWEDA can be easily appreciated. The structure can effectively suppress a uniform normal-incidence background from reaching the underlying sensor and instead only permit highly localized light field variations or light fields at non-zero incidence angles to pass through and be detected. As such, the underlying sensor no longer needs to contend with a high

background and its associated noise fluctuation terms. The bit depth can also be optimized and devoted to the detection of the weaker light field variations. Used in an appropriate manner, such devices can potentially allow for greater signal detection sensitivity in weak-signal-buried-in-high-background scenarios. This method also enables a new way to build darkfield microscopes on the sensor level that does not rely on elaborate bulk optical arrangements.

6.3 SWEDA device

6.3.1 SWEDA with circular groove pattern

The first type of SWEDA is shown in Fig. 6-1(A). It adopts a circular pattern for the groove design. We refer to this structure as the circular-groove-based SWEDA. Due to its circular symmetry nature, this type of SWEDA provides a polarization-independent behavior for signal detection and imaging. We began the implementation of such a SWEDA by using a commercial software (CST Microwave Studio) to perform a set of simulations to understand the interplay between our design parameter choices and system characteristics. The simulations were performed at a nominal wavelength of 738 nm. The permittivity of gold at this wavelength is $-19.95 + 1.48i$ [34]. The simulations were performed in 3 dimensions. The calculation domain was $12 \lambda \times 12 \lambda \times 3 \lambda$ and contained ~ 12 million meshes. The transmission of the SWEDA and single hole were calculated by integrating the Poynting vector over a $6 \lambda \times 6 \lambda$ region (0.85λ beneath the aperture). For all simulations, we applied a perfect match layer (PML) at the outer boundaries.

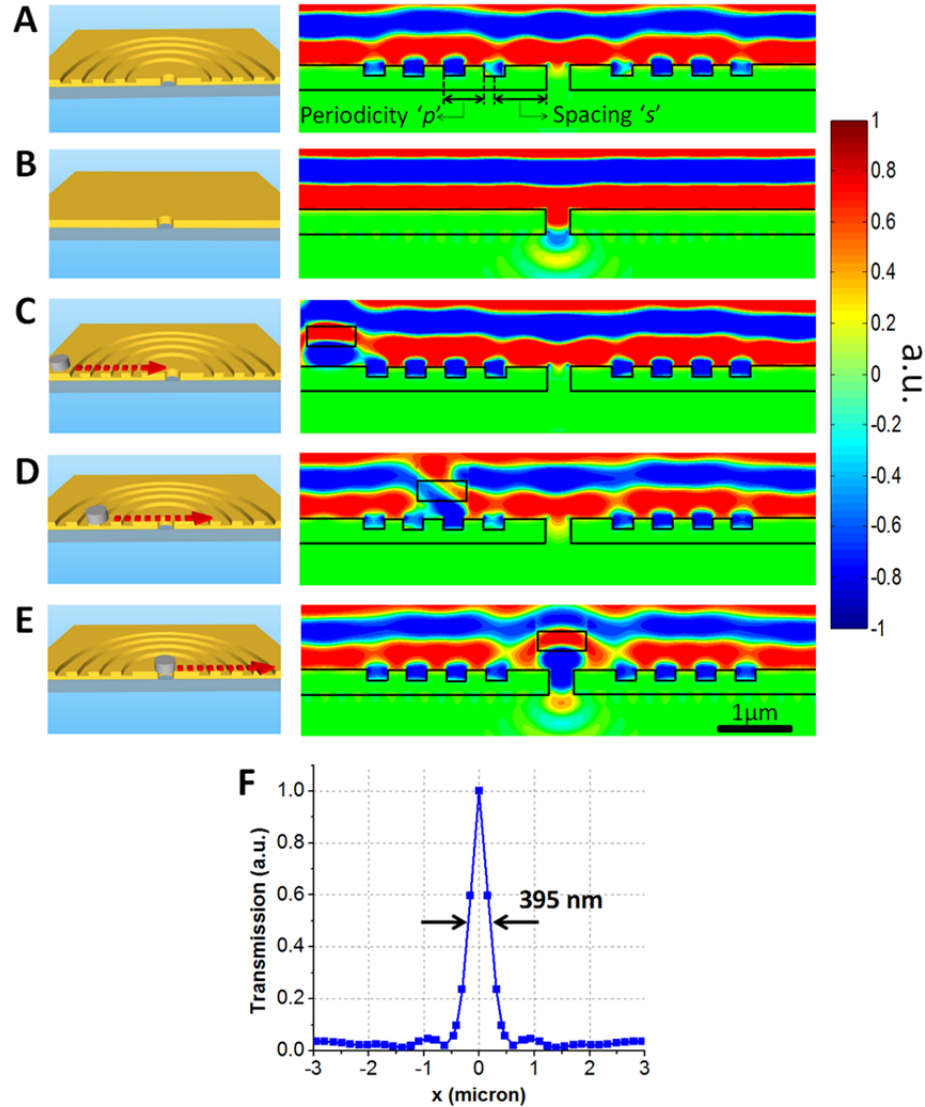


Figure 6-1 (color): Simulations of the circular-groove based SWEDA. Displayed is the real part of the electric-field at $\lambda = 738$ nm (equivalent to the time-domain fields at the instant of time when the source phase is zero). (A) The optimized SWEDA structure, where $s = 774.3$ nm, $p = 560$ nm, thickness of gold = 340 nm, diameter of hole = 300 nm and groove depth=140 nm and refractive index of the dielectric substrate = 1.5. The simulation predicts that the darkfield suppression factor of this structure equals 6640. (B) Simulation for the simple hole. (C-E) Simulations of a cylindrical scatterer (radius 300 nm, thickness 200 nm, displacement height 300 nm, permittivity 2.25) transiting across the SWEDA. (F) The transmission signal curve from the SWEDA as the cylindrical scatterer (the same as (C)-(E)) moves across it. The full width at half maximum was determined to be 395 nm.

There are primarily 4 specific parameters that impact the performance of the SWEDA; they are: 1) Groove periodicity and groove depth. The groove periodicity (defined here as the p -parameter in Fig. 6-1(A)) and groove depth can be adjusted to control the magnitude of the surface wave coupled into the structure. Note that the exact match of the groove periodicity to the wavelength of the surface wave is not necessarily desired, as this may induce an overly strong surface wave component, which cannot be matched by the direct transmission component. 2) The number of grooves. The strength of the coupled surface wave increases as a function of groove numbers. On the other hand, we desire a low number of grooves for overall SWEDA structure compactness considerations. 3) Central hole size. This affects the strength of the direct transmission component. We would additionally aim to restrict the aperture size such that the light transmission is not multi-moded. Multi-mode light transmission significantly complicates the destructive interference balancing act as we would need to achieve destructive interference between the surface wave component and the direct transmission component for all modes involved. 4) The distance between the innermost groove and the rim of the central hole (defined here as the s -parameter in Fig. 6-1(A)) determines the phase difference between the surface-wave induced and the direct transmission components. To accomplish exact cancellation of the two components, we require this phase difference to be 180 degrees. Other parameters such as the groove profile can also be used to tune the surface wave component; however, from the fabrication point of view, the profile of the groove is not as easy to control as the 4 parameters we mentioned.

The simulation program allowed us to map out the interplay of these parameters and the overall SWEDA system characteristics. We define the darkfield suppression factor as the ratio of the total power transmission through a simple hole (without grooves) to the total power through a SWEDA. For good darkfield performance, we desire this ratio to be as high as possible. We were able to arrive at a design parameter set (Fig. 6-1(A)) that provides a suppression factor of 6640 by the simulation program. The simulated electric-field distributions for this particular SWEDA design (Fig. 6-1(A)) and that of a corresponding simple hole (Fig. 6-1(B)) are shown here. We can see that the SWEDA structure should indeed be able to suppress light transmission through the central hole

significantly. We next simulated the translation of a cylindrical dielectric object (radius 300 nm, thickness 200 nm, displacement height 300 nm, permittivity 2.25) across the top of the SWEDA structure (Fig. 6-1(C-F)). We can see that the SWEDA began to transmit light significantly when the object's presence directly above the central hole significantly perturbed the direct transmission component and, consequently, disrupted the delicately balanced destructive interference condition. We further observed that the presence of the object above the groove structures did perturb the SWEDA to a certain extent as well. However, the impact was much less significant (Fig. 6-1(F)); this can be well appreciated by noting that the generation of surface wave occurred over the entire area associated with the ring grooves and localized changes of the light field over the area had a diminished impact on the overall surface wave component. As a whole, this simulation indicates that the SWEDA is maximally sensitive to light field heterogeneity directly above the central hole.

We next fabricated a number of SWEDA structure based on the parameters suggested by our simulation results. Fig. 6-2(A) shows the scanning electron microscope (SEM) image of a typical SWEDA that we have created by focus ion beam (FIB) milling. The fabrication process can be described as following: We started with a 2 nm thick titanium layer (adhesion layer) and 340-nm-thick gold layer that were coated on a 1-mm-thick glass substrate by an e-beam evaporator (Temescal BJD-1800). A focused ion beam (FEI Nova200 dual-beam system using Ga⁺ ions with a 5 nm nominal beam diameter) was employed to perform milling. A low ion beam current was used (30 pA, 30 keV) in the milling process to accomplish the requisite fine structure. We fabricated a set of 13 SWEDAs with different spacing 's' ranging from 540 nm to 1020 nm. A single hole without the groove structure was also fabricated to serve as a control. To characterize the optical property of the SWEDA, we used a tunable wavelength laser (Spectra-Physics Tsunami continuous wave Ti: Sapphire) as the illumination source. The transmissions through the apertures were collected by an inverted microscope with a 20X objective lens.

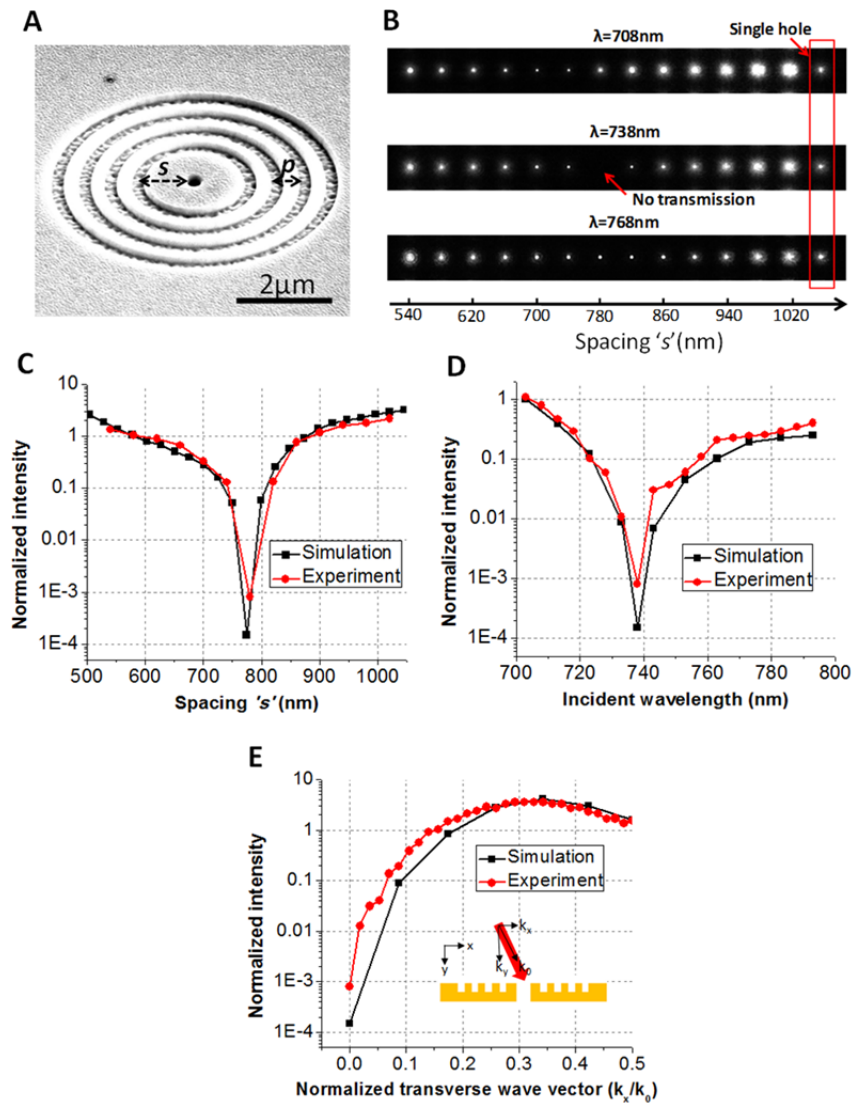


Figure 6-2 (color): Experimental characterization of the circular-groove-based SWEDA. (A) The SEM image of a typical fabricated SWEDA. (B) The optical transmission images of the 13 SWEDAs and the reference single-hole under normal-incidence illumination for three different wavelengths. (C) The measured optical transmission signals from SWEDAs with different ‘s’ ranging from 540 nm to 1020 nm (left to right). The signals from the SWEDA were normalized by single hole (signal from the single hole at normal incidence was set to unity). The simulated intensity is also shown for comparison. (D) The normalized optical transmission signals of SWEDA ($s = 780$ nm) with different incident wavelengths. (E) The normalized optical transmission signals of SWEDA with different normalized transverse wave vector.

Fig. 6-2(B) shows the optical transmission images of the 13 SWEDAs and the reference single-hole at normal incidence for three different wavelengths. We can see that the spacing parameter ‘ s ’ does indeed have a significant impact on the transmission of the SWEDA structures. The transmission intensity measured for these SWEDA structures are plotted in Fig. 6-2(C) (wavelength of 738 nm); we used the unadorned simple hole for normalization. The simulation prediction for each of the structures is also plotted for comparison. From the plots, the implemented SWEDA structure with s -parameter of 780 nm exhibited the desired near-zero transmission characteristics. The optimized SWEDA’s structure parameters were a close match with our simulation predictions – the s -parameter differed by 6 nm (less than 0.8%). The measured suppression factor for the optimized SWEDA was 1230. In other words, this SWEDA transmitted 1230 times less light than an unadorned simple hole of size equal to that of the central SWEDA hole.

We next measured the spectral response of the optimized SWEDA over a spectral range of 700 nm to 790 nm. Since SWEDA’s operation depends on the exact amplitude balance and opposing phase relationship of the surface-wave-assisted transmission component and the direct transmission component, we can expect that the darkfield property of SWEDA to be optimized for one single wavelength. Fig. 6-2(D) shows the experimentally measured and simulation-predicted spectral transmission of the SWEDA. As expected, there is a single minimum over the range of interest and the transmission increased monotonically away from this point. It is also worth noting that the suppression factor actually remained fairly high (> 50) for a bandwidth of ~ 10 nm.

For a given incident light field, we can decompose it into different plane wave component with respect to the transverses wave vector [35]. In Fig. 6-2(E), we measure the transmission of the SWEDA as a function of the normalized transverses wave vector (k_x/k_0). Fig. 6-2(E) represents the system transfer function of the SWEDA: SWEDA rejects the normal incident plane wave component and transmits other components with efficiency as dictated by this transfer function.

The good agreement between the experimental and simulated spacing, wavelength and transverses wave vector trends, as evident in Fig. 6-2(C), (D), and (E), is a proof of the SWEDA working principle. The discrepancy in darkfield suppression factor is attributable

to fabrication imperfections associated with the FIB milling process. We tend to end up with rounded structure edges experimentally. Another contribution might be the variation in groove depth due to the intrinsic roughness of the groove bottom (metals mill non-uniformly as a function of grain orientation due to channeling). If exact matches of experiments and simulation are desired in specific applications, such imperfections may be mitigated by employing a sacrificial layer, as described in Ref. [36], during fabrication to help preserve the sharpness of edges.

6.3.2 SWEDA with linear groove pattern

The second type of SWEDA is shown in Fig. 6-3(A) and 6-3(B). It adopts a linear pattern for the groove design (refer as the linear-groove-based SWEDA), and as such, it is highly sensitive to the polarization state of the incident light. As shown in Fig. 6-3(A), incoming TM polarized light (where the electric-field is perpendicular to the groove structure) can be collected and converted into a surface wave by the periodic grooves and then be recoupled into propagating light through the central hole. On the other hand, the TE (with magnetic-field perpendicular to the groove structure) coupling efficiency of the SP wave, a major component of the total surface wave, is much smaller than the TM case [32], and thus, the absence of interference with SP wave permits significant TE polarized light transmission through the hole in Fig. 6-3(B). Fig. 6-3(C) and 6-3(D) show the simulations of this SWEDA at a nominal wavelength of 750 nm (the permittivity of gold at this wavelength is $-20.96 + 1.55i$ [34]). We were able to arrive at a set of design parameters that provide a darkfield suppression factor of 35400 for TM wave in our simulations. The simulated magnetic-field distributions for this particular design are shown in Fig. 6-3(C). In Fig. 6-3(D), we also show the electric-field distributions for the TE wave, from which we can see that the structure does transmit TE wave significantly. The difference between the TM and TE cases also verifies the surface-wave-enabled mechanism of the linear-groove-based SWEDA, since the SP wave can only be induced efficiently for TM polarization [32]. We also note that, from the simulations shown in Fig. 6-3(C) and 6-3(D), the linear-groove-based SWEDA provides a polarization extinction ratio of 42500 for the two orthogonal polarization states.

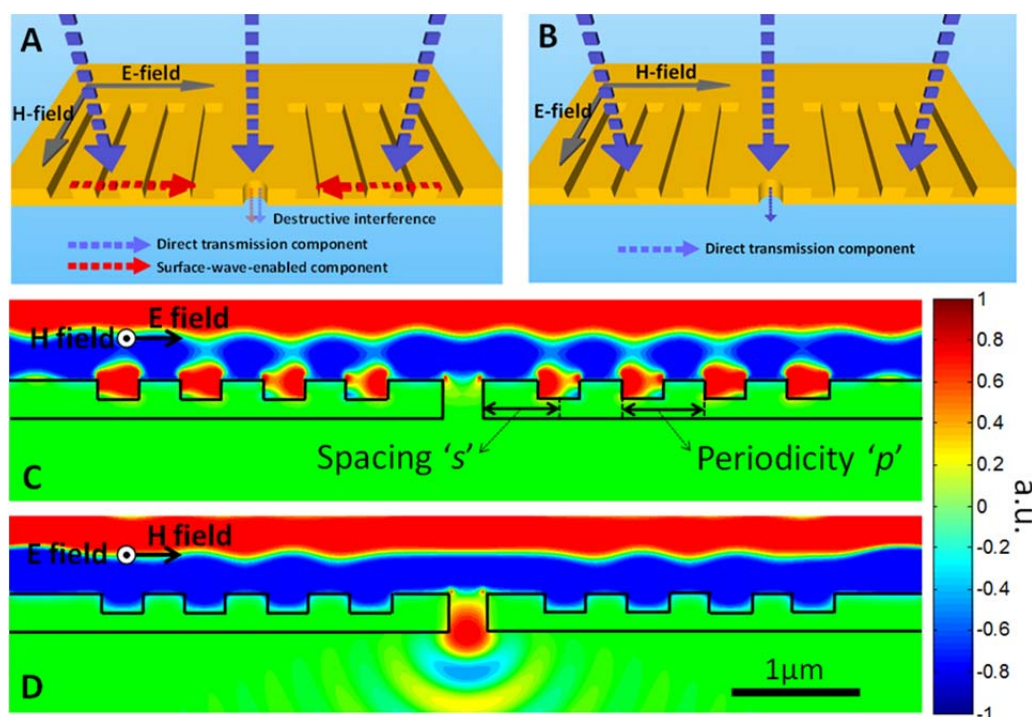


Figure 6-3 (color): Working principle and simulation of the linear-groove based SWEDA. (A) The TM incident light is coupled into surface wave by the linear groove pattern. The destructive interference between the surface wave component and the direct transmission component results in zero transmission. (B) The TE incident light cannot be coupled into SP waves (a primary component of the total surface wave), and transmission is induced in the absence of destructive interference. (C) Simulation of the TM case. Displayed is the real part of the electric-field at $\lambda = 750$ nm. The parameters of the optimized SWEDA are: $s = 658$ nm, $p = 660$ nm, thickness of gold = 340 nm, diameter of hole = 300 nm, groove depth = 140 nm and refractive index of the dielectric substrate = 1.5. The simulation predicts a TM darkfield suppression factor of this structure versus a simple hole is 35400. (D) Simulation of the TE case. Displayed is the real part of the magnetic-field at $\lambda = 750$ nm. The simulation predicts the polarization extinction ratio of the two orthogonal polarization states is 42500.

We next fabricated a number of linear-groove-based SWEDAs with linear groove patterns. Fig. 6-4(A) shows the SEM image of a typical linear-groove-based SWEDA that

we have created by FIB milling. We fabricated a set of 9 linear-groove-based SWEDAs with different spacing ‘s’ ranging from 455 nm to 775 nm. The optical transmission signals of linear-groove-based SWEDAs are normalized and plotted as a function of spacing ‘s’ and wavelength ‘ λ ’ in Fig. 6-5. The measured darkfield suppression factor for the optimized linear-groove based SWEDA was 5080. In other words, this structure transmitted 5080 times less TM light than an unadorned simple hole of size equal to that of the central SWEDA opening. In Fig. 6-4(B), a light field is incident on the SWEDA with a polarization angle θ – this geometry is used for our subsequent measurements. The optical images with different polarization angles are shown in Fig. 6-4(C), and the normalized signals of SWEDAs are plotted in Fig. 6-4(D). The measured polarization extinction ratio is 6100, meaning that the amount of TE light transmission through the linear-groove-based SWEDA is 6100 times higher than the TM case. Such a high extinction ratio positively indicates that the linear-groove-based SWEDA can serve as a highly compact and highly efficient polarization sensor.

Fig. 6-5(A) shows the optical transmission images of the 9 linear-groove-based SWEDAs and the reference single-hole at normal-incidence TM illumination for three different wavelengths. We can see that the spacing parameter ‘s’ does indeed have a significant impact on the TM transmission of these structures. The TM transmission intensity measured for these linear-groove-based SPEDAs with different spacing ‘s’ are plotted in Fig. 6-5(B) (wavelength of 750 nm); we used the transmission of the unadorned simple hole for normalization. The simulation prediction for each of the structures is also plotted for comparison. From the plots, we can see that the implemented linear-groove-based SWEDA structure with s-parameter of 655 nm exhibited the desired near-zero transmission characteristics. The optimal structure parameters were a close match with our simulation predictions – the s-parameter differed by 3 nm (less than 0.5%). The measured darkfield suppression factor for the optimized linear-groove-based SWEDA was 5080. In other words, this structure transmitted 5080 times less TM light than an unadorned simple hole of size equal to that of the central SWEDA hole. We next measured the spectral transmission response of the optimized linear-groove-based SWEDA over a spectral range of 700 nm to 800 nm. Since operation of the linear-groove-based SWEDA depends on the

exact balance and opposing phase relationship of the surface-wave-assisted transmission component and the direct transmission component, we can expect that the TM darkfield property of linear-groove-based SWEDA to be optimized for only a single wavelength. Fig. 6-5(C) shows the experimentally measured and simulation-predicted spectral transmission. As expected, there is a single minimum over the range of interest and the transmission increases monotonically away from this point. It is also worth noting that the suppression factor actually remained fairly high (> 50) for a bandwidth of ~ 10 nm.

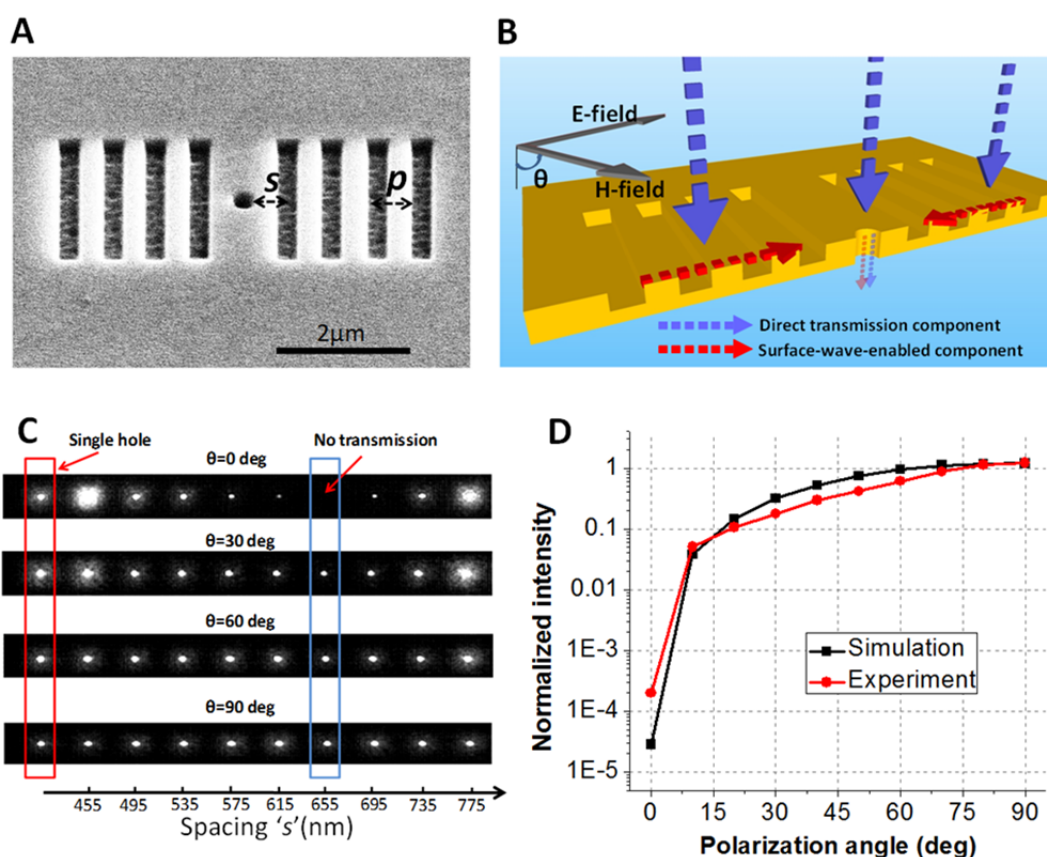


Figure 6-4 (color): Experimental characterization of the linear-groove-based SWEDA. (A) The SEM image of a typical fabricated SWEDA. (B) The light is incident on the SPEDA with a polarization angle θ . (C) The optical transmission images of the SWEDAs for different polarization angles at $\lambda = 750$ nm. (D) The normalized optical transmission signals of SWEDA are plotted as a function of polarization angle. The measured polarization extinction ratio for TE and TM incidence is 6100.

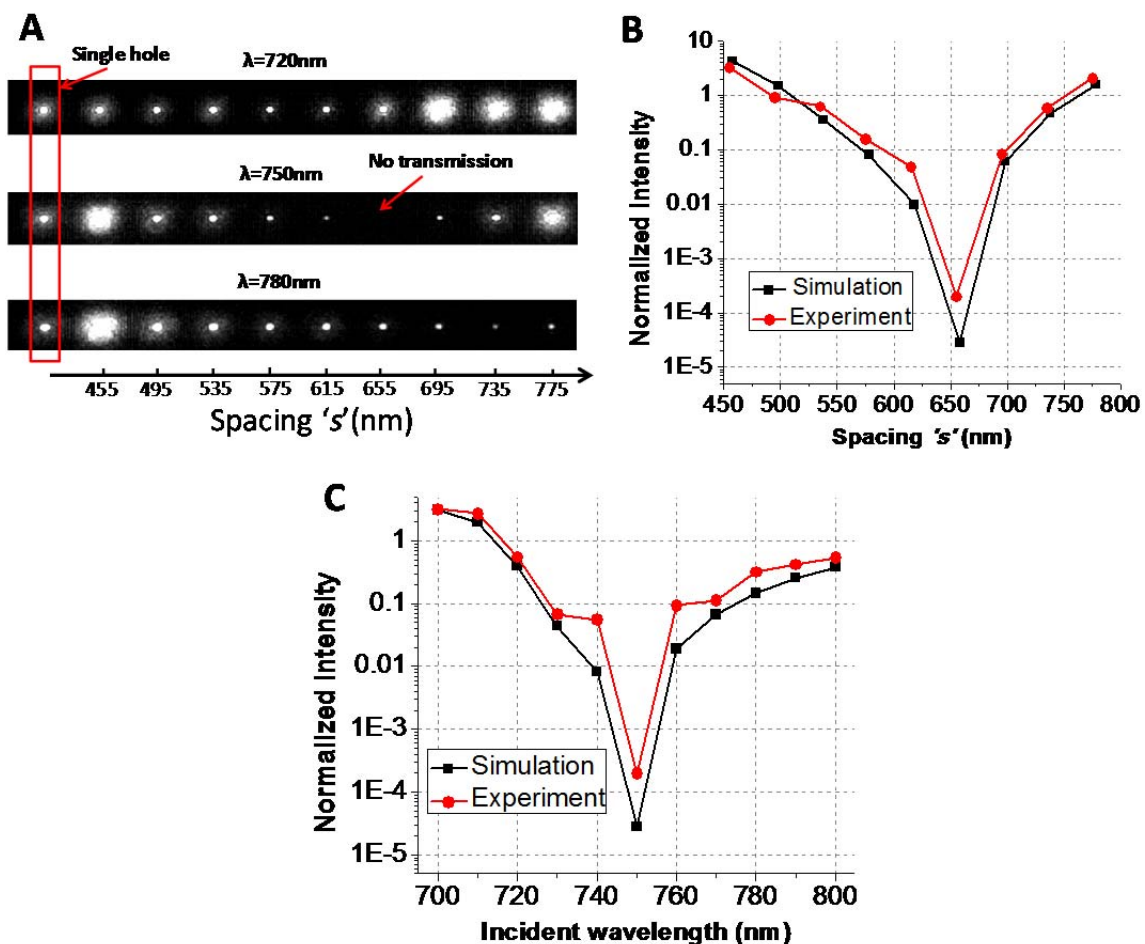


Figure 6-5 (color): Transmission characterization of the linear-groove-based SWEDA.

(A) The optical transmission images of the 9 SWEDAs and the reference single-hole under normal-incidence illumination for three different wavelengths. (B) The measured optical transmission signals from SWEDAs with different spacing ' s ' ranging from 455 nm to 775 nm (left to right). The signals from the SWEDA were normalized by single hole (signal from the single hole at normal incidence was set to unity). The measured suppression factor for the optimized SWEDA is 5080. The simulated intensity is also shown for comparison. (C) The measured normalized optical transmission signals from SWEDA ($s = 655$ nm) with different incident wavelengths. The simulation result is also shown for comparison.

6.4 Boosting detection sensitivity by SWEDA

Due to the polarization-independent nature of the circular-groove based SWEDA, it can be used to suppress a bright normal-incidence background regardless of the incident light field's polarization state. The ability of such a SWEDA to improve small signal detection is illustrated in the following experiment. We prepared a sample comprised of an ITO-coated glass slide that was marked with shallow pits of radius of 175 nm and 250 nm via the FIB (Fig. 6-6(A) and 6-6(B)). Next, we transmitted a uniform light field of intensity about 0.2 W/cm² from a 738 nm laser through the sample. We then used a 1:1 relay microscope to project a virtual image of the pits onto our optimized circular-groove-based SWEDA (see Methods for more details). We next raster-scanned the sample and measured the light transmission through the SWEDA at each point of the scan. We then generated an image of the sample from the collected data. As is evident in Fig. 6-6(C) and 6-6(D), SWEDA allowed us to identify the presence of the two pits with little difficulty. We next acquired images of the same pits (Fig. 6-6(E) and 6-6(F)) with a simple camera (based on the same sensor chip). It is difficult to identify the presence of the two pits in this case. The total light fluence incident on the sample for both the SWEDA and camera image acquisitions was kept the same to allow for direct result comparisons.

Fig. 6-6(G) shows plots of signal traces across the images. The SWEDA-acquired data were normalized on the same scale. The camera image data were normalized versus the average background signal. The backgrounds associated with the SWEDA-acquired data were low and the contributive signals from the pits were well discernible. In fact, the contributive signals were sufficiently well-resolved that we can use them to quantify their relative strengths for the two pits. In comparison, the high backgrounds in the camera images combined with the associated noise masked the scattering contributions from the pits. The measured contrast improvement was 25 dB for the 175 nm pit and 27 dB for the 250 nm pit.

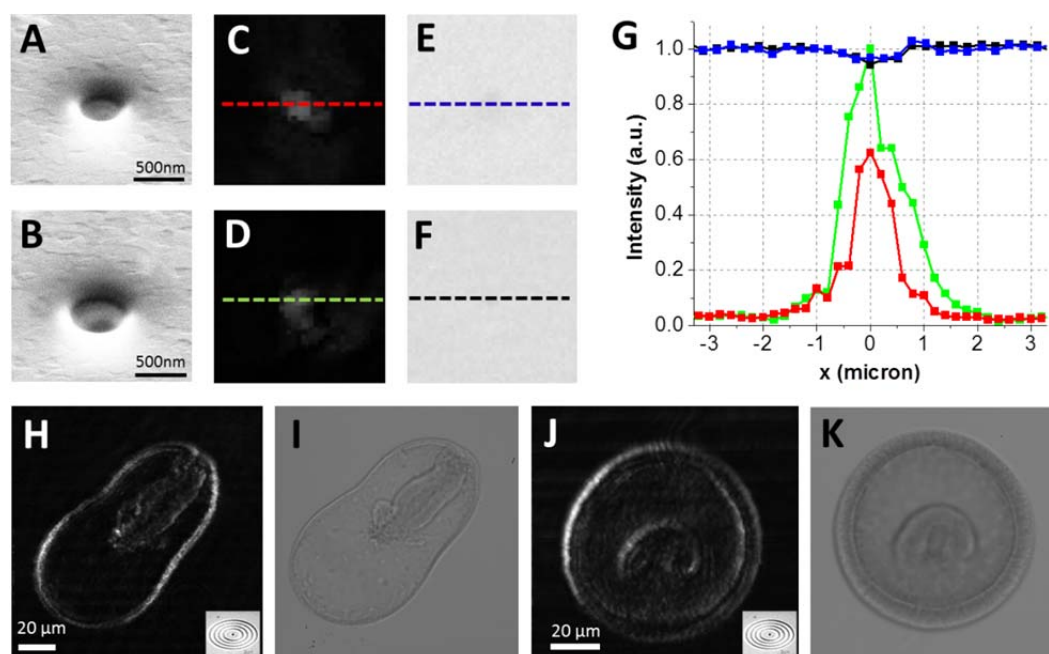


Figure 6-6 (color): The sensitivity enhancement demonstration for the circular-groove based SWEDA. (A and B) The SEM images of the 175 nm and 250 nm pits on the ITO coated glass. (C and D) The SWEDA-based raster-scanned images of the samples (A) and (B). (E and F) Microscope images of the samples (A) and (B) under the same illumination condition as the SWEDA collected images using a conventional camera with the same CMOS chip. (G) Center line traces of the images in (C-F). Please see (C-F) for color reference guide. The observed image contrast (signal / background) enhancement is ~ 25 dB for the 175 nm pit and ~ 27 dB for the 250 nm pit. (H and J) The SWEDA-based raster-scanned images of the starfish embryos. (I and K) Conventional bright field microscope images.

As pointed out in our introduction, circular-groove-based SWEDA can potentially be employed to perform darkfield microscopy imaging at the sensor level. The principle involved is substantially different from that of a conventional darkfield microscope. While a conventional system depends on oblique illumination and a relatively small objective angle of collection to screen out the uniform background via a fairly sophisticated bulk optical arrangement, the ability of circular-groove-based SWEDA to screen out uniform background presents a more direct approach. To demonstrate that such a system can indeed

be implemented, we employed our optimized circular-groove based SWEDA in the same experimental scheme to scan slides of starfish embryos in different developmental stages. The illumination intensity was 0.2 W/cm^2 . Fig. 6-6(H) and 6-6(J) show the results. Similar images of the specimens taken with a standard microscope are shown in Fig. 6-6(I) and 6-6(K) for comparison. We can see that the SWEDA generated image has a dark background, as is consistent with a darkfield microscope image. We can also see that the edge and interior of the starfish embryo appeared brighter in the SWEDA image and darker in the control image. This is again consistent with our expectations of a darkfield image as sample locations with substantial scattering should appear brighter in a darkfield image and darker in a simple transmission image. We would like to emphasize that this is a proof-of-concept experiment. A feasible darkfield microscope can be implemented by employing a laser as the light source in a standard microscope and using a sensor chip patterned with a grid of tightly spaced circular-groove-based SWEDA as the microscope camera.

6.5 Biotin-streptavidin biosensing with SWEDA

Another application of SWEDA is for highly sensitive biosensing experiments. In particular, the widely used biotin-streptavidin reaction could be adapted for use with SWEDA for the optical detection of streptavidin tagged molecules of interest, according to preliminary experiments and simulations. In this detection scheme, biotin is placed on the gold surface layer of the SWEDA. As a solution containing the corresponding streptavidin molecules brings these molecules into contact with the biotin-coated surface of the SWEDA, streptavidin molecules will bind to the biotin molecules, causing a local change in the index of refraction on the surface of the SWEDA structure. This change in the index of refraction will change the surface wave component of light, disturbing the delicate destructive interference condition and allowing light to be transmitted through. Hence, the presence of the streptavidin-tagged molecules would be converted into an optical signal by the SWEDA.

To explore this concept, we conducted a simulation using CST Microwave Studio again. We first optimized for a new set of parameters for the SWEDA structure to operate in water (refractive index 1.33). Next, to simulate streptavidin molecules, about 5 nm in

size with refractive index 1.45, we conducted another simulation with a 5 nm thick layer of streptavidin covering the entire surface. As we can see in Fig. 6-7, the presence of the streptavidin on the surface of the SWEDA breaks the deconstructive interference condition, allowing for much greater light transmission. The transmission ratio shown in Fig. 6-7(b) and 6-7(c) is about 1000. These simulation results demonstrate the feasibility of using SWEDA in biosensing applications with biotin and streptavidin. As our experimental findings indicate, SWEDA is a robust, structurally simple and highly compact approach to accomplish optical background suppression and/or polarized light field suppression. It is also worth noting that, in principle, there is no theoretical limit to how close the SWEDA darkfield suppression factor can approach infinity; the practical limit is only set by the fabrication tolerance and the net transmission through the opaque metal layer.

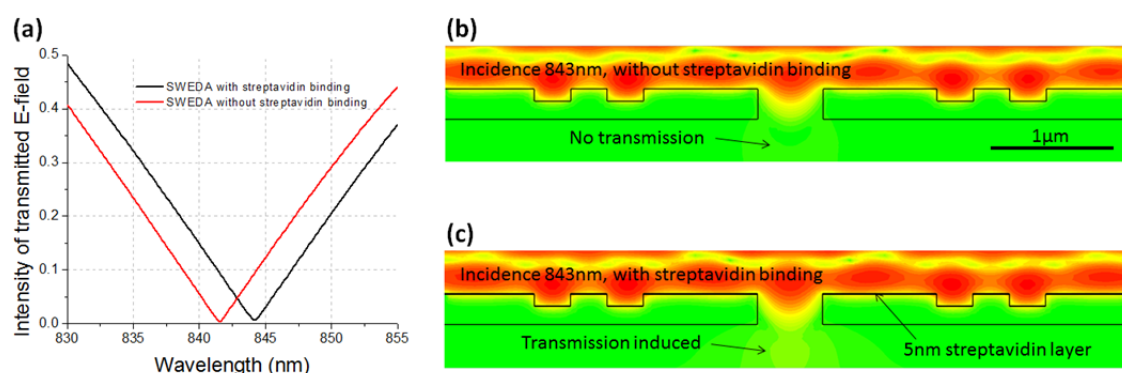


Figure 6-7 (color): Biotin-streptavidin biosensing with SWEDA. (a) The spectrum of intensity of transmitted E-field (the intensity of incident E-field is set to be 1). (b) The E-field intensity distribution without streptavidin binding. (c) The E-field intensity distribution with 5 nm streptavidin binding.

Compared with the conventional surface-plasmon-resonance (SPR) sensor, the proposed platform does not employ the Kretschmann configuration and is based on direct coupling of normally incident radiation, making this scheme very sensitive to localized changes in refractive index in the vicinity of the metallic surface of the structure. The sensing approach described here does not require any prism coupling mechanism, thereby making the miniaturization of these sensors feasible.

6.6 Discussion

As our experimental findings indicate, SWEDA is a robust, structurally simple and highly compact approach to accomplish optical background suppression and/or polarized light field suppression. It is also worth noting that, in principle, there is no theoretical limit to how close the SWEDA darkfield suppression factor can approach infinity; the practical limit is only set by the fabrication tolerance and the net transmission through the opaque metal layer.

There are a few limitations associated with the SWEDA structure that are worth discussing presently. First, the structure is optimized for single wavelength operations. This limitation can be overcome by using more complicated SWEDA-type structures involving multibeam interference that can operate over a broad range of wavelengths. Second, the amount of light transmitted is largely limited by the size of the central hole. We believe that this issue can be potentially addressed by replacing the central opening of SWEDA with multiple C-shape apertures [37] to increase light collection efficiency. Third, this structure works well at only blocking uniform light field at normal incidence. Fortunately, the general SWEDA concept can be extended with asymmetric structure designs to screen out light at other incidence angles.

SWEDA technology can potentially be used in a range of different applications. The linear-groove-based SWEDA demonstrated in the present work is a highly compact and highly sensitive polarization sensor. Since the polarization state of light will change during the interaction with chiral materials, this SWEDA design may also find some applications in on-chip detection of some chiral materials such as sugar, proteins and DNA [38, 39]. The ability to fully suppress a coherent background as exhibited by the circular-groove-based SWEDA can be useful for small signal detections in metrology applications. It is especially applicable in detection scenarios where the overall background intensities fluctuate with time. As our background subtraction occurs at the individual pixel level, SWEDA technology removes the need for balanced detection schemes. The pre-detection background subtraction, which is a light cancellation process, is also intrinsically more sensitive than post-detection cancellation schemes that are susceptible to intrinsic detection

statistical variations. The inclusion of chemical reagents in the central hole can also turn such a SWEDA structure into a high-sensitivity sensor that can react to small refractive index changes of the reagents.

From a practical implementation viewpoint, SWEDA structures can be fabricated directly on top of CCD or CMOS sensor pixels. The small size and planar design of SWEDA make such implementation particularly suited for foundry fabrication. Sensor chips with broad-bandwidth SWEDA can then be used in place of the standard camera sensor to accomplish sensor level darkfield imaging. Such systems, in combination with a coherent light source, can transform a standard microscope into a simpler and cheaper darkfield microscope than current darkfield microscopes. Such systems can also enable edge-detection imaging in machine vision applications if the illumination source employed is coherent. A SWEDA array can also replace the hole array in the optofluidic microscope (OFM) [2, 4] – a low-cost, lensless and high resolution microscopy approach, to accomplish darkfield microscopy imaging on a chip. The use of SWEDA in this case is especially appropriate as both the OFM and SWEDA implementation are well suited for semiconductor mass-fabrication. In fact, it is difficult to envision a more compact and cost-effective approach for incorporating darkfield ability in an OFM system.

Finally, we would like to note that the general concept of exact balancing the surface-wave-induced component and direct light transmission component in a destructive interference manner is a novel idea that can inspire other surface-wave-structures with novel properties. Effectively, such structures are tiny interferometers (~ 6 microns or less) that can be fabricated on a single metal substrate and which have excellent stability (our SWEDA structures exhibited no significant performance drift over the entire duration of our experiments). Since the structure is planar, it can be mass produced in a semiconductor foundry. The proposed structure can also be redesigned for operation at longer wavelengths. As an example of other potential applications, we believe that the concept of SWEDA can be applied to optical isolation in an ultra-compact format, polarization control in semiconductor lasers [40], wavefront detection, extending depth of field of the type II aperture-based imaging device [41], and perspective imaging [42] by customizing the optical transfer function on the pixel level.

Bibliography

- [1] G. Zheng, X. Cui, and C. Yang, "Surface-wave-enabled darkfield aperture for background suppression during weak signal detection," *Proceedings of the National Academy of Sciences*, May 3, 2010, 2010.
- [2] X. Heng, D. Erickson, L. Baugh *et al.*, "Optofluidic microscopy ---- method for implementing a high resolution optical microscope on a chip," *Lab on a Chip*, vol. 6, no. 10, pp. 1274-1276, 2006.
- [3] J. Garcia-Sucerquia, W. Xu, M. Jericho *et al.*, "Immersion digital in-line holographic microscopy," *Optics letters*, vol. 31, no. 9, pp. 1211-1213, 2006.
- [4] X. Cui, L. Lee, X. Heng *et al.*, "Lensless high-resolution on-chip optofluidic microscopes for *Caenorhabditis elegans* and cell imaging," *Proceedings of the National Academy of Sciences*, vol. 105, no. 31, pp. 10670, 2008.
- [5] N. Lindquist, A. Lesuffleur, H. Im *et al.*, "Sub-micron resolution surface plasmon resonance imaging enabled by nanohole arrays with surrounding Bragg mirrors for enhanced sensitivity and isolation," *Lab on a Chip*, vol. 9, no. 3, pp. 382-387, 2009.
- [6] S. Seo, T. Su, D. Tseng *et al.*, "Lensfree holographic imaging for on-chip cytometry and diagnostics," *Lab on a Chip*, vol. 9, no. 6, pp. 777-787, 2009.
- [7] E. Schonbrun, W. Ye, and K. Crozier, "Scanning microscopy using a short-focal-length Fresnel zone plate," *Optics letters*, vol. 34, no. 14, pp. 2228-2230, 2009.
- [8] E. Schonbrun, A. Abate, and P. Steinvurzel, "High-throughput fluorescence detection using an integrated zone-plate array," *Lab on a Chip*, vol. 10, no. 7, pp. 852-856, 2010.
- [9] G. Zheng, and C. Yang, "Improving weak-signal identification via predetection background suppression by a pixel-level, surface-wave enabled dark-field aperture," *Optics letters*, vol. 35, no. 15, pp. 2636-2638, 2010.
- [10] D. Breslauer, R. Maamari, N. Switz *et al.*, "Mobile Phone Based Clinical Microscopy for Global Health Applications," *PLoS ONE*, vol. 4, no. 7, pp. e6320, 2009.
- [11] J. Wu, X. Cui, G. Zheng *et al.*, "Wide field-of-view microscope based on holographic focus grid illumination," *Opt. Lett.*, vol. 35, no. 13, pp. 2188-2190, 2010.
- [12] R. Narayanaswamy, and O. Wolfbeis, *Optical sensors: industrial, environmental and diagnostic applications*. Springer Berlin, 2004.
- [13] G. C. Cox, *Optical imaging techniques in cell biology*, Boca Raton :: CRC/Taylor & Francis, 2007.
- [14] T. Ebbesen, H. Lezec, H. Ghaemi *et al.*, "Extraordinary optical transmission through sub-wavelength hole arrays," *Nature*, vol. 391, no. 6668, pp. 667-669, 1998.
- [15] T. Thio, K. M. Pellerin, R. A. Linke *et al.*, "Enhanced light transmission through a single subwavelength aperture," *Opt. Lett.*, vol. 26, no. 24, pp. 1972-1974, 2001.
- [16] H. Lezec, A. Degiron, E. Devaux *et al.*, "Beaming light from a subwavelength aperture," *Science*, vol. 297, no. 5582, pp. 820-822, 2002.
- [17] T. Thio, H. Lezec, T. Ebbesen *et al.*, "Giant optical transmission of sub-wavelength apertures: physics and applications," *Nanotechnology*, vol. 13, no. 3, pp. 429-432, 2002.
- [18] H. Lezec, and T. Thio, "Diffracted evanescent wave model for enhanced and suppressed optical transmission through subwavelength hole arrays," *Optics express*, vol. 12, no. 16, pp. 3629-3651, 2004.

- [19] R. Hollingsworth, and R. Collins, "Plasmon enhanced near-field optical probes," Google Patents, 2005.
- [20] H. Schouten, N. Kuzmin, G. Dubois *et al.*, "Plasmon-assisted two-slit transmission: Young's experiment revisited," *Physical Review Letters*, vol. 94, no. 5, pp. 53901, 2005.
- [21] L. Chen, J. Robinson, and M. Lipson, "Role of radiation and surface plasmon polaritons in the optical interactions between a nano-slit and a nano-groove on a metal surface," *Optics Express*, vol. 14, no. 26, pp. 12629-12636, 2006.
- [22] G. Gay, O. Alloschery, B. Viaris de Lesegno *et al.*, "The optical response of nanostructured surfaces and the composite diffracted evanescent wave model," *Nat Phys*, vol. 2, no. 4, pp. 262-267, 2006.
- [23] P. Lalanne, and J. Hugonin, "Interaction between optical nano-objects at metallo-dielectric interfaces," *Nature Physics*, vol. 2, no. 8, pp. 551, 2006.
- [24] L. Aigouy, P. Lalanne, J. Hugonin *et al.*, "Near-field analysis of surface waves launched at nanoslit apertures," *Physical Review Letters*, vol. 98, no. 15, pp. 153902, 2007.
- [25] D. Pacifici, H. Lezec, and H. Atwater, "All-optical modulation by plasmonic excitation of CdSe quantum dots," *Nature photonics*, vol. 1, no. 7, pp. 402-406, 2007.
- [26] A. Drezet, C. Genet, and T. Ebbesen, "Miniature plasmonic wave plates," *Physical Review Letters*, vol. 101, no. 4, pp. 43902, 2008.
- [27] E. Laux, C. Genet, T. Skauli *et al.*, "Plasmonic photon sorters for spectral and polarimetric imaging," *Nature Photonics*, vol. 2, no. 3, pp. 161-164, 2008.
- [28] H. Liu, and P. Lalanne, "Microscopic theory of the extraordinary optical transmission," *Nature*, vol. 452, no. 7188, pp. 728-731, 2008.
- [29] D. Pacifici, H. Lezec, L. Sweatlock *et al.*, "Universal optical transmission features in periodic and quasiperiodic hole arrays," *Optics Express*, vol. 16, no. 12, pp. 9222-9238, 2008.
- [30] B. Ung, and Y. Sheng, "Optical surface waves over metallo-dielectric nanostructures: Sommerfeld integrals revisited," *Optics Express*, vol. 16, no. 12, pp. 9073-9086, 2008.
- [31] G. Gbur, H. Schouten, and T. Visser, "Achieving superresolution in near-field optical data readout systems using surface plasmons," *Applied Physics Letters*, vol. 87, pp. 191109, 2005.
- [32] S. Maier, *Plasmonics: fundamentals and applications*: Springer Verlag, 2007.
- [33] D. Pacifici, H. Lezec, H. Atwater *et al.*, "Quantitative determination of optical transmission through subwavelength slit arrays in Ag films: Role of surface wave interference and local coupling between adjacent slits," *Physical Review B*, vol. 77, no. 11, pp. 115411, 2008.
- [34] E. Palik, and G. Ghosh, *Handbook of optical constants of solids*: Academic press, 1985.
- [35] J. Kong, *Electromagnetic wave theory*: EMW publishing, 2005.
- [36] J. Leen, P. Hansen, Y. Cheng *et al.*, "Improved focused ion beam fabrication of near-field apertures using a silicon nitride membrane," *Optics Letters*, vol. 33, no. 23, pp. 2827-2829, 2008.
- [37] X. Shi, L. Hesselink, and R. Thornton, "Ultrahigh light transmission through a C-shaped nanoaperture," *Optics letters*, vol. 28, no. 15, pp. 1320-1322, 2003.
- [38] G. Fasman, *Circular dichroism and the conformational analysis of biomolecules*: Plenum Pub Corp, 1996.

- [39] K. Minakawa, H. Yamada, K. Sasagawa *et al.*, “Microchamber Device Equipped with Complementary Metal Oxide Semiconductor Optical Polarization Analyzer Chip for Micro Total Analysis System,” *Jpn. J. Appl. Phys.*, vol. 48, no. 4, pp. 04C192, 2009.
- [40] N. Yu, Q. Wang, C. Pflugl *et al.*, “Semiconductor lasers with integrated plasmonic polarizers,” *Applied Physics Letters*, vol. 94, pp. 151101, 2009.
- [41] X. Heng, X. Cui, D. Knapp *et al.*, “Characterization of light collection through a subwavelength aperture from a point source,” *Optics express*, vol. 14, no. 22, pp. 10410-10425, 2006.
- [42] R. Ng, M. Levoy, M. Bredif *et al.*, “Light field photography with a hand-held plenoptic camera,” *Computer Science Technical Report CSTR*, vol. 2, 2005.

Chapter 7

Angle-sensitive pixel design for wavefront sensing

Conventional image sensors are only responsive to the intensity variation of the incoming light wave. By encoding the wavefront information into the balanced detection scheme, we demonstrate an image sensor pixel design that is capable of detecting both the local intensity and angular information simultaneously. With the full compatibility to the CMOS fabrication process, the proposed pixel design can benefit a variety of applications, including light field photography, phase microscopy, lensless imaging and machine vision.

7.1 Background

The concept of light field camera (or plenoptic camera) has received much attentions in recent years [1, 2]. Such a camera can capture both intensity and angular information of incoming light waves. Based on these two types of information, it is possible for the user to interactively change the focus, the view point and the perceived depth-of-field of the captured image upon digital post-processing. However, conventional CCD/CMOS image sensors can only capture a 2D intensity map of the incoming light wave; angular information is lost in the measurement process. To address this issue, several schemes have been developed to record both the intensity and the angular distribution of the light field, including the use of an array of conventional cameras [3], multiple masks in the optical path [4] and a microlens array [2]. These approaches recover the angular information based on the relative position between the external optical component and the imaging recording pixel array.

Recently, it is shown that, the measurement of the angular information can be integrated at the pixel level of a CMOS image sensor, termed light field imager [5-7]. Such a light field imager has been successfully demonstrated for synthetic refocusing, depth mapping, 3D localization and lensless imaging [5-7]. The key idea of this light field imager

is to encode the angular information in the intensity measurement at pixel level. It employs a pair of diffraction gratings placed above photodiodes to achieve angular sensitivity. Upon illumination, the top grating generates diffraction patterns that have periodicity identical to the grating pitch (Talbot effect). The bottom grating is used to selectively transmit the diffracted light to the photodiode below. In such a pixel design, there are two ambiguities needed to be addressed: 1) the ambiguity between the local intensity and the local incident angle; 2) the intrinsic periodicity of the angular response. To resolve these two ambiguities, 8 pixels are needed to fully determine the local angular information in two dimensions.

In this chapter, we present a simple angle-sensitive pixel (ASP) design based on the balanced detection scheme. We combined 4 conventional pixels to form one ASP group. The summation of pixel values represents the local light intensity and the difference of pixel values represents the local incident angle. This chapter is structured as follows. We will first describe the principle of the proposed ASP. Next, we will report on our full wave simulation of the ASP design for two typical pixel structures. Finally, we will draw our conclusion at the end of this chapter.

7.2 Angle-sensitive pixel design

7.2.1 Principle

The proposed ASP design is shown in Fig. 7-1(a), where 4 conventional pixels share one top metal opening. The cross-section view in x-z plane is shown in Fig. 7-1(b1) and (b2). In the rest of the paper, we will focus our discussion on the angular response at x direction. The case for y direction can be treated in the same manner. As shown in Fig. 7-1(b1), upon normal incidence, readout of pixel 1 is exactly the same as pixel 2, and we refer this case as the balanced state. With a non-zero incident angle θ shown in Fig. 7-1(b2), the readout of pixel 1 is higher than that of pixel 2 and the incident angle can be recovered from the intensity difference of these two pixels.

In the large scale limit (i.e., the ray-optics limit), intensity readouts of pixel 1 and 2 can be expressed as

$$I_1 = I_0(w - h * \tan\theta/n), I_2 = I_0(w + h * \tan\theta/n) \quad (7-1)$$

, where I_0 is the local intensity of the incoming wave, n is the refraction index of the passivation layer, w is the opening size of individual pixels (denoted in Fig. 7-1(b1)), h is the thickness of the top passivation layer. The local intensity of the light wave can be simply measured by pixel binding, i.e., $(I_2 + I_1)$. The incident angle in x direction can be recovered based on the following equation:

$$\theta = \arctan\left(\frac{n \cdot w}{h} \frac{I_2 - I_1}{I_2 + I_1}\right) = \arctan\left(\frac{n \cdot w}{h} \frac{\Delta I}{I_{total}}\right) \quad (7-2)$$

, where ‘ w/h ’ is a structure parameter to characterize the angular sensitivity of the ASP. A smaller ‘ w/h ’ promises a higher angular sensitivity, with the tradeoff in the total measurement range and the pixel crosstalk.

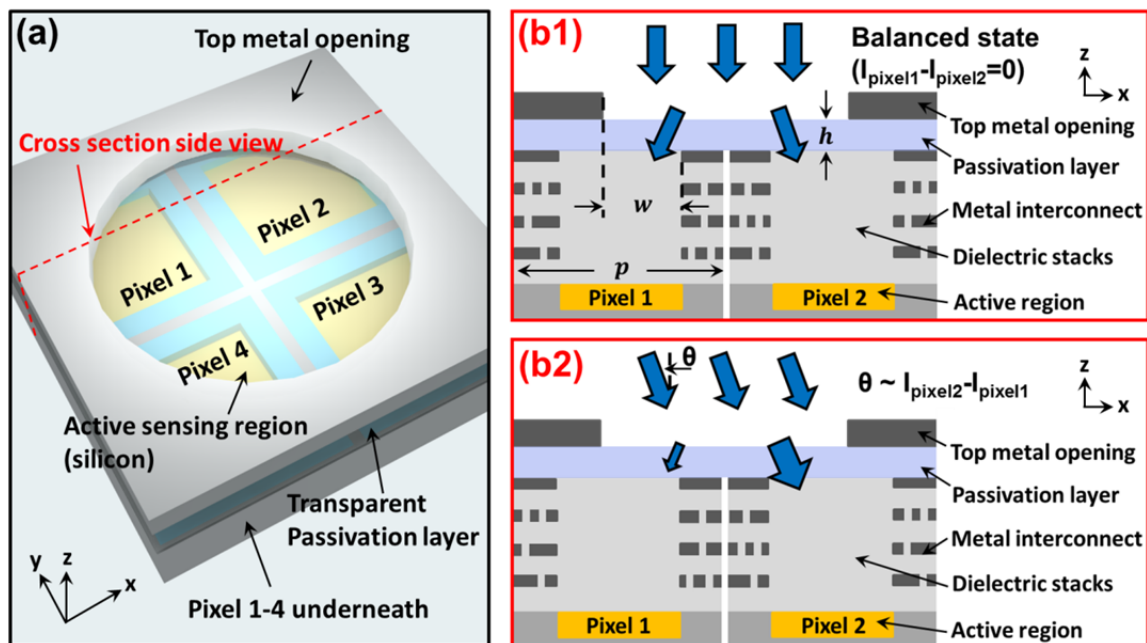


Figure 7-1 (color): (a) The proposed ASP design. (b1) Balanced state of the ASP under normal incidence. (b2) The incident angle can be recovered based on the difference of the two pixel values.

7.2.2 Simulations of the angle-sensitive pixel design

In a practical CMOS image sensor pixel design, the size of individual pixel is at the micrometer scale (For example, the pixel size of image sensor in most of mobile modules

ranges from 1.1 to 3 micrometers). The light diffraction effect at this scale plays an important role in the angular response of the proposed ASP. Next, we will present our FDTD-based full-wave simulations for two types of ASP design, one for the front-side illuminated pixel structure and the other for the back-side illuminated structure.

Fig. 7-2 demonstrates an ASP design based on a 2.2 μm front-side illuminated pixel structure. In this design, the size of entire ASP is 4.4 μm ; the top metal opening is 2.4 μm ; the refractive index and the thickness of the passivation layer is 1.47 and 1.2 μm . To reduce the complexity of the simulation, we use perfect electric conductor as metal layers. The bottom part of the ASP is the silicon layer, where we define a 1.6 μm * 1 μm region (denoted by the dash line) as the active sensing area for power flow integration. Two types of simulation result are given in Fig. 7-2: the electric field (Fig. 7-2(a1) and (b1)) and the time averaged power flow (Fig. 7-2(a2) and (b2)). Fig. 7-2(a) demonstrates the case of the balanced state, corresponding to Fig. 7-1(b1). Fig. 7-2(b) demonstrates the case of 10 degree incidence, corresponding to Fig. 7-1(b2). In Fig. 7-1(b2), the power flow in the active region of pixel 2 is higher than that of pixel 1, and the ratio between I_1 and I_2 is determined to be 2.5 from this simulation.

An important feature shown in Fig. 7-2 is the diffraction-based focusing effect of the top metal opening. In Fig. 7-2(a2), as the light wave passes through the top metal opening, the effective beam width decreases; in other words, the top metal opening acts an effective lens to focus the light wave into the center part of the ASP. In this regard, we can define an effective opening size w_{eff} to correct for w defined in Eq. (7-1). For Fig. 7-2(a2), the effective w_{eff} is about 1.8 times smaller than the w .

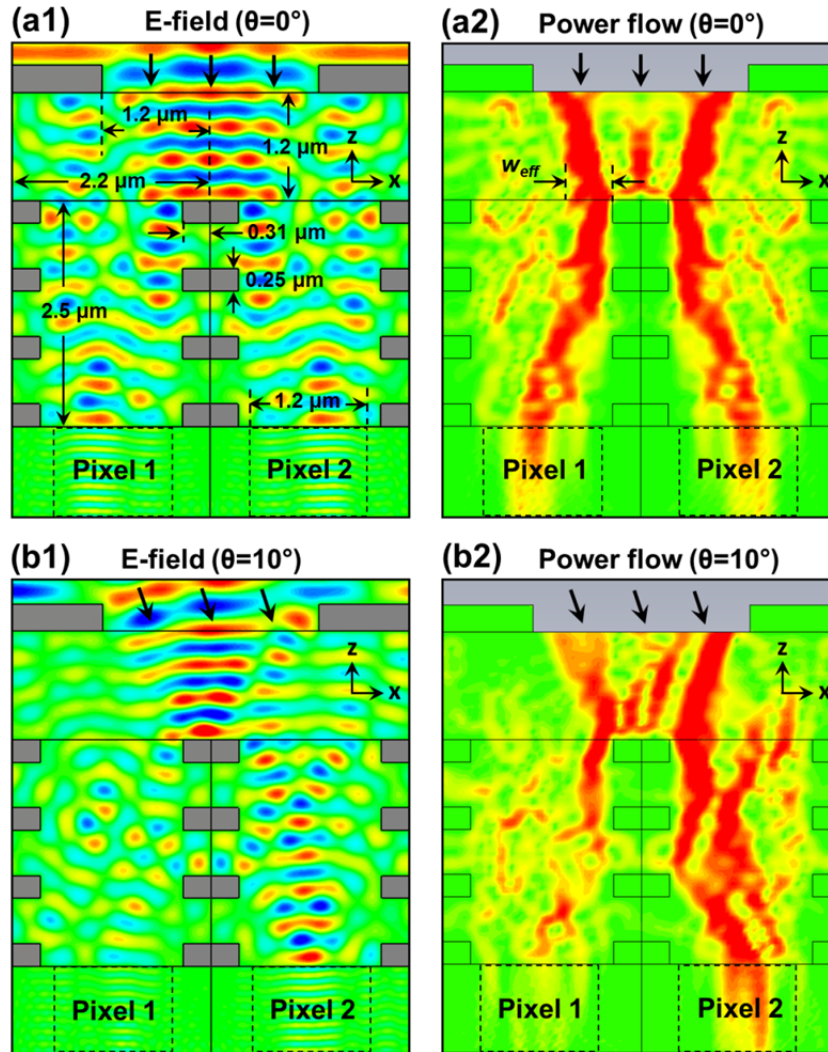


Figure 7-2 (color): The FDTD simulation of the front-side illuminated ASP design with normal incidence (a) and 10 degree incidence (b). The wavelength is chosen to be 550 nm, the center of visible spectrum.

The angular response of the front-side illuminated ASP is shown in Fig. 7-3. We observe that $(I_2 - I_1)/(I_2 + I_1)$ is a monotonically increasing function with respect to the incident angle θ . Therefore, there is no ambiguity for the angular response for different θ s. In Fig. 7-3(b), we also compare the simulation result with the theoretical calculation based on Eq. (7-1). The effective opening size w_{eff} is used to correct the focusing effect of the top metal opening. We can see that the overall trends of these two curves are in a good

agreement with each other. However, there are also some discrepancies worth discussing. The simulated angular sensitivity is higher than that of Eq. (7-1) for small incident angles, and lower for large incident angles. Such discrepancies can be attributed to the uniform light ray assumption used in Eq. (7-1). Due to the focusing effect of the top metal opening, the actual power flow is stronger in the center of the ASP. Therefore, for small incident angles, the focused light wave enters into one of the individual pixels, resulting in a steeper slope of the angular response in Fig. 7-3(b). The lower angular sensitivity at larger incident angles can be explained in a similar manner.

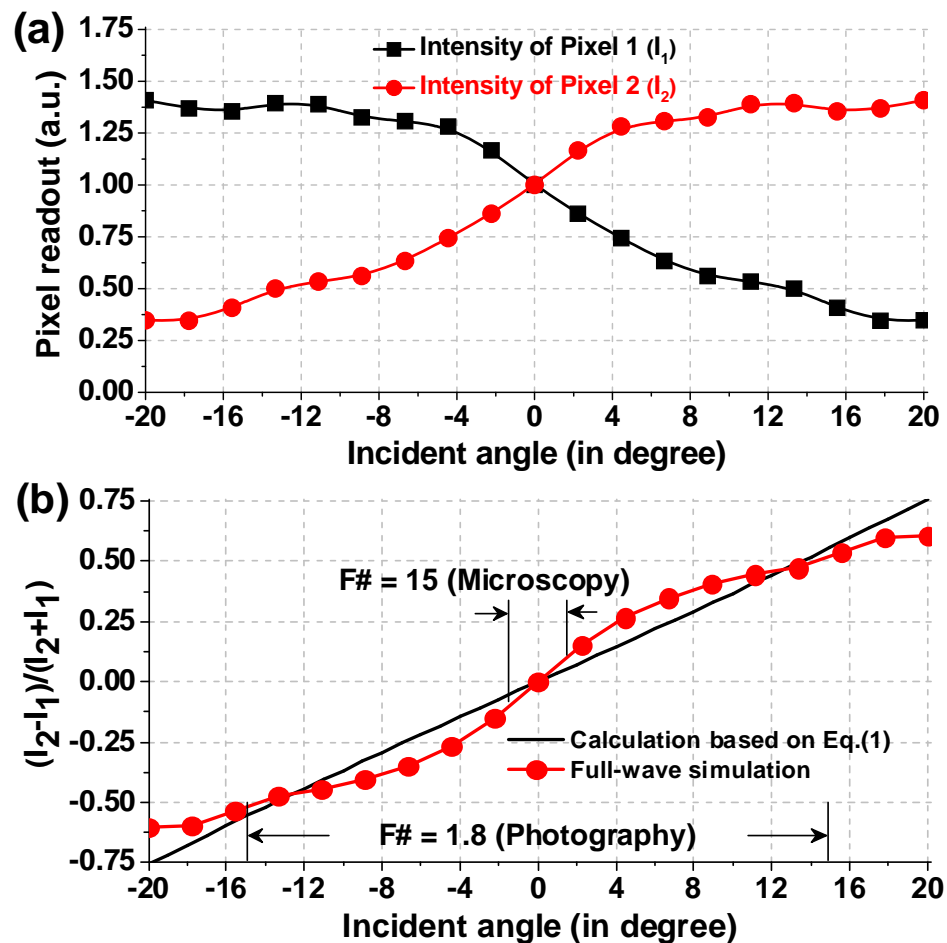


Figure 7-3 (color): Characterization of the propose ASP design. (a) Intensity readouts for pixel 1 and 2 with respect to the incident angle. (b) The angular response of the proposed ASP.

The angular range of the simulation spans from -20 to +20 in Fig. 7-3. It covers most of applications in photography and microscopy. Based on the red curve in Fig. 7-3(b), we can also determine the minimum angular sensitivity of the proposed ASP. For photography application (with an f-number of 1.8), the minimum angular sensitivity locates at the largest incident angle (~ 15 degree). Assuming we have a 10 bit image sensor with 1023 intensity levels, the minimum angular variation we can detect is 0.47 mrad (in upper limit) in this case. For microscopy application, the angular range at the image plane is about -2 degree to +2 degree, corresponding to an f-number of 15. In this range, the minimum angular variation we can detect is 0.12 mrad, about 4 times better than the previous case. Such a high angular sensitivity at small angle range also perfectly fit into microscopy applications, where high accuracy is desired for quantitative analysis.

Another trend of the CMOS image sensor development is the use of back-side illuminated pixel structure. Such a structure orients the wiring behind the photocathode layer by flipping the silicon wafer during manufacturing and then thinning its reverse side so that light can strike the photocathode layer without passing through the wiring layer. The proposed ASP can also be adapted to the back-side illuminated pixel structure. Fig. 7-4(a) and 4(b) show the FDTD simulation of the back-side illuminated ASP design. As shown in Fig. 7-4(a2), the effective opening size w_{eff} is about 1.7 times smaller than w in this case. In Fig. 7-4(c), we also compare the simulated angular response with Eq. (7-1). In such a back-side illuminated pixel structure, the active region locates at the bottom of the silicon layer. The effective layer height h is larger than that of Eq. (7-1), and thus, the simulated angular response exhibits a steeper slope in Fig. 7-4(c). The minimum angular sensitivity of such an ASP design is about 0.3 mrad over the range of -20 degree to +20 degree.

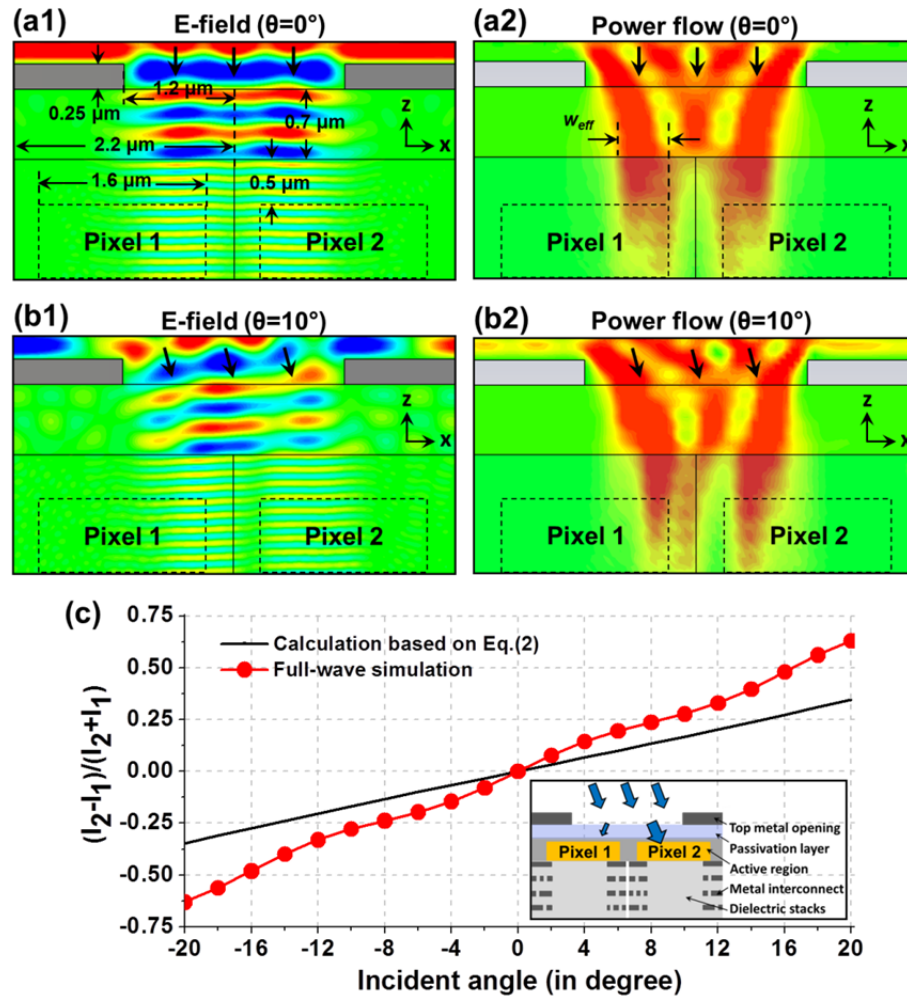


Figure 7-4 (color): The FDTD simulation of the back-side illuminated ASP design with normal incidence (a) and 10 degree incidence (b). (c) The angular response of the proposed ASP.

7.3 Discussion

To conclude, we have demonstrated a simple ASP design for both the front-side and back-side illuminated pixel structures. The proposed ASP employs the balanced detection scheme to measure the local intensity and the angular information simultaneously. The estimated angular sensitivity is about 0.1-0.4 mrad per intensity-level for a typical 10 bit CMOS image sensor. There are several advantages associated with the proposed ASP design:

1) No angular ambiguity. Unlike the diffraction-grating approach, the angular response of the proposed ASP is a monotonically increasing function with respect to the incident angle; therefore, there is no angular ambiguity for the proposed ASP.

2) High pixel density. In the proposed ASP, the recovery of the 2D angular information is based on intensity measurements of 4 conventional pixels. In other words, the ASP density is only 4 times less than that of a conventional CMOS imager, and it is generally higher than the microlens/pinhole-based wavefront sensor [8].

3) Full compatibility with the CMOS fabrication process. With only one extra metal layer on top, the proposed ASP design can be easily integrated in the conventional CMOS fabrication process. We can even directly modify an existing CMOS imager by post-fabrication processes [9, 10].

Finally, we note that, the concept of balanced detection scheme is not new. It has been demonstrated for wavefront detection at a relative large scale (~ 0.5 mm) [11]. However, we believe that the integration of such a scheme at the pixel level, especially in combination with the emerging back-side illuminated structure, enables a variety of new application possibilities in light field photography [2], phase microscopy [8], lensless imaging [6, 12] and machine vision. Some further studies of the proposed ASP, including the diffraction-based focusing effect, the optimal angular response and the optical confinement methods for adjacent ASPs [13], are highly desired in the future.

Bibliography

- [1] M. Levoy, and P. Hanrahan, "Light field rendering." pp. 31-42.
- [2] R. Ng, M. Levoy, M. Brédif *et al.*, "Light field photography with a hand-held plenoptic camera," *Computer Science Technical Report CSTR*, vol. 2, 2005.
- [3] A. Kubota, K. Aizawa, and T. Chen, "Reconstructing dense light field from array of multifocus images for novel view synthesis," *Image Processing, IEEE Transactions on*, vol. 16, no. 1, pp. 269-279, 2007.
- [4] A. Veeraraghavan, R. Raskar, A. Agrawal *et al.*, "Dappled photography: Mask enhanced cameras for heterodyned light fields and coded aperture refocusing," *ACM Transactions on Graphics*, vol. 26, no. 3, pp. 69, 2007.
- [5] A. Wang, P. Gill, and A. Molnar, "Light field image sensors based on the Talbot effect," *Applied optics*, vol. 48, no. 31, pp. 5897-5905, 2009.
- [6] P. R. Gill, C. Lee, D. G. Lee *et al.*, "A microscale camera using direct Fourier-domain scene capture," *Optics letters*, vol. 36, no. 15, pp. 2949-2951, 2011.
- [7] A. Wang, and A. Molnar, "A Light-Field Image Sensor in 180 nm CMOS," *Solid-State Circuits, IEEE Journal of*, no. 99, pp. 1-1, 2012.
- [8] X. Cui, J. Ren, G. J. Tearney *et al.*, "Wavefront image sensor chip," *Optics Express*, vol. 18, no. 16, pp. 16685-16701, 2010.
- [9] G. Zheng, and C. Yang, "Improving weak-signal identification via predetection background suppression by a pixel-level, surface-wave enabled dark-field aperture," *Optics letters*, vol. 35, no. 15, pp. 2636-2638, 2010.
- [10] G. Zheng, X. Cui, and C. Yang, "Surface-wave-enabled darkfield aperture for background suppression during weak signal detection," *Proceedings of the National Academy of Sciences*, vol. 107, no. 20, pp. 9043, 2010.
- [11] D. de Lima Monteiro, G. Vdovin, and P. Sarro, "High-speed wavefront sensor compatible with standard CMOS technology," *Sensors and Actuators A: Physical*, vol. 109, no. 3, pp. 220-230, 2004.
- [12] G. Zheng, S. A. Lee, Y. Antebi *et al.*, "The ePetri dish, an on-chip cell imaging platform based on subpixel perspective sweeping microscopy (SPSM)," *Proceedings of the National Academy of Sciences*, vol. 108, no. 41, pp. 16889-16894, 2011.
- [13] C. C. Fesenmaier, Y. Huo, and P. B. Catrysse, "Optical confinement methods for continued scaling of CMOS image sensor pixels," *Optics Express*, vol. 16, no. 25, pp. 20457-20470, 2008.

Chapter 8

0.5 gigapixel microscopy using a flatbed scanner

The third accessing point in design considerations is the image sensor. In this chapter, we show that the image sensor can also be replaced by a flatbed scanner to achieve ultrahigh pixel count for wide field-of-view imaging. We show that such an imaging system is capable of capturing a 10 mm * 7.5 mm FOV image with 0.77 micron resolution, resulting in 0.54 gigapixels (10^9 pixels) across the entire image (26400 pixels * 20400 pixels). The resolution and field curve of the proposed system were characterized by imaging a USAF resolution target and a hole-array target. Microscopy image of a blood smear and a pathology slide was acquired by using such a system for application demonstration.

8.1 Background

The conventional microscope architecture can be generally defined as consisting of a microscope objective for light collection from a sample slide, intermediate relay optics and a pair of or a singular eyepiece that projects a magnified image of the sample into our eyes. With the advancement of digital cameras, the eyepiece(s) segment of the microscope has undergone adaptation changes to be replaced with appropriate optics and camera to enable electronic imaging. Over the past decades and with the broad acceptance of infinity correction, the conventional microscope design has achieved extensive standardization across the microscopy industry - objectives and eyepieces from the major microscope makers are largely interchangeable. This standardization helps with cost-effectiveness. However, it has also limited the commercial design space for conventional microscopy - any significant design deviation that exceeds the standardization parameter space would have to contend with its incompatibility with the entrenched microscopy consumer base.

Recently, there has been an increased recognition that bioscience and biomedical microscopy imaging needs are outstripping the capability of the standard microscope. One

salient need of modern bioscience and biomedical community is for a microscopy imaging method that is able to electronically acquire a wide field-of-view (FOV) image with high resolution [1]. The standard microscope was originally designed to provide sufficient image details to a human eye or a digital camera sensor chip. As an example, the resolution of a conventional 20X objective lens (0.4 numerical aperture) is about $0.7\ \mu\text{m}$ and the FOV is only about 1 mm in diameter. The resulting space-bandwidth-product (SBP) [2] is about 8 mega-pixels (the number of independent pixels to characterize the captured image). This pixel count has only been recently reached or exceeded by digital camera imager. Interestingly, this SBP shows only slight variation across the range of commercial microscope objectives. Placed in different context, the relative invariance of SBP necessarily ties resolution and FOV together for most commercial objectives - high-resolution imaging necessarily implies a limited FOV.

In the past years, there has been significant progress in the development of system that increases the FOV of the conventional microscope system by incorporating sample slide scanning to acquire image over a large area [3] or by implementing parallel imaging with multiple objectives [4]. In addition, there have also been exciting research efforts into wide FOV imaging system, including ePetri dish [5], digital in-line holography [6], focus-grid scanning illumination [7, 8], off-axis holography microscopy [9, 10]. All these methods try to break the tie between resolution and FOV by abandoning the conventional microscopy design and shifting away from the use of optics schemes that perform optical image magnification.

The underlying assumptions that underpin all of these developments appear to be 1) a higher SBP (order of magnitude or more) with a magnification-based optical scheme is commercially impractical and 2) the associated pixel count for a radically higher SBP would face electronic image acquisition issues for which a viable solution does not yet exist.

In this chapter, we demonstrate an optical magnification microscopy solution that challenges these assumptions. The configuration of this imaging system is based on two cost-effective items: a commercial available closed-circuit-television (CCTV) lens system and a low-cost consumer flatbed scanner. We show that, such a system is capable of

capturing a 0.54 gigapixel microscopy image with a FOV of 10 mm * 7.5 mm and that a 0.77 resolution is achieved across the entire FOV. Remarkably, the CCTV lens system has a SBP of at least 0.5 gigapixel (10^9 pixels), which is about 2 orders of magnitude larger than those of conventional microscope objectives.

This chapter is structured as follows: we will first present our proof-of-concept setup; then, we will present the automatic focusing scheme of the platform. Next, we will report on the resolution and the field-curve characterization of the platform. Then, we will demonstrate the application of the proposed setup by imaging a blood smear and a pathology slide; finally, we will discuss some limitations as well as future directions for the proposed gigapixel microscopy system.

8.2 The prototype setup

Driven by the recent trend of small pixel size of the image sensor (0.7 μm pixel size has been reported in Ref. [11]), significant efforts have been put into the design of consumer/industry camera lens to match this diffraction-limited pixel size. In the past years, it has been demonstrated that the SBP of some consumer camera lenses can achieve count on the order of billion pixels, i.e., these camera lenses are capable of capturing gigapixel images [12, 13].

In our proposed microscopy imaging system, we redirected this gigapixel imaging effort [12, 13] to microscopy. The main component of the setup was a commercial available high-quality CCTV lens (C30823KP, Pentax, f/1.4, focal length 8mm). Like other consumer/industry camera lenses, the conventional use of this lens is to demagnify the scene onto the image plane, where the CMOS/CCD imager is located. In our setup (Fig. 8-1), we put our sample at the image plane to replace the CMOS/CCD imager and used the CCTV lens to magnify the sample, i.e., using the lens in the reverse manner. With a magnification factor of ~ 30 , the projected image was too large to be directly imaged with a CMOS/CCD imager. Instead, we modified and employed a consumer flatbed scanner (Canon LiDE 700F) to accomplish image acquisition. We chose this scanner for two reasons: 1) its “LED Indirect Expose (LiDE)” design and 2) the high scanning resolution (2400 dpi is measured, corresponding to a 10 μm pixel size of the scanner). Due to its

LiDE design, this scanner actually possesses a linear CCD that covers the complete width of the scanning area. In comparison, other conventional scanners use a combination of mirrors and lenses to accomplish the same functionality, and it will take additional steps to modify these scanners for our application. In our setup, we disabled the LED light source of the Canon LiDE 700F scanner by using a black tape. The relay lens array and the light guide on top of the linear CCD were also removed. Therefore, the linear CCD shown in 8-1 was directly exposed to the projected image from the CCTV lens.

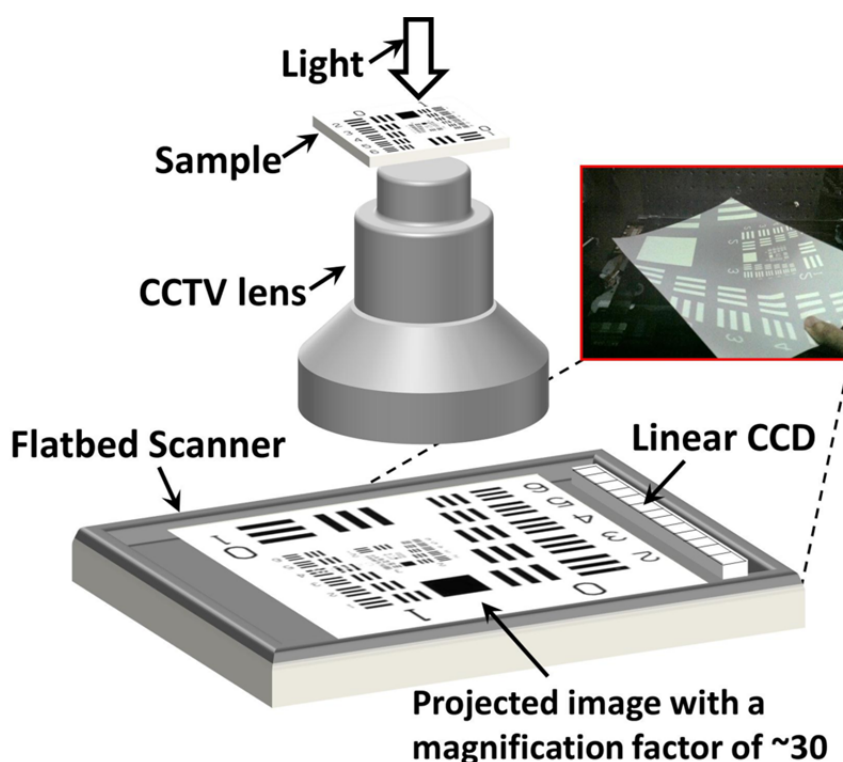


Figure 8-1 (color): The setup of the proposed 0.54 gigapixel microscopy (not to scale). A CCTV lens is used to magnify the sample by a factor of 30 and a scanner is used to capture the projected image. The distance between the sample and the lens is about 1 cm. Inset on the top right shows the magnified image of a USAF target on an A4 paper held in front of the scanner.

The scanning resolution was set to 2400 dpi, the maximum resolution of the scanner (corresponds to a 10 μm pixel size); the FOV of the scanner was set to the

maximum scanning area (297 mm * 216 mm). The magnification factor was ~30 in our platform, and it corresponded to a FOV of 10 mm * 7.5 mm at the object side. The distance between the sample and the CCTV lens is about 1 cm and the distance between scanner and the lens is about 30 cm. We used a diffuse LED light source from top for illumination. Based on these settings, the capture image contained 26400 pixels * 20400 pixels, and thus, it produced a 0.54 gigapixel microscopy image of the sample. Inset of Fig.1 shows the projected image of a USAF target on a letter size paper held in front of the scanner.

8.3 Automatic focusing scheme

In a conventional microscope setup, the image recording device can give real time update on the object, and therefore, it is easy to adjust the position of the stage to the best focus position. In the proposed platform, the scanner takes a relative long time to acquire the entire image of the object, and thus, it takes a long time to find out the best focus position. To address this issue, we used an automatic focusing scheme with a programmable stage in our setup, as shown in the inset of Fig. 8-2(a2). This focusing scheme consists of three steps: 1) move the stage with a constant speed (5 $\mu\text{m/s}$); 2) acquire the image at the same time (only certain part of the image is in-focus along the scanning direction); 3) define an F index to find out the best focus position from the acquire image. In step 3, we define the F index using the following equation

$$F \text{ index} = \sum_{x=1}^{end} |2f(x, y) - f(x - step, y) - f(x + step, y)| \quad (8-1)$$

Such an F index is a measurement of the sharpness of the image.

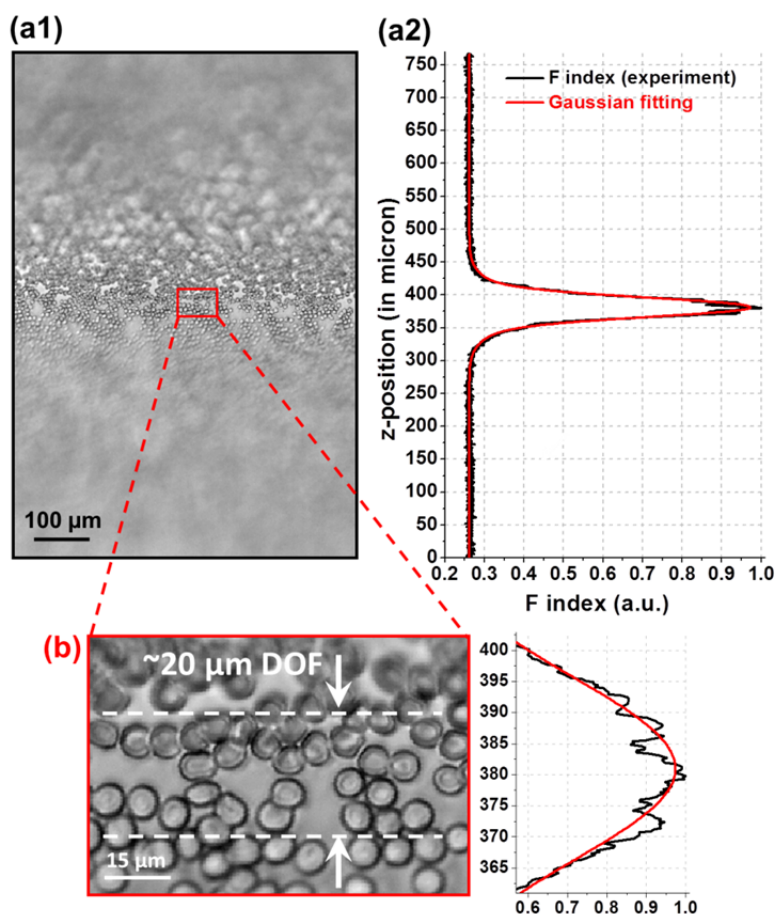


Figure 8-2 (color): The automatic focusing scheme of the proposed setup. (a1) The acquired image of a blood smear with the stage moving at a constant speed at z-direction. (b) Based on the motion speed, we can plot the F index with respect to different z positions, and thus, automatically locate the best focused position of the sample. (b) The magnified image of (a), where the depth-of-focus is estimated to be $\sim 20 \mu\text{m}$. In this experiment, a diffused green LED with 20 nm spectrum bandwidth is used for illumination.

Fig. 8-2(a1) is the acquired image of a blood smear following the above steps (only a small portion of the image is acquired for faster scanning). We can see that the sample is out-of-focus at the beginning, then, the stage bring the sample into focus at the middle part of the image, and finally, the sample is out-of-focus again. Based on the motion speed of the programmable stage, we can plot the F index (with ‘step’ = 2) versus different z-positions, as shown in Fig. 8-2(a2). The peak of the F index is estimated to be located at $z =$

381 μm . The magnified image and the corresponding F index are shown in Fig. 8-2(b), where the depth-of-focus (DOF) is estimated to be $\sim 20 \mu\text{m}$. The proposed automatic focusing scheme works well with biological samples and pathology slides. The entire focusing process takes about 1~2 minutes for the proposed platform. However, we note if the sample is extremely sparse (for example, one small hole on a metal mask), such a scheme will fail and we have to take multiple images at different z positions to find out the best focus position.

8.4 Resolution and field curve of the platform

We next characterize the resolution and the field-curve of the proposed imaging system. We first imaged a USAF target, as shown in Fig. 8-3. It is well known that, the aberration of a physical lens will degrade the image resolution at different FOVs of the lens, i.e., the resolution may be different from the center to the edge FOVs. In order to test the resolution at different FOVs, we translated the USAF target across the FOV of the CCTV lens and captured the corresponding images in Fig. 8-3(a-c). A diffused green LED light source (530 nm wavelength, with ~ 20 nm spectrum bandwidth) was used in this experiment for illumination.

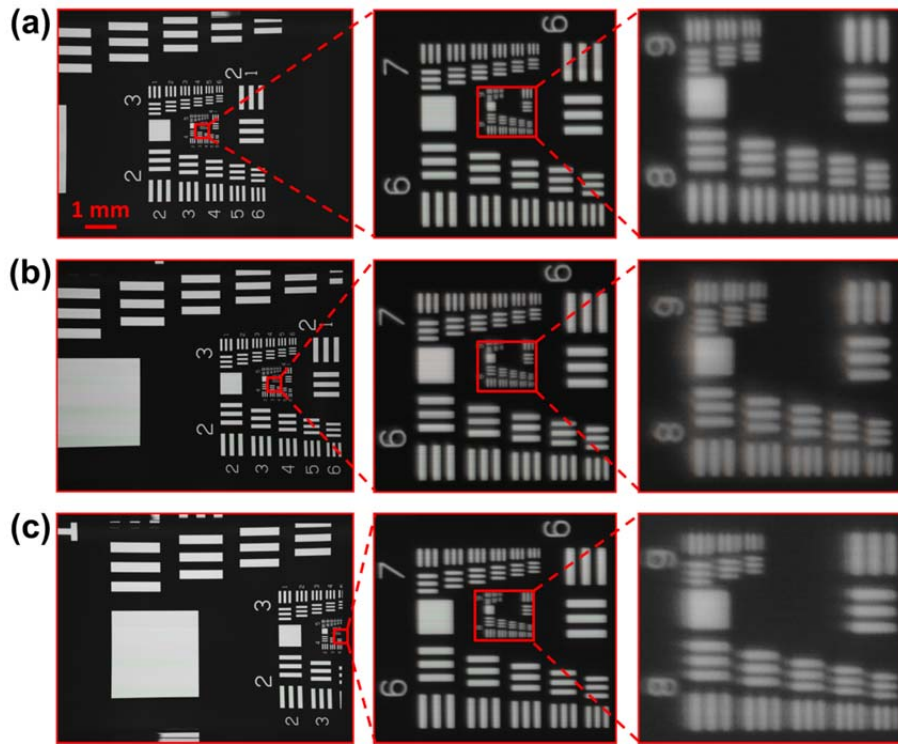


Figure 8-3 (color): USAF resolution target acquired by the proposed 0.54 gigapixel microscopy system. The effective FOV is about 10 mm * 7.5 mm, with 26400 pixels * 20400 pixels across the entire image. The imaging performance at the (a) center, (b) 50% away from center and (c) 95% away from center. The line widths of group 9, element 1, 2 and 3 are 0.98 μm , 0.87 μm and 0.77 μm respectively.

In the USAF target, the line widths of group 9, element 1, 2 and 3 are 0.98 μm , 0.87 μm and 0.77 μm , respectively. The image performance at the center of the FOV is shown in Fig. 8-3(a), where we can clearly see the feature at group 9, element 3 (0.77 μm line width). In Fig. 8-3(b) and (c), we translate the sample to 50% and 95% of the FOV away from center (100% corresponds to 10 mm). In both images, we can still clearly see the fine feature at group 9, element 3 (0.77 μm line width). This establishes the resolution of our prototype system is, under the monochromatic green light illumination, 0.77 μm over the entire FOV. We note that, by Nyquist theorem, we need at least two pixels to capture the smallest detail of the image, and thus, the effective pixel size at the object size should be less than 385 nm. Based on Section 1, the effective pixel size of our platform is about 330

nm ($10\ \mu\text{m}$ divided by magnification factor), which fulfills the requirement of Nyquist theorem in this regard. In Fig. 8-3(c), the horizontal resolution is worse than the vertical resolution. Such an effect is due to the high order aberration of the lens, such as coma. We also note that, due to the pixel-response differences of the linear CCD, line-artifact is present in the raw scanning data [13]. This effect can be eliminated by performing a simple normalization process: 1) capture a reference image without any sample; 2) normalized the raw scanning image of the sample with the reference image. In this process, the reference image is sample-independent, i.e., it can be used for any sample.

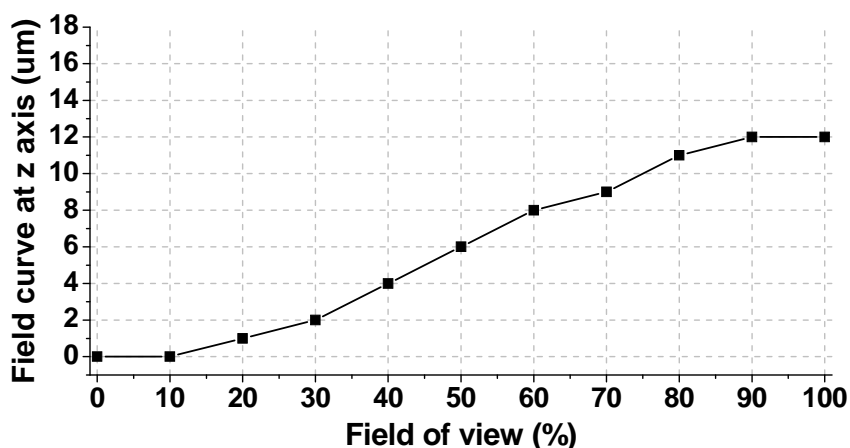


Figure 8-4: Displacement of the best focal plane of different FOVs (from center to edge FOV). In this figure, 100% in x-axis corresponds to 10 mm.

In the second experiment, we want to characterize the field curve of the imaging system. Our sample was a chrome mask ($1.8\ \text{cm} * 1.8\ \text{cm}$) with a hole-array on it (fabricated by lithography). The size of the hole was about $1\ \mu\text{m}$ in diameter and periodicity of the hole-array was $30\ \mu\text{m}$. The light source of this experiment is the same as before (a green LED with a $20\ \text{nm}$ spectrum bandwidth). First, we captured a series of images as we mechanically shifted the chrome mask into different z positions; then, we analyzed the spot size to locate the best focal plane for different FOVs, with the result shown in Fig. 8-4 (for example, at 50% FOV, the best focal plane locates at $z = 6\ \mu\text{m}$). The displacement of the best focal plane is directly related to field curve of the imaging system. Remarkably, the result shows that the field curvature is relatively small (maximum

observed of 12 micron z-displacement) over the entire FOV under the monochromatic illumination.

8.5 Imaging of a blood smear and a pathology slide

We next used our system for imaging demonstration. First, we acquired a monochromatic image of a human blood smear using a green LED light source. The sample was automatically tuned to its in-focus position based on the automatic focusing scheme described in Section 8.3. Fig. 8-5 shows the acquired image, where the scanner and magnification setting is the same as before. There are 200 times difference in the scale bars between Fig. 8-5(a) and (b3). In order to appreciate the wide FOV capability, we also prepare a video showing the entire and the magnified view of the image.

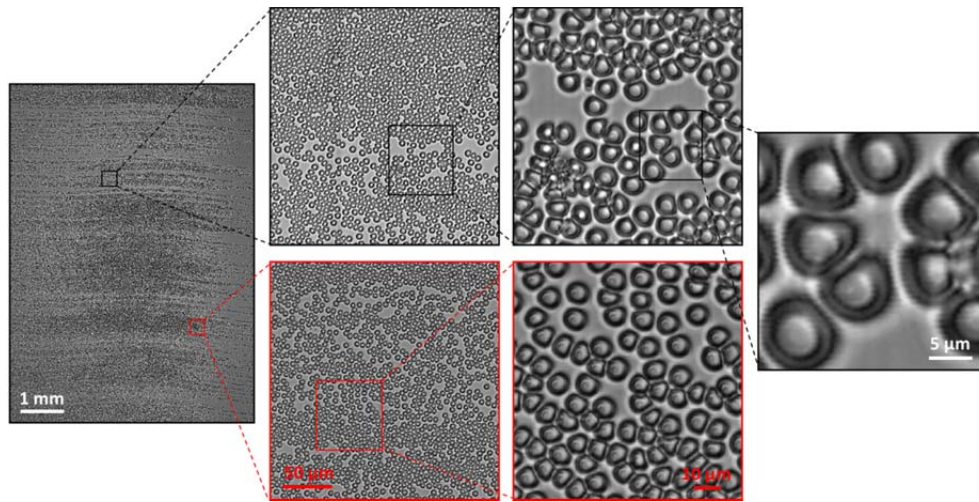


Figure 8-5 (color): 0.54 monochromatic gigapixel image of a blood smear. (a) The full FOV of the captured image. (b1), (b2), (b3) and (c1), (c2) are the expanded view of the (a).

The proposed platform can also be used for color imaging. We used R/G/B diffused LED light sources for three color illuminations, similar to Ref. [14]. The sample slide was automatically tuned into its in-focus position for each color illumination ($\Delta z=3 \mu\text{m}$ for the blue LED and $-12 \mu\text{m}$ for the red LED). Three images (for R/G/B) are separately acquired, normalized, aligned [15] and then combined into the final color image. Fig. 8-6 shows the

acquired color image of a pathology slide (human metastatic carcinoma to liver, Carolina Biological Supply). Fig. 8-6(a) shows the wide FOV image of the pathology sample. Fig. 6 (b1), (b2) and (c1), (c2) are the corresponding expanded view for Fig. 8-6(a).

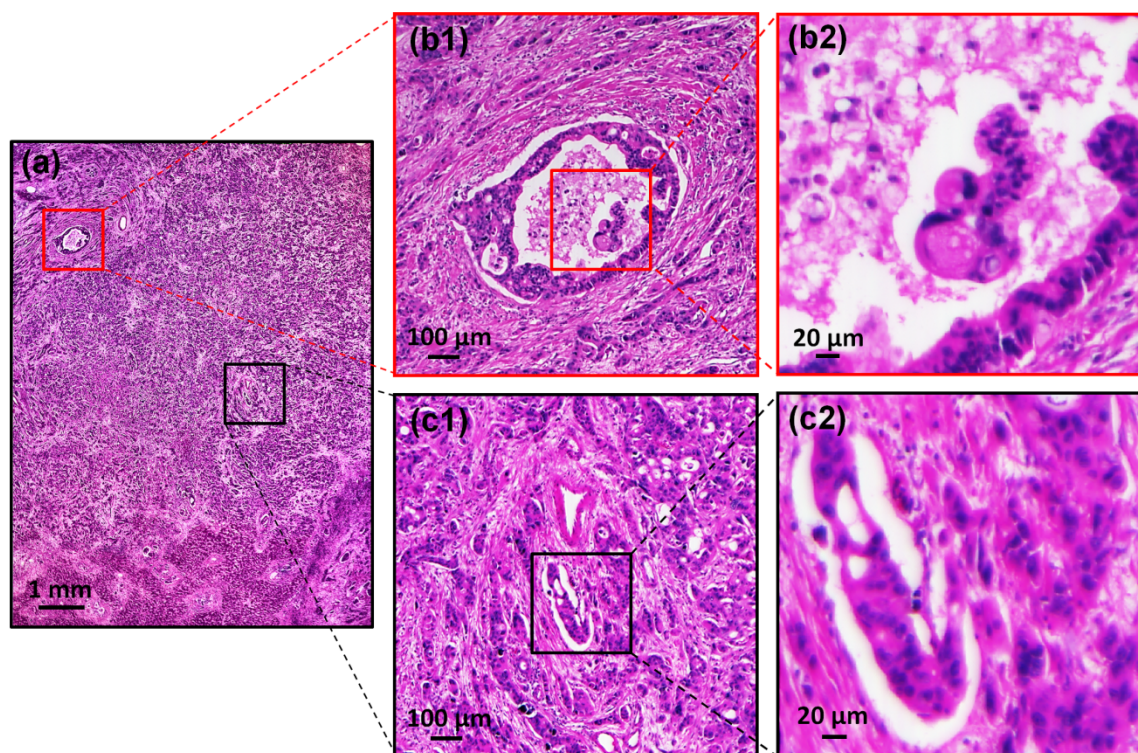


Figure 8-6 (color): 0.54 gigapixel color image of a pathology slide (human metastatic carcinoma to liver). (a) The full frame of the acquired image. (b1), (b2) and (c1), (c2) are the expanded view of (a).

8.6 Conclusion

In summary, we report a wide-FOV (10 mm * 7.5 mm) microscopy system which can generate a 0.54 gigapixel microscopy image with 0.77 μm resolution across the entire FOV. We note that there are other large-format professional camera lenses for even larger FOV (for example, 35 mm in diameter). The bottom line we want to convey in this paper is that lenses from the photography/industry community may provide a potential solution for high throughput microscopy imaging. Interested readers can choose their lenses based on the balance between the price and the performance.

It is interesting to contrast the SBP and resolution of our demonstrated system versus those of the conventional microscope. As shown in Fig. 8-7, the effective SBP of our system is more than one order of magnitude greater than those of the microscope objectives. Compared to a typical 10X and 4X objectives, our system has both superior SBP and resolution.

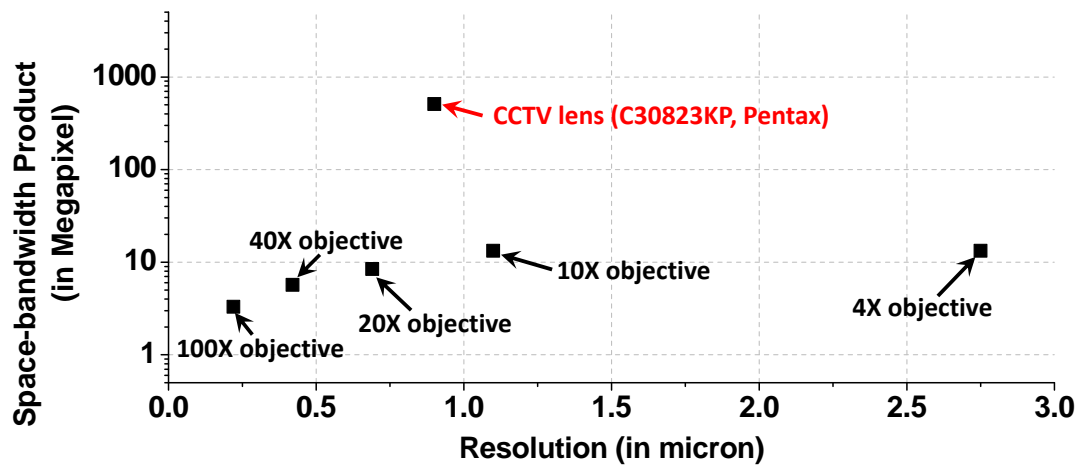


Figure 8-7 (color): The SBP-resolution summary for microscope objectives and the proposed system.

We note that one important limitation of the system is the scanning speed. A full-scan at 2400 dpi scanning resolution with USB 2.0 link took about 10 minutes. There are three strategies to address this issue: 1) use other high speed scanners; 2) use multiple scanners for parallelization (we can take out the linear CCDs and its housing components from multiple scanners and assemble them into one scanner); 3) use other scanning devices such as the digital scanning back (for example, a commercial available digital scanning back takes 29 seconds to capture a 0.312 gigapixel image). Our future directions include: 1) improve the speed of setup using the strategies discussed above; 2) incorporate other imaging functionalities such as 3D, darkfield and phase imaging into the proposed wide FOV platform [16, 17].

Bibliography

- [1] M. Oheim, "Advances and challenges in high-throughput microscopy for live-cell subcellular imaging," *Expert Opinion on Drug Discovery*, no. 0, pp. 1-17, 2011.
- [2] A. VanderLugt, *Optical signal processing*. Wiley New York, 1992.
- [3] J. Gilbertson, J. Ho, L. Anthony *et al.*, "Primary histologic diagnosis using automated whole slide imaging: a validation study," *BMC clinical pathology*, vol. 6, no. 1, pp. 4, 2006.
- [4] Dmetrix, "<http://www.dmetrix.net/techtutorial1.shtml>."
- [5] G. Zheng, S. A. Lee, Y. Antebi *et al.*, "The ePetri dish, an on-chip cell imaging platform based on subpixel perspective sweeping microscopy (SPSM)," *Proceedings of the National Academy of Sciences*, vol. 108, no. 41, pp. 16889-16894, 2011.
- [6] W. Bishara, T. Su, A. Coskun *et al.*, "Lensfree on-chip microscopy over a wide field-of-view using pixel super-resolution," *Optics Express*, vol. 18, no. 11, pp. 11181-11191, 2010.
- [7] J. Wu, X. Cui, G. Zheng *et al.*, "Wide field-of-view microscope based on holographic focus grid illumination," *Optics letters*, vol. 35, no. 13, pp. 2188-2190, 2010.
- [8] J. Wu, G. Zheng, Z. Li *et al.*, "Focal plane tuning in wide-field-of-view microscope with Talbot pattern illumination," *Optics letters*, vol. 36, no. 12, pp. 2179-2181, 2011.
- [9] J. Di, J. Zhao, H. Jiang *et al.*, "High resolution digital holographic microscopy with a wide field of view based on a synthetic aperture technique and use of linear CCD scanning," *Applied optics*, vol. 47, no. 30, pp. 5654-5659, 2008.
- [10] M. Lee, O. Yaglidere, and A. Ozcan, "Field-portable reflection and transmission microscopy based on lensless holography," *Biomedical Optics Express*, vol. 2, no. 9, pp. 2721-2730, 2011.
- [11] K. Fife, A. Gamal, and H. Wong, "A 3mpixel multi-aperture image sensor with 0.7 um pixels in 0.11 um cmos." pp. 48-49.
- [12] M. Ben-Ezra, "Large-Format Tile-Scan Camera," *IEEE Computer Graphics and Applications*, pp. 49-61, 2011.
- [13] S. Wang, and W. Heidrich, "The Design of an Inexpensive Very High Resolution Scan Camera System," *Computer Graphics Forum*, vol. 23, no. 3, pp. 441-450, 2004.
- [14] S. A. Lee, R. Leitao, G. Zheng *et al.*, "Color Capable Sub-Pixel Resolving Optofluidic Microscope and Its Application to Blood Cell Imaging for Malaria Diagnosis," *PloS one*, vol. 6, no. 10, pp. e26127, 2011.
- [15] J. Mallon, and P. F. Whelan, "Calibration and removal of lateral chromatic aberration in images," *Pattern recognition letters*, vol. 28, no. 1, pp. 125-135, 2007.
- [16] G. Zheng, C. Kolner, and C. Yang, "Microscopy refocusing and dark-field imaging by using a simple LED array," *Optics letters*, vol. 36, no. 20, pp. 3987-3989, 2011.
- [17] L. Waller, S. S. Kou, C. J. R. Sheppard *et al.*, "Phase from chromatic aberrations," *Optics Express*, vol. 18, no. 22, pp. 22817-22825, 2010.

Chapter 9

Summary

In this thesis, we have presented several new microscope imaging techniques from three aspects: illumination design, sample manipulation and imager modification.

Illumination source is the first accessing point in the optical path of a microscopy imaging system. The first design strategy involves the active control of the illumination sources. Based on this strategy, we demonstrated a simple and cost-effective imaging method, termed Non-interferometric Aperture-synthesizing Microscopy (NAM), for breaking the spatial-bandwidth product barrier of a conventional microscope (**Chapter 2**). We showed that the NAM method is capable of providing two orders of magnitude higher throughput for most existing bright-field microscopes without involving any mechanical scanning. Based on NAM, we demonstrated the implementation of a 1.6 gigapixel microscope with a maximum numerical aperture of 0.5, a field-of-view of 120 mm², and a resolution-invariant imaging depth of 0.3 mm. The proposed NAM method is also able to recover the phase profile of the sample. In this regard, NAM provides an easy and cost-effective solution for researchers and clinicians to incorporate phase imaging functionality into their current microscope systems. The proposed NAM method, readily implemented with a conventional microscope, has the potential to broadly impact digital pathology, histology, phytotomy, immunochemistry and forensic photography. It can also be extended to other spectrum such as THz and X-ray regions, where lenses are poor and of very limited numerical aperture.

The active control of illumination sources can also be adapted for chip-scale microscopy imaging. In **Chapter 3**, we introduced a chip-scale microscopy solution, termed Sub-pixel Perspective Sweeping Microscopy (SPSM) and demonstrated a proof-of-concept self-imaging digital Petri dish solution. This on-chip platform has the ability to automatically image confluent cell sample with sub-cellular resolution over a large field-of-view. As such, it is well suited for long-term cell culture imaging and tracking applications.

Unlike the other lensless microscopy methods, this new approach is fully capable of working with cell cultures or any samples in which cells/bacteria may be contiguously connected, and thus, it can significantly improve Petri-dish-based cell/bacteria culture experiments. With this approach providing a compact, low-cost and disposable microscopy imaging solution, we can start to transit Petri-dish-based experiments from the traditionally labor-intensive process to an automated and streamlined process.

The active control of the illumination light source can also be combined with tomography reconstruction technique for 3D imaging. In **Chapter 4**, we present the implementation of digital 3D refocusing approach using a simple LED matrix. We showed that such an approach can be used to render a bright field image, dark field image, and more importantly, sectioned images at different depths without involving mechanical scanning.

The second strategy in design considerations is to manipulate the sample. In **Chapter 5**, we presented a fully on-chip, lensless microscope device, termed sub-pixel resolving optofluidic microscope (SROFM). The novel combination of a pixel super-resolution and optofluidic approach towards microscopy removes the need for bulky and expensive lenses, coherent illumination sources and precision microscanning mechanisms. In addition, the SROFM system also allows us to capture images and videos of rotating samples in high resolution and, thereby, reveal three-dimensional sub-cellular structures from different perspectives. SROFM's simplicity, compactness, and cost-effectiveness make it well-suited for drop-and-flow screening of fluidic samples such as blood, urine or water. The SROFM technique can potentially play an important role in the eventual development and commercialization of a mass-distributed, portable microscope for point-of-care analysis and third-world diagnostics, for the detection of water-borne parasites, blood-borne parasites and diseases involving blood cell deformations.

The third accessing point in design considerations is the image sensor. Imager modification is an emerging technique that performs pre-detection light field manipulation. In **Chapter 6**, we presented a novel optical structure design, termed surface-wave-enabled darkfield aperture (SWEDA), which can be directly incorporated onto optical sensors to accomplish pre-detection background suppression. A detection system that can effectively

suppress background contributions (prior to detection) and allow detection of small signals in extremely compact device architectures is potentially useful for a broad range of applications from on-chip bio-sensing to metrology and microscopy.

Conventional image sensors are only responsive to the intensity variation of the incoming light wave. By encoding the wavefront information into the balanced detection scheme, we demonstrated an image sensor pixel design that is capable of detecting both the local intensity and angular information simultaneously in **Chapter 7**.

In **Chapter 8**, we showed that the image sensor can also be replaced by a flatbed scanner to achieve ultrahigh pixel count for wide field-of-view imaging. We showed that such an imaging system is able to capture a 10 mm * 7.5 mm field-of-view image with 0.77 micron resolution, resulting in 0.54 gigapixels (10^9 pixels) across the entire image (26400 pixels * 20400 pixels).

To summarize, the new microscopy imaging techniques presented in this thesis could increase the throughput, reduce the cost and improve the efficiency and quality of microscopy imaging in biological research. We also anticipate that they will generate a revolutionary impact on some of industry applications, such as digital pathology, histology, immunochemistry, and cell-culture-based clinical diagnosis.